Statistical Evaluation of the Imbibition of Polymers into Porous Materials

Dissertation

submitted
by

Fernando Vazquez Luna

to the School of Biology/Chemistry
at the University of Osnabrück

Osnabrück, 2022

Dissertation to partially fulfill the requirements for the degree of

'Doctor rerum naturalium'

presented by Fernando Vazquez Luna

to the School of Biology/Chemistry, University of Osnabrück

Reviewer #1: Prof. Dr. Martin Steinhart

Reviewer #2: Prof. Dr. Patrick Huber

Abstract

Frozen transient imbibition states into two complementary pore models having pore diameters of ~380 nm and hydroxyl-terminated inorganic-oxidic pore walls, controlled porous glass (CPG) and self-ordered porous alumina (AAO), were imaged by phase-contrast X-ray computed tomography (X-ray CT), scanning electron microscopy (SEM) and energy dispersive X-ray spectroscopy mapping (EDX). The deployment of phase-contrast X-ray CT bring together the advantages of macroscopic averaging methods and microscopy by allowing the algorithmic evaluation of three-dimensional reconstructions of imbibition morphologies to study characteristic features with characteristic length scales in the range from a few tens of µm down to the sub-µm scale, not possible with averaging methods, and with high validity, unattainable with microscopy.

CPG contains continuous spongy-tortuous pore systems. AAO containing arrays of isolated straight cylindrical pores is a reference pore model with a tortuosity close to 1. Comparative evaluation of the spatiotemporal imbibition front evolution yields important information on the pore morphology of a probed tortuous matrix like CPG and on the imbibition mechanism. Image analysis methods based on the evaluation of pixel brightness fluctuations were developed to determine imbibition front positions and widths by descriptive statistics. The retardation of the imbibition front movement with respect to AAO reference samples may be used as a descriptor for the geometric tortuosity of a tested porous matrix. The velocity of the imbibition front movements in CPG equaled two-thirds of the velocity of the imbibition front movements in AAO. Moreover, the dynamics of the imbibition front broadening discloses whether porous matrices are dominated by cylindrical neck-like pore segments or by nodes. Independent single-meniscus movements in cylindrical AAO pores result in faster imbibition front broadening than in CPG, in which a morphology dominated

by nodes results in slower cooperative imbibition front movements involving several menisci. The results presented here may be relevant to a broad variety of applications including printing, adhesive bonding, oil recovery, water filtration, as well as the optimization of production and properties of engineering, construction and hybrid materials.

Declaration of authorship

I hereby declare that the presented thesis

Statistical Evaluation of the Imbibition of Polymers into Porous Materials

was prepared entirely on my own. Outside sources were not used without an explicit declaration in the text. The following persons attributed to this work as collaboration partners:

- Guido Dittrich conducted the estimation of imbibition length frequencies from a pore diameter histogram of AAO and the estimation of imbibition lengths, dead layers and role of hydraulic tortuosity on CPG.
- Theresa Paul conducted the fabrication and mercury intrusion characterization of the CPG membranes.
- Christine Schulz-Kölbel and Claudia Heß conducted the fabrication of the AAO membranes.
- Michael Gerstenberger wrote the script for the identification of the imbibition fronts, the determination of average imbibition lengths L_a and the quantification of the imbibition front widths of AAO from X-ray-CT data.
- Dr. Juliana Martins de Souza e Silva and Dr. Cristine Santos de Oliveira conducted the X-ray CT imaging.
- Dr. Anjani Kumar Maurya wrote the script for the batch extraction of roughness profiles from X-ray-CT data.

I have not attempted a promotion before, and this work was not presented to any other institution before.

Osnabrück (August, 2022) Fernando Vazquez Luna

Acknowledgments

Every episode in our lives has inception and conclusion points, for both of those points of my doctorate I would like to express my gratitude to Prof. Dr. Martin Steinhart that granted me the opportunity to grow professionally not only by accepting me as his student but also for the enthralling discussions and thoughtful guidance along the way. His knowledge and vast patience throughout the writing process of scientific articles and this dissertation nurtured them to successful completion.

In science as in many regards of life, knowledge and interesting discussions bring meaningful depth to it, for this I would like to thank Prof. Dr. Patrick Huber, Prof. Dr. Dirk Enke and Prof. Dr. Ralf Wehrspohn. I am also thankful to Dr. Juliana Martins de Sousa e Silva, Dr. Cristine Santos de Oliveira for their help with X-ray CT imaging, to Guido Dittrich for his help with many calculations of L_s, L_a, and dead layers for AAO and CPG, and Theresa Paul for the fabrication and characterization of CPG membranes. Without their kind collaboration and enthusiastic discussions this work would not have come to fruition.

Coding has always been a challenging skill for me. Therefore, I am thankful to Michael Gerstenberger for his help with the code in Python to analyze the AAO membranes, and Dr. Anjani K. Maurya, whom I had the fortune to meet during our master studies, for his help with the MatLab code to do the analysis of the X-ray CT data from AAO and CPG.

Between inception and conclusion points there is a long path along which I met wonderful and fun colleagues from the physical chemistry group to whom I am also deeply thankful. Christine Schulz-Kölbel and Claudia Heß provided me crucial help with the fabrication of AAO templates. Barbara Gunkel whose assistance with many administrative issues will always be gratefully remembered. Dr. Helmut Schäfer, Dr. Qaiser Ali Khan, Dr. Michael Phillipi and Dr. Mercedes Runge provided always enjoyable and engaging discussions.

There were particularly dark times throughout my PhD path and during those times two persons came to me as beacons of warm light, first as colleagues and then as unconditional friends. Dr. Anna Eichler-Wolf who has the best pronunciation of my name and Ружа Периз whose name I was never able to pronounce correctly, the best officemate and plant keeper one could ask for. Both made me walk like nobody else has, my gratitude for you two is eternal.

I am grateful to my friend S. Patricia G. L. who is always there for me in times of need, with a response time of 30 to 50 business days. Finally, to my parents, my lifelong teachers whom always encouraged me to be curious and in a continuous state of learning, and my sister who has the kindest heart of all.

Table of Contents

Table of contents

1 Introduction

Imbibition of porous scaffolds[1] involves the replacement of a receding fluid, such as air, by an invading fluid, such as a polymer. It is of significant relevance to a variety of application fields ranging from geophysics[2] to carbon dioxide trapping[3] to inkjet printing[4] to dentistry.[5] Furthermore, imbibition underlies the preparation of functional nanostructured composite and hybrid materials,[6-8] including optical hybrids,[9-10] solar cells[11] and active ingredient depots.[12]

The simplest imbibition model scenario, the invasion of straight cylindrical pores by fluids wetting the pore walls under conditions where gravitation can be neglected, is commonly described by a power law:

$$L_s = \nu \cdot t_i^n \qquad \text{(Equation 1.1)}$$

The imbibition length L_s is the length of the segment of a cylindrical pore, which is filled by an invading liquid after an elapsed imbibition time t_i. The classical Lucas-Washburn theory predicts a value of 0.5 for the exponent n of t_i. This time scaling is the result from the balance of Laplace pressure and an increase in viscous drag behind the imbibition front inside the capillary.[13] Deviations from the classical Lucas-Washburn (LW) scenario are expected when the capillarity of the liquid, the liquid-solid interaction or the hydraulic permeability as a function of time change. In addition, deviations from LW dynamics have been attributed to “dead layers” of adsorbed molecules of the invading species on the pore walls,[14-17] thermal fluctuations, van der Waals forces and hydrodynamic slippage.[13, 18] Furthermore, the development of precursor films during imbibition of single-pores result in abundant transient nanoscopic single-pore imbibition morphologies.[19-20]

Attempts to correspondingly adapt the LW equation predominantly addressed the nature of the preexponential factor ν.[21-23] In addition, geometries that differ from an ideal cylindrical shape can lead to average imbibition front position L_a to $t_i^{1/2}$ deviations from classical LW scenario.[24] Likewise, imbibition front roughening[23] is observed when pore diameter dispersion is present as in self-ordered nanoporous anodic aluminum oxide (AAO).[25]

While even predictive understanding of imbibition on the single-pore level has remained scarce,[22, 26] frequently porous matrices, such as controlled porous glass (CPG),[27] in which pore walls and pores form two interpenetrating networks, are imbibed.[28-29] In this case, collective effects from hydraulically coupled menisci at the imbibition fronts superimpose single-pore imbibition phenomena.[2, 30-32] Often, values of the time exponent lower than 0.5 have been observed,[33] suggesting that LW dynamics may not fully explain imbibition of complex three-dimensional porous materials. Additionally, cooperative changes from the imbibition front topography, like avalanche like relaxations,[34-38] viscous fingering[35, 39] and imbibition front roughening,[35, 39-42] are an outcome of differences in the Laplace pressures at the hydraulically coupled menisci with diameter variations at the imbibition front. Consequently, descriptions of imbibition dynamics have been modified to consider tortuosity and geometry of the fluid invaded porous material.[43]

To describe the spatiotemporal evolution of imbibition fronts during the invasion of porous matrices by wetting fluids, average positions of the imbibition fronts need to be determined and imbibition front widths need to be quantified in a statistically reliable way. Imbibition fronts have been inspected with the naked eye[44-45] and by averaging methods, such as small-angle X-ray scattering,[22] dielectric spectroscopy,[46-48] neutron radiography,[41, 49] gravimetry[50-52] and opto-fluidic techniques.[19, 53-58] In particular, quantifying the imbibition front width reliably and in a reproducible way with scales spanning from few 100 nm to few micrometers is still demanding.

The imbibition of Polystyrene (PS) into self-ordered AAO, [25, 59-61] and CPG[27] was investigated. AAO is a nearly ideal pore model with a tortuosity close to 1 which contains arrays of straight parallel cylindrical pores oriented strictly normal to the membrane surface (**Figure 1.1a**) accessible by two-step anodization and CPG is a pore model in which pores and pore walls form spongy interpenetrating networks (**Figure 1.1b**) accessible by selective leaching of phase-separated alkali borosilicate glass plates. The comparison with self-ordered AAO as a reference pore model having a tortuosity close to 1 yields information on the pore morphology of probed tortuous porous matrices, such as CPG, and insight into the mechanisms governing their imbibition.

Zernike phase-contrast X-ray computed tomography (X-ray CT)[62-66] yielding 3D images of extended sample volumes with spatial sub-micron resolution was used for characterization and the results obtained were compared with results from scanning electron microscopy (SEM) providing 2D real-space images of the probed cross-sections and energy-dispersive X-ray (EDX) spectroscopy which yields cross-sectional 2D EDX maps. X-ray CT enables probing imbibition-relevant structural features characterizing transient imbibition stages with single-pore resolution in the sub-µm range, as well as probing of much larger sample volumes than by classical microscopy methods. Thus, structural features characterizing transient imbibition stages, such as imbibition lengths and imbibition front widths, can be imaged and evaluated with excellent validity even when they are characterized by submicron length scales. The only similar powerful method would be focus ion beam (FIB) tomography. However, FIB tomography requires the ablation of sample material between the imaging of consecutive slices, which may result in the emergence of artifacts. Moreover, in contrast to FIB tomography X-ray computed tomography allows the deployment of phase-contrast imaging, which is particularly suitable to image interfaces, such as imbibition fronts.

PS with a mass-average molecular weight M_w = 239 kg/mol and a number-average molecular weight M_n = 233 kg/mol was infiltrated into AAO and CPG, both membranes had hydroxyl-terminated inorganic-oxidic pore walls and approximately similar mean pore diameters of ~380 nm, for infiltration times t_i of 3, 10, 20, 30, 70 and 90 minutes at 200°C. At this temperature, each PS chain in a bulk PS melt is involved in ~13 entanglements.[67-68] Bent et al. reported a radius of gyration of 12 nm for quiescent melts of PS with M_w = 260000 g/mol, which is comparable to the M_w value of the PS used here, at a temperature comparable to the infiltration temperature applied here.[69] Under flow, the radius of gyration in the flow direction increased to 15 nm, while the radius of gyration normal to the flow direction slightly decreased to 11 nm. Therefore, it is reasonable to assume that the diameter of gyration is at least one order of magnitude smaller than the membranes pore diameter. It should be noted that trapped air did not influence the imbibition process since diffusive transport of small molecules, such as N_2 and O_2, is orders of magnitudes faster than the imbibition processes studied here.[70] Since high-resolution X-ray CT measurements last several hours, this method is not suitable for in situ imbibition monitoring. However, the highly entangled PS used here is characterized by a high glass transition temperature of ~100°C. Therefore, transient imbibition stages can conveniently be frozen by thermal quenching to room temperature, where the PS is vitrified. The quenched transient imbibition stages remain arrested throughout the X-ray CT measurements. Consequently, the time scales of imbibition and the X-ray CT measurements are decoupled.

Introduction

To link volumetrically reconstructed sample morphologies to physical models, sample features of interest as well as parameters allowing their quantitative description need to be identified. So far, sample evaluation is frequently done by visual inspection – an approach associated with noise restricting its reliability.[71] Therefore, two semi-automatic algorithmic image analysis procedures based on descriptive statistics of pixel intensity dispersion for the identification of the imbibition fronts, the determination of average imbibition lengths L_a and the quantification of the imbibition front widths were developed. These algorithms result in five different image analysis methods depending on characterization technique used or the porous material analyzed.

The first semi-automatic algorithm is employed to analyze 3D reconstructions of X-ray CT from AAO, yielding brightness profiles along all identified AAO pores in the probed sample volume resulting in two methods *CT-mean* and *CT-rms.* In method *CT-mean* (cf. Section 4.2), histograms of single-pore imbibition lengths were evaluated to obtain L_a and the imbibition front width. In method *CT-rms* (cf. Section 4.2) the statistical pixel intensity dispersion R_q as a function of the distance to the AAO surface was evaluated.

Batch-CT-rms (cf. Section 4.3) and *EDX-rms* (cf. Section 4.4) are two methods that does neither involve segmentation procedures nor requires the determination of pore coordinates, hence is applicable for both AAO and CPG. They are based on the evaluation of pixel intensity dispersion R_q parallel to the membrane surfaces. Here, the second algorithm condenses 3D reconstructions or the 2D EDX maps into 1D profiles normal to the membrane surfaces which represents the pixel intensity dispersion as a function of the distance to the membrane surface. Finally, *SEM-mean* method (cf. Section 4.5), is based on evaluating histograms of single-pore imbibition lengths obtained manually from the probed sample cross-sections of AAO and CPG.

Introduction

The imbibition fronts are indicated by peaks of image properties extracted from microscopic raw data as function of the distance D to the membrane surface. The average imbibition front positions L_a correspond to conspicuous points that can be determined unambiguously. However, the direct algorithmic determination of imbibition front widths would require the identification of the two imbibition front onset points. The onset of an imbibition front is indicated by a subtle change in the regional curvature of a raw curve exhibiting noise on local length scales. Any numerical D values of discrete onset points will sensitively depend on how the indispensable curve fitting procedure is carried out. Moreover, the curvature changes per distance interval ΔD in the onset region is close to zero over a larger D range so that criteria for the rational positioning of discrete onset points can hardly be defined. Therefore, the direct determination of imbibition front widths is associated with significant uncertainties. Measures of the dispersion of the peaks indicating the imbibition front are more robust, albeit indirect, descriptors of the imbibition front width.

In summary, the imbibition of PS into AAO and CPG was studied with phase-contrast X-ray CT and compared with results from traditional microscopy techniques such as SEM and 2D EDX mapping. To evaluate the results from each technique semi-automatic algorithms were developed to obtain the positions of the imbibition front and the imbibition front widths. X-ray CT allows the algorithmic evaluation of volumetric reconstructions of imbibition morphologies to study characteristic features with characteristic length scales in the range from a few tens of microns down to the submicron scale, not possible with averaging methods, and with high validity, not possible with microscopy.

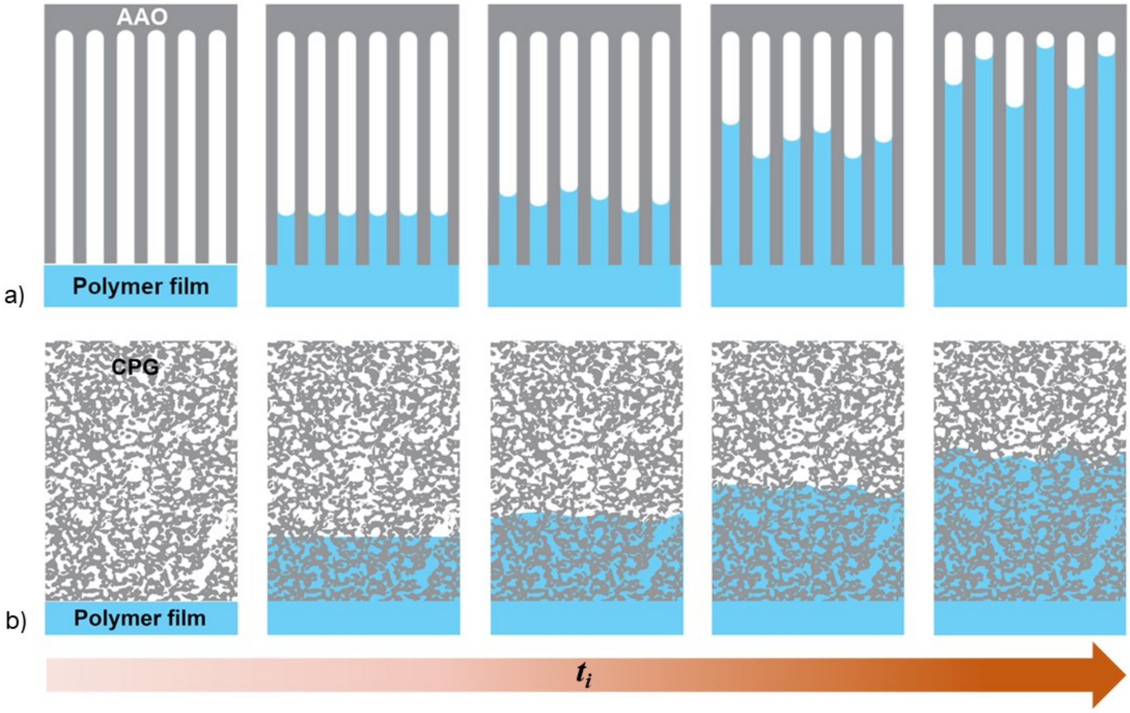

Figure 1.1. Schematic representation of a) AAO and b) CPG membranes (gray) infiltrated with polymer (blue). With increasing imbibition time t_i (from the left to the right), the average position of the imbibition front L_a, and the width of the imbibition front increase.

Introduction

2 State of the art

2.1 Porous materials

According to the IUPAC recommendations a porous solid is “any solid that contains cavities, channels or interstices”.[72] Properties such as density, thermal conductivity and strength depend on the pore structure of the material. However, the morphological description of most common porous materials is complex for reasons such as different pore shapes throughout the solid, interconnected pores, and pore size distributions.[72] Therefore, some conventions have been made. For simplicity, the shape of pores is described in terms of cylinders, cavities, slits, prisms, solid spheres or the voids between solid particles.[72] When the shape of the pores of a solid is well defined and known the pore size becomes a major parameter with precise meaning, generally referred to pore width.[72]

Porosity ε is one of the most crucial morphological properties of a porous material and it is defined as the “ratio of the total pore volume V_p to the apparent volume V of the particle or powder (excluding interparticle voids)” by the IUPAC.[72] The chemical reactivity of the solid and the physical interactions of solids with liquids and gases are properties influenced by the porosity.[72]

In most cases porous solids are complex systems with chaotic pore spaces and a broad range of pore sizes. The complexity of these systems originates from the paths available for fluids to advance, tortuous instead of straight, giving rise to the concept of tortuosity.[73] Tortuosity is a concept used to characterize the structure of porous materials, however there is no canonical definition of it. According to Ghanbarian "…no consensus has emerged unifying the models in a coherent way."[73] Often, tortuosity is defined as the ratio of the lengths of a curvilinear percolation path and the linear distance between two points in a porous matrix.[73-74] Additionally, Comiti showed that the nature of percolation paths through a pore model and, therefore, the tortuosity mainly depends on the porosity.[75]

There is a large variety of porous materials available, found in nature like rocks and soil, as well as man-made, like AAO[25] or CPG,[27] ordered or disordered and straight or sinuous pores. The fabrication of porous materials is diverse, however, Meyer et al. mentioned three main routes of fabrication for porous materials with an irregular pore structure, aggregation or agglomeration, recrystallization and subtraction or addition.[76] An example of aggregation are macroporous silica gels, which can be obtained by hydrothermal treatment of polysilicic acids, by controlled sintering or by sol-gel method. In the case of recrystallization, some zeolites and porous aluminum oxide are examples. Finally, the route of subtraction or addition where some parts of the solid are selectively removed or added, for example, CPG and carbon molecular sieves.[72, 76]

Porous materials with a regular structure can be naturally occurring or synthetic like zeolites which are aluminosilicate materials with basic building blocks of SiO_4 and AlO_4 that form crystalline structures and therefore have regular pore systems with pore diameters in the range from micro- to mesopores.[76] Another example of ordered porous material is self-ordered AAO which is obtained by electrochemical anodization of aluminum substrates and with tailorable pore diameters from a few to a few hundreds of nanometers.[25, 77]

2.1.1 *Self-ordered anodic aluminum oxide*

Self-ordered anodic aluminum oxide (AAO) is a synthetic material with a regular porous structure consisting of straight cylindrical pores ordered in a hexagonal lattice with tailorable diameters and length and hydroxyl-terminated pore walls grown by electrochemical anodization of aluminum.[25] The growth mechanism has been tried to be explained with different theories but still in 2021 Liu et al. stated that "…there is currently no single theory that can systematically explain all the phenomena in the experiment".[61] It is resistant to organic solvents, stable at temperatures in which polymers can be processed and can be selectively removed with acidic or basic solutions.[20]

There are two identified anodization regimes in which AAO can be prepared, mild anodization (MA)[59] and hard anodization (HA).[78] Masuda et al. reported a two-step mild anodization (**Figure 2.1**) in which the disordered aluminum oxide grown in a first step is removed and then a second anodization is carried to produce an arrangement of highly ordered nanopores.[59] The first step involves the production of disordered nanopores in its top part arranged in a hexagonal lattice which is then removed by selective wet-chemical etching leaving indentations arranged in a hexagonal pattern. In the second anodization step, the AAO grows from the patterned aluminum left with hexagonally arranged pores with thickness up to hundreds of micrometers. An schematic representation of the two-step anodization process is shown in **Figure 2.1**.[60] There are three self-organization regimes of MA, and each of them results in different pore diameters and lattice constants. With an electrolyte solution of sulfuric acid and 25 V anodization voltage, 25 nm pore diameter and 65 nm lattice constant are obtained,[77] with oxalic acid and 40V, 35 nm pore diameter and100 nm lattice constant are obtained[59] and with phosphoric acid and 195 V lattice constant of 500 nm and 180 nm pore diameter are obtained arranged in hexagonal lattices.[25, 61] The AAO fabricated in the MA regime has pore diameter distributions with a dispersity of less than 8%.[20] Nielsch et al. reported that for self-ordered AAO, independently from the anodization conditions the porosity is always around 10%.[79] However, porosities up to 50% can be obtained by isotropic wet-chemical widening of the pores.[20]

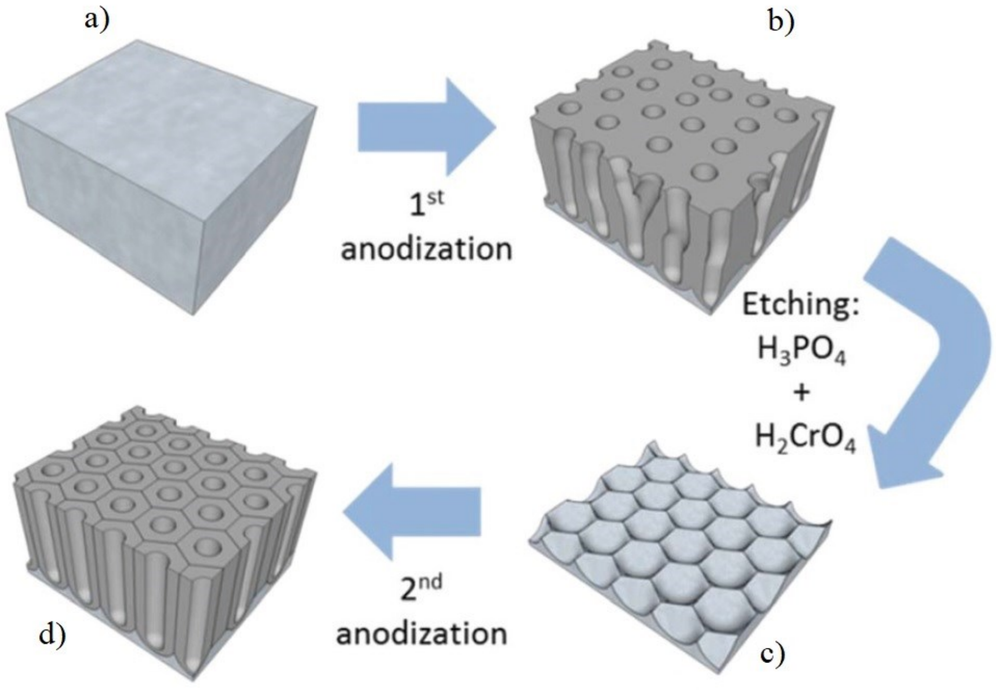

Figure 2.1. Schematic representation of the two-step anodization process to obtain self-ordered anodic aluminum oxide in the mild anodization regime. a) Aluminum substrate before anodization. b) After first anodization, alumina pores hexagonally ordered at the bottom and disordered at the top are formed. c) Alumina is removed with chemical etching and d) straight AAO with pores grown normal from the patterned aluminum substrate from c). Adapted from [60].

Le Coz et al. employed field-emission gun transmission electron microscopy (FEG-TEM) and EDX chemical analysis and mapping to described the structure (**Figure 2.2**) and chemical composition of the AAO basic cell obtained in the MA regime with phosphoric acid.[80] The basic AAO cell consists of an “skeleton” part with hexagonal structure mostly made up of alumina. An internal part which includes a high content of phosphorus. Additionally, evidence of an interstitial rod was observed for the first time but its chemical composition could not be determined.[80]

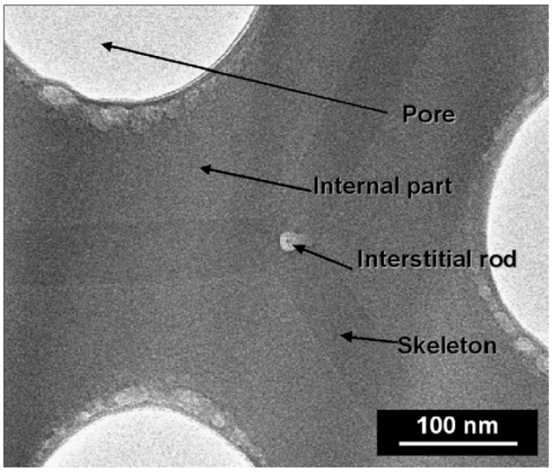

Figure 2.2. FEG-TEM image from the basic cell of self-ordered AAO showing the relatively pure alumina "skeleton", the internal part which includes a high content of phosphorus, the interstitial rod and the pores. Reproduced from [80].

An AAO membrane consists of several basic cells, arranged in a hexagonal lattice with in which every single pore is oriented strictly normal to the AAO surface and the length of the pores corresponds exactly to the thickness of the membrane. Therefore, AAO is a nearly ideal pore system with tortuosity close to 1. In **Figure 2.3**, SEM images shows the cross-section on an AAO membrane parallel to the pore axes and the AAO pore mouths with ≈ 380 nm pore diameters and 500 nm lattice constant.

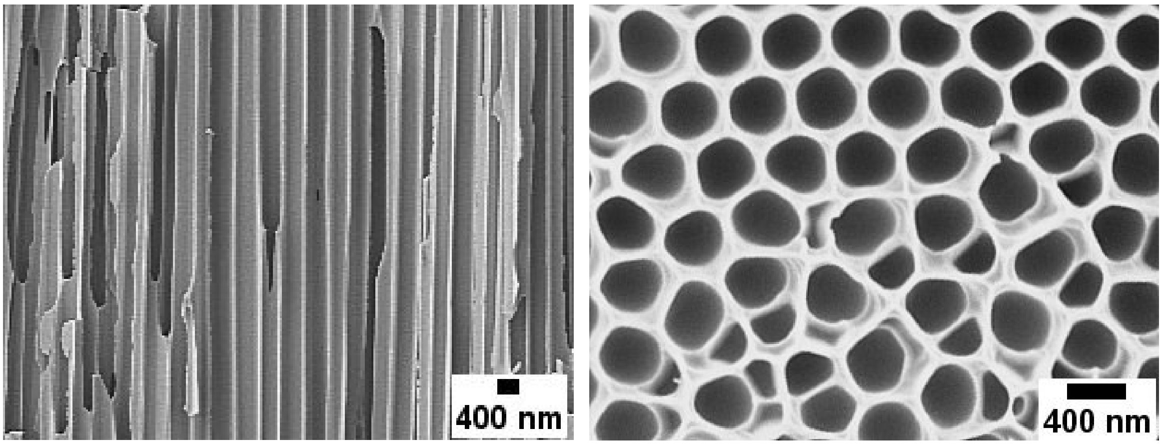

a) b)

Figure 2.3. Scanning electron microscopy (SEM) images from SESI detector (a), and InLens detector (b) of self-ordered anodized aluminum oxide (AAO). a) Cross-section of AAO parallel to the pore axes with ≈ 380 nm pore diameters. b) Pore mouths of AAO with ≈ 400 nm pore diameters.

The hard anodization (HA) regime is performed at higher anodization voltages and overcomes some disadvantages of MA like long fabrication time and narrow processing windows for AAO growth. AAO with 220-300 nm lattice constants and 49-59 nm pore diameters is obtained by HA with oxalic acid solutions and anodization voltages between 120 -150 V.[20] MA and HA regimes are summarized in **Figure 2.4**.

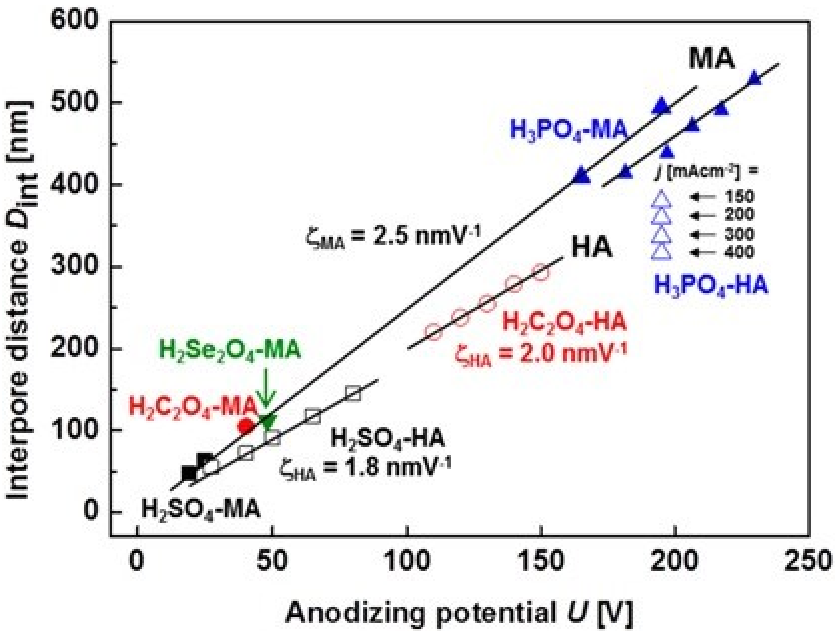

Figure 2.4. Overview of self-ordering MA and HA regimes currently identified. Reproduced from [81].

AAO fabrication is not limited only to self-ordered straight cylindrical pores, long-range ordering of AAO can be obtained by hard imprint lithography in which different pore morphologies and lattices can be pre-patterned in the Al substrates which the oxide will use to grow.[20] Complex pore architectures can also be fabricated, for example, with pulsed anodization where the anodization potential is applied in pulses to obtain variable pore diameter along the axis parallel to the AAO pores.[82]

Due to its tailorability, optical and electrical properties and large surface area, AAO is an important material for several applications such as template-assisted fabrication of nanostructures, data storage, energy generation, sensing devices, photonic crystals, filtration, etc.[60-61] Additionally, the isolated straight cylindrical pores with tunable diameters and tortuosity close to 1, makes AAO an ideal material as a reference for the study of liquid invasion of porous materials.[8, 17, 21, 44, 47-48] An overview of some AAO applications is shown in **Figure 2.5**.

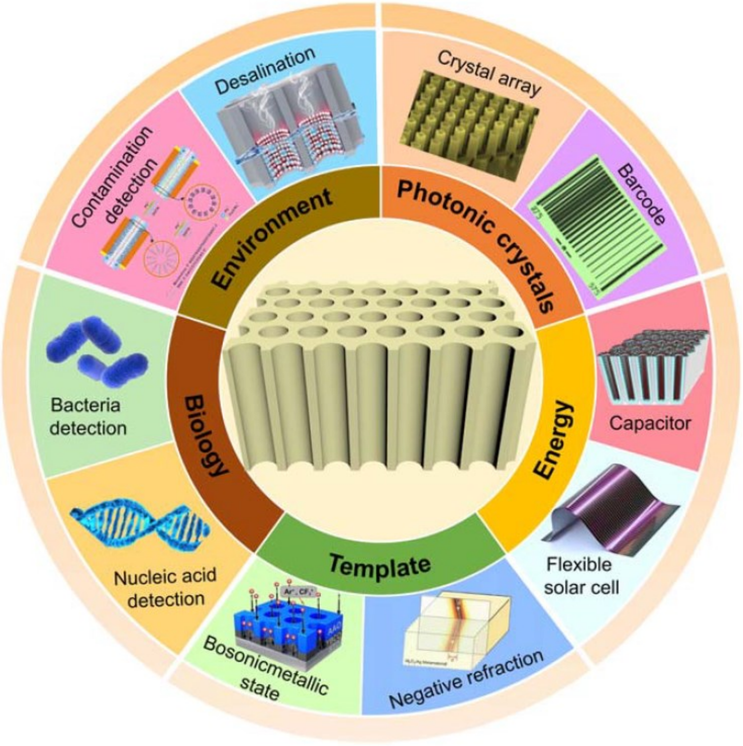

Figure 2.5. Overview of some AAO applications. Reproduced from [61].

2.1.2 *Controlled porous Glass*

Porous glasses belong to the disordered porous materials type, Janowski et al. stated that they "are one of the most investigated and characterized porous materials".[83-84] From around 1926, the separation of glasses that contain boron into phases was known[83-84] and was later exploited by Hood and Nordberg to develop what is known today as the VYCOR®-process.[85] Vycor porous glasses (VPG) are alkali borosilicate glasses (Na_2O-B_2O_3-SiO_2) within a special composition range that separate with a heat treatment into acid-soluble and acid-insoluble phases. One of the phases can then be removed by selective leaching resulting in a sponge-like structure with 4-9 nm pores.[83-84] Additionally, Vogel reported that phase separation occurs in a wide range of compositions.[86]

Haller developed the basics to prepare controlled porous glasses (CPG) with a narrow pore size distribution.[87-89] The basic procedure to prepare CPG consist of four steps.[83-84] In the first step, an alkali borosilicate glass melt in the zone of the boric acid anomaly[90] is formed (**Figure 2.6a**). Second, the melt is quenched to a temperature, between 580 and 700 °C, in which spinodal decomposition occurs and the melt separates into silica-rich phase and a sodium-rich borate phase (**Figure 2.6b**). The melt then is vitrified and can be formed in different shapes. Third, the vitrified glass is reheated for a certain time in order to induce phase separation and coarsening of the microheterogeneities. Finally, the sodium-rich borate phase is removed by acid/alkaline treatment to remove silica residues in the pores (**Figure 2.6c,d**).[83-84] The obtained porous glass consists of a sponge-like interconnected network of pores **(Figure 2.7**).

Enke et al. stated that "The mechanism of phase separation during the preparation process of porous glasses is controversially discussed in literature".[27] The most preferred mechanism is spinodal decomposition, in which the phase separation happens when unstable concentration fluctuations characterized by a long wavelength grow.[27] Yazawa et al. found not only clear evidence of phase separation through spinodal decomposition but also how parameters such as cooling rate, amplitude and wavelength of concentration fluctuations affect the resulting textural parameters i. e. pore volume or surface area of the porous glass.[91]

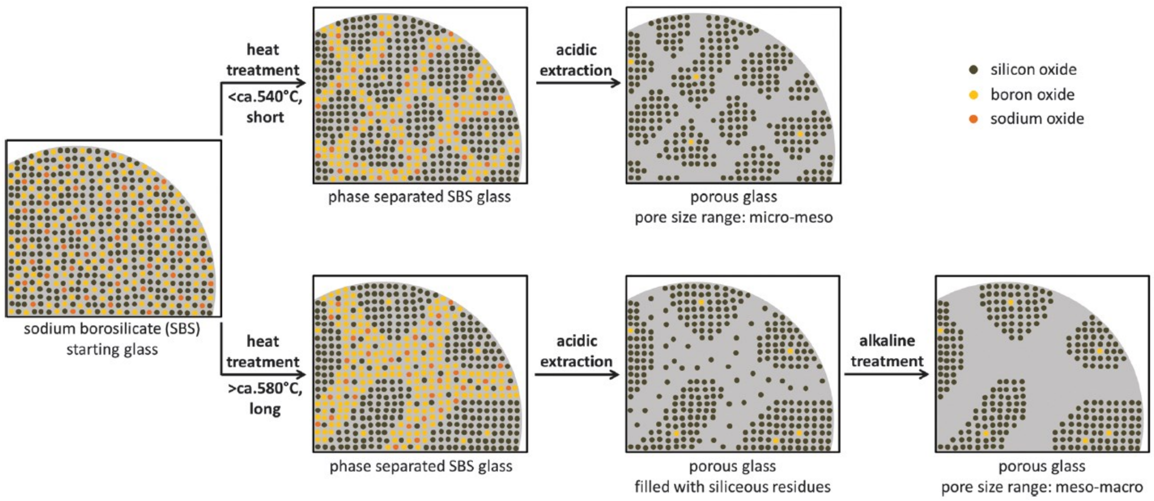

a) b) c) d)

Figure 2.6. Schematic representation of the process to produce CPG. a) Starting alkali borosilicate glass in the zone of the boric acid anomaly. b) Phase separation by spinodal decomposition into a silica-rich phase and a sodium-rich borate phase. c) Extraction of the sodium-rich borate phase with acidic treatment. d) Extraction of the silica residues inside the pores with alkaline treatment. Adapted from [92].

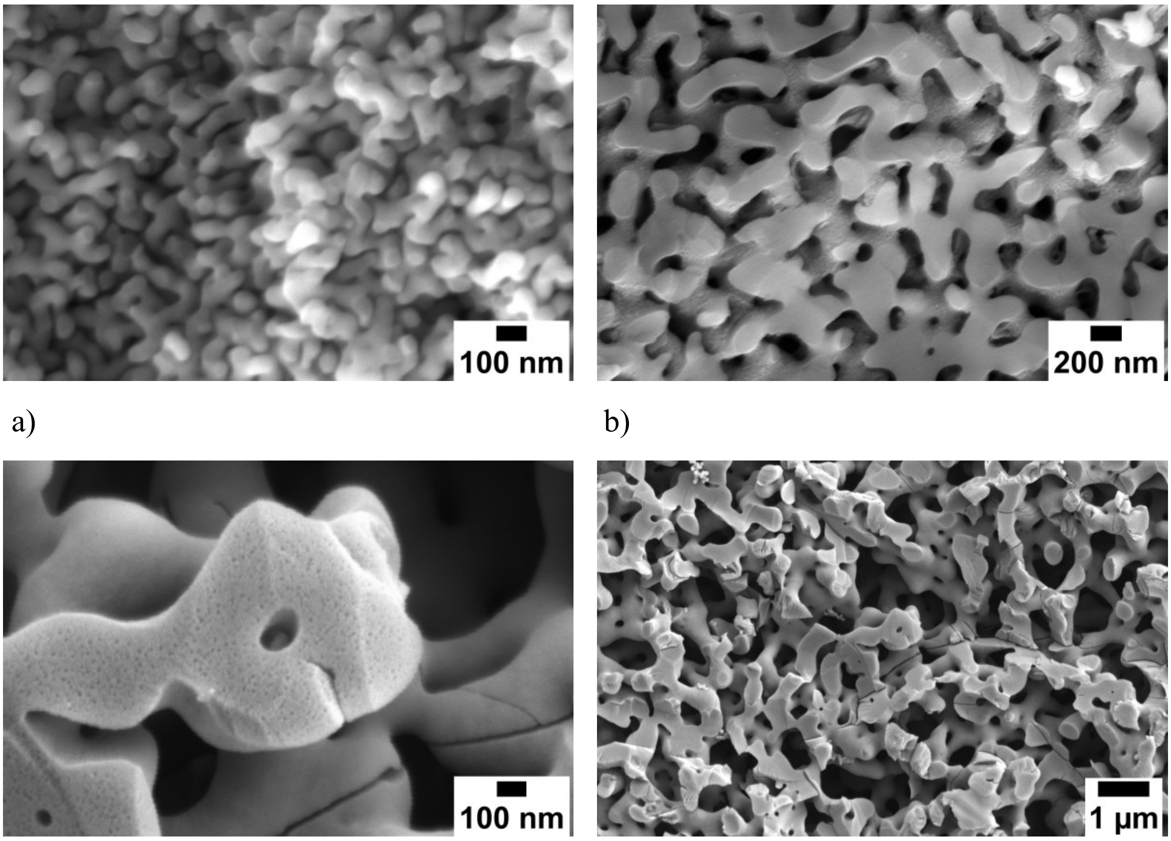

a) b)

c) d)

Figure 2.7. SEM images of controlled porous glass (CPG) morphologies with different mean pore diameters a) Surface of CPG with ≈ 40 nm pore diameter, b) Surface of CPG with ≈ 200 nm pore diameter, c,d) Surface of CPG with ≈ 300 nm pore diameter at different magnifications. The images were acquired with a SESI detector.

Controlled porous glasses, prepared in the ways mention above, are highly valuable porous materials due to - as their name says - controllable characteristics. According to Janowski et al., porosity as well as the number, size and form of the pores and pore size distribution are strongly influenced by the composition of the alkali borosilicate glass. Thus, the textural properties of the CPG will depend on the content of the sodium rich borate phase that can be leached.[83]

Additionally, due to hydroxyl groups covering the surfaces of CPG's a large number of chemical modifications of the surface are possible. The CPG's mechanical stability make them also perfect materials to be formed in various monolithic shapes such as membranes, tubes, rings, etc.[83-84] Inayat et al. reported that a combination of phase separation and sintering make the fabrication of porous glasses with hierarchical pores possible and stretch-drawing of bundles of glass monoliths while heated to the softening point will result in hierarchical pores that are also aligned.[92]

The above mentioned characteristics of CPG make it an important porous material for the study of spontaneous imbibition of liquids[41] and the behavior of fluids under confinement[93] as well as for membrane science.[94] CPGs may also be used as active ingredient depots.[12] CPG has been extensively used for the study of imbibition with different types of liquids and by different techniques as it is a porous model system that resembles porous materials found in nature and because it provides a robust and reproducible porous model with tailorable characteristics.[15, 41, 50, 52, 95]

2.1.3 Characterization of porous materials

The specific textural characteristics of each material such as pore size distribution, porosity, or specific surface area are important characteristics of porous materials, and they can be characterized nowadays by a collection of different methods that rely on different physical principles.[76, 96] According to Rouquerol et al. the characterization methods can be listed in four categories, liquid intrusion-extrusion, liquid permeametry, phase change in a confined medium and imaging.[96] Imaging methods will be discussed in a subsection "Characterization of imbibition state of porous materials" as essentially the same imaging methods are used for as-prepared and infiltrated porous materials. In **Figure 2.8**, the most common methods and the length scales in which they are able to provide us information on the textural characteristics of the materials are summarized.

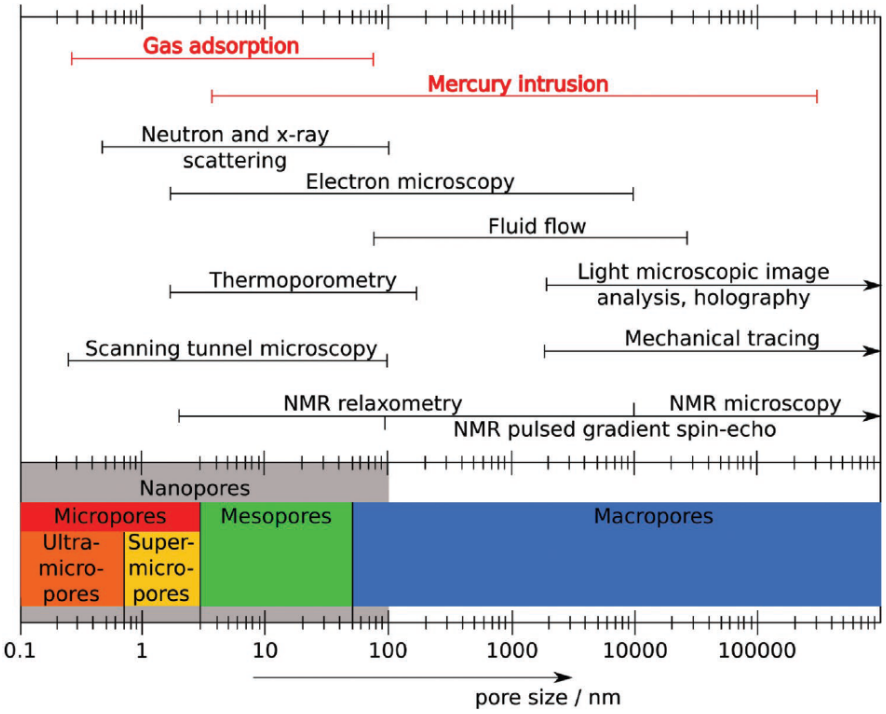

Figure 2.8. Pore size analysis ranges of common characterization techniques for porous materials. Reproduced from [97].

Mercury intrusion is widely accepted and considered the state of the art method of the liquid intrusion-extrusion family to characterize macropores in materials like catalysts or building materials.[97] It is useful to investigate the tortuosity, permeability, fractal dimension and compressibility of porous solids as well as to acquire information on the pore shape, network effects and skeletal and bulk density.[98] Mercury does not wet most of the materials at room temperature. Therefore, it needs to be forced into the material with pressure. From the intruded volume V_{Hg} versus pressure p, intrusion-extrusion curves **(Figure 2.9**) one can obtain information on pores with diameters in a range from ≈ 4 nm to more than 400 µm.[98] The main limitations of mercury intrusion are issues related to environment and health. Therefore, possible liquid metal replacements are currently being researched like Gallium or Indium.[97] Water intrusion can provide information on the mesoporous range but it can be extended provided that the material is hydrophobically modified.[96]

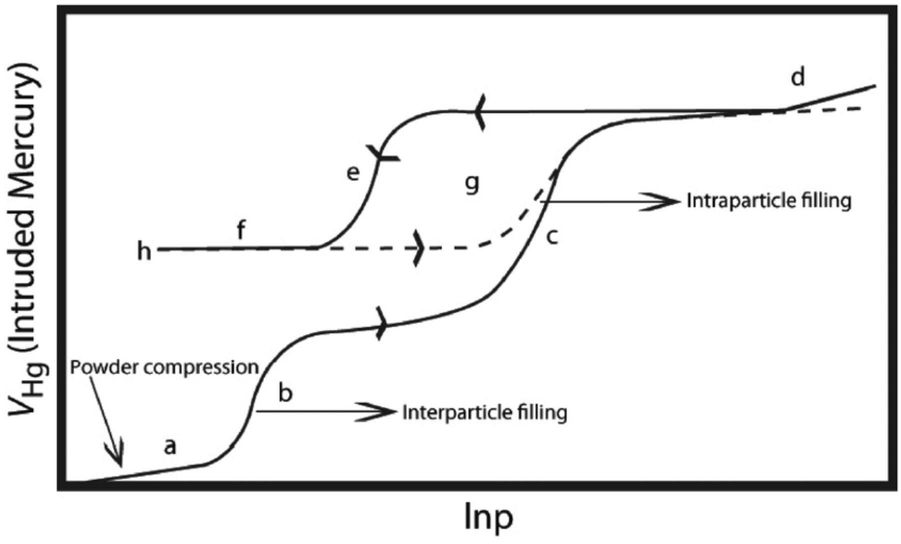

Figure 2.9. Schematic volume of intruded mercury versus pressure curve showing different stages of the process. a) Rearrangement of particles in the powder bed. b) Intrusion of particle voids. c) Pore filling. d) Reversible compression for some materials. e) Extrusion of mercury. f) Mercury is retained inside the pores, preventing the loop from closing. g) Further intrusion-extrusion cycles. h) mercury entrapment or hysteresis. Reproduced from [98].

Liquid permeametry relies on the pumping of liquid through the membrane to be probed at a known flow rate while the pressure drop is measured. It provides information on the estimated hydraulic pore radius in the range of 0.1 to 1000 µm. It is a simple method with no standard equipment available. A drawback is that it does not provide a pore size distribution but a hydraulic radius which normally shifts towards pore sizes with broadest dimensions.[96]

The family of phase change methods relies on the condensation, freezing and melting of different liquids inside the porous materials detected by different methods. Two examples are thermoporometry and cryoporometry, the first relies on the freezing-melting of water or hexane with slow cooling or heating rate detected by differential scanning calorimetry (DSC) and is useful in the meso- and macroporous range. The second relies on the freezing-melting of a liquid detected by nuclear magnetic resonance (NMR) with same slow cooling rates as with thermoporometry and it is useful for pores between 10 nm to 1000 nm.[96]

2.2 Imbibition of Porous Media

2.2.1 General considerations

To understand the process of imbibition, it is helpful to introduce first the wetting of a flat surface at the microscopic level. According to Young's law (Equation 2.1),[99] the wetting state of the fluid can be directly obtained when the three surface tension are known.[100]

$$\gamma_{SV} = \gamma_{SL} + \gamma \cos \theta_{\mathrm{eq}} \qquad \text{(Equation 2.1)}$$

where γ_{sv} is the solid-vapor surface tension, γ_{sl} is the solid liquid surface tension, $\gamma \equiv \gamma_{\mathrm{lv}}$ denotes the liquid-vapor surface tension and θ_{eq} denotes the contact angle formed between the liquid-vapor surface tension γ_{LV} and the solid-liquid surface tension γ_{LS} contact lines. (**Figure 2.10**).

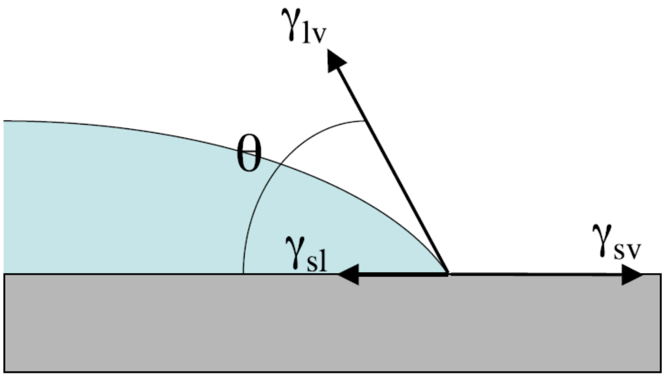

Figure 2.10. Schematic diagram of a solid surface with a drop of liquid on it. The equilibrium contact angle θ_{eq} is the angle formed between the liquid-vapor surface tension γ_{LV} and the solid-liquid surface tension γ_{LS} contact lines. The solid vapor surface tension is denoted by γ_{SV}. Reproduced from [100].

The ability of a liquid to wet a surface is determined by van der Waals and electrostatic forces and is commonly measured by an equilibrium contact angle θ_{eq}.[100] When θ_{eq} is larger than zero there is partial wetting and the liquid takes the form of a sessile drop on the surface with a microscopically thin layer absorbed on the surface surrounding the drop (**Figure 2.11**). If the equilibrium contact angle equals to zero, there is complete wetting and the drop of liquid spreads entirely over the surface. When the surface is large enough that it can be considered “infinite”, the film spreads in the form of a “pancake” structure, which means the film covers a finite area with a thickness larger than a monolayer due to long-range interactions between the solid and the liquid and cohesion between the liquid.[20] At the spreading front, a precursor film thinner than a monolayer occurs as a transient feature during spreading. Polar inorganic surfaces usually have high surface energies while the surface energies of organic fluids and polymer melts are typically lower by one order of magnitude.[20] In this regard, evidence of a precursor film has been found even for viscous polymeric fluids.[101-102]

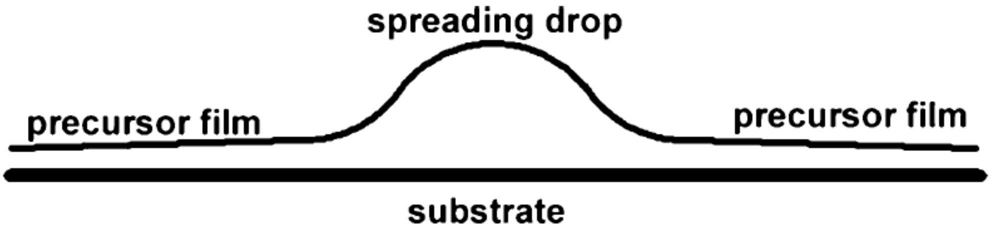

Figure 2.11. Schematic diagram of the spreading of a liquid drop on a flat substrate. Reproduced from [20].

To differentiate between the wetting states of a system the equilibrium, the spreading coefficient S_{eq} (Equation 2.2) representing the surface free energy relative to its value for complete wetting is employed.[100]

$$S_{eq} \equiv \gamma_{SV} - (\gamma_{SL} + \gamma) = \gamma(\cos\theta_{eq} - 1) \qquad \text{(Equation 2.2)}$$

When $S<0$, a drop with a finite contact angle will form, meaning partial wetting and if $S>0$ the fluid will spread with a contact angle of zero meaning complete wetting.[102]

2.2.2 Imbibition at the single-pore level

The flow of a liquid into cylindrical channels has been arduously investigated, both theoretically and experimentally as this process is far from being trivial.[20] Nevertheless, in 2010, Engel et al. argued that "…there exists no description of the filling behavior of liquids, especially of polymer melts into nanopores in literature that is experimentally and theoretically consistent…".[22] In 2019, Singh et al. stated that "…there is yet no consensus on how wettability controls the physical processes that underlie the dynamics of an invading liquid at the pore scale."[26]

The wetting in a single-pore scenario is different than the wetting of a flat substrate in the sense that a real-life pore has a "finite" length and volume that is frequently smaller than the volume of the fluid being infiltrated.[20] Lenormand described spontaneous imbibition as a process where in a porous medium an invading wetting fluid displaces a receding non-wetting fluid.[1] In this scenario, the two fluids are considered immiscible. The opposite case, where the non-wetting fluid displaces the wetting fluid was described as drainage. The two immiscible fluids will form a meniscus with a contact angle at the interface of the capillary wall and the wetting fluid depending on factors such as pore geometry, and surface-liquid interaction.[1] A schematic representation of imbibition into a capillary is seen in **Figure 2.12.**

Around a hundred years ago, Lucas in 1918[103] and Washburn in 1921[104] defined what would be the basic equation to describe the dynamics of capillary flow (Equation 1.1) that describes the distance a liquid travels through a single cylindrical pore as well as a porous body, which Washburn stated "behaves as an assemblage of very small cylindrical capillaries".

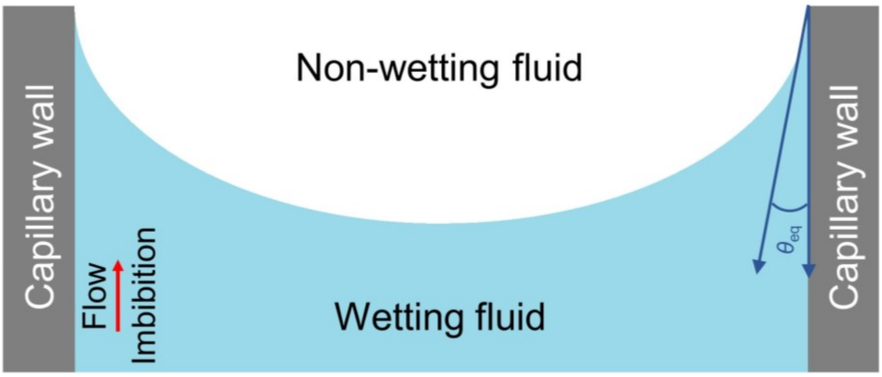

Figure 2.12. Schematic representation of imbibition into a capillary, where a wetting liquid displaces a non-wetting liquid. The equilibrium contact angle is θ_{eq}.

The classical Lucas-Washburn theory[103-104] assuming lamellar flow of an invading fluid through ideal cylindrical capillaries uniform in diameter predicts a value of 0.5 for the exponent n of t_i. If the exponent n is set to 0.5, Equation 1.1 (cf. Chapter 1) is suitable to describe processes that slow down with time – as it is commonly observed for the imbibition of fluids into pores. Therefore, the value 0.5 for n is typically accepted without further questioning. This time scaling results from a dynamic balance of a constant driving Laplace pressure at the advancing imbibition front and a linear increase in viscous drag in the infiltrated part of the cylindrical capillary behind the imbibition front.[13, 105-106] Thus, any changes in the capillarity of the liquid, the liquid-solid interaction or the hydraulic permeability as a function of time during the imbibition process can lead to deviations from the classical Lucas-Washburn scenario.[106] Experimentally observed deviations from the Lucas-Washburn model were ascribed to “dead layers” of adsorbed molecules of the invading species on the pore walls,[14-17] as well as to thermal fluctuations, van der Waals forces and hydrodynamic slippage.[13, 18] Slippage and the extend of it was found to depend for chain molecules, i. e. polymers, on the length of the chain, density of entanglements and the surface chemistry.[18, 101] Moreover, single-pore imbibition is characterized by a broad phenomenology of transient nanoscopic single-pore imbibition morphologies often characterized by the presence of precursor films (**Figure 2.13**).[19-20, 107]

Additionally, Quéré[108] argued that “Close to the moment when the tube touches the liquid, Washburn’s law leads to an unphysical infinite velocity of imbibition…” Therefore, “…inertia must be considered at that particular moment.” In this initial moment, a linear relationship of the imbibition length and imbibition time ($L_s \sim t_i$) precedes the Lucas-Washburn dynamics.[108]

When the imbibition on single pores departs from capillary wetting (**Figure 2.13a)**, the occurrence of thin precursor films (**Figure 2.13b**) of the invading liquid that follow a $\sqrt{t}$ law but with larger imbibition speeds v than that of the menisci movement have been reported in several studies.[107, 109-110] The precursor films can develop into imbibition states of complete filling of the pore by different mechanisms. Engel et al. reported thickening of precursor films during the filling of pores (**Figure 2.13c**).[22] Another reported[111-112] morphology is due to the “snap-off” mechanism in which after the formation of a precursor film, instabilities of the film occur along the pore walls and menisci form at those positions.

The menisci formed will advance in opposite directions as the amount of liquid entering the pores increases (**Figure 2.13d**).

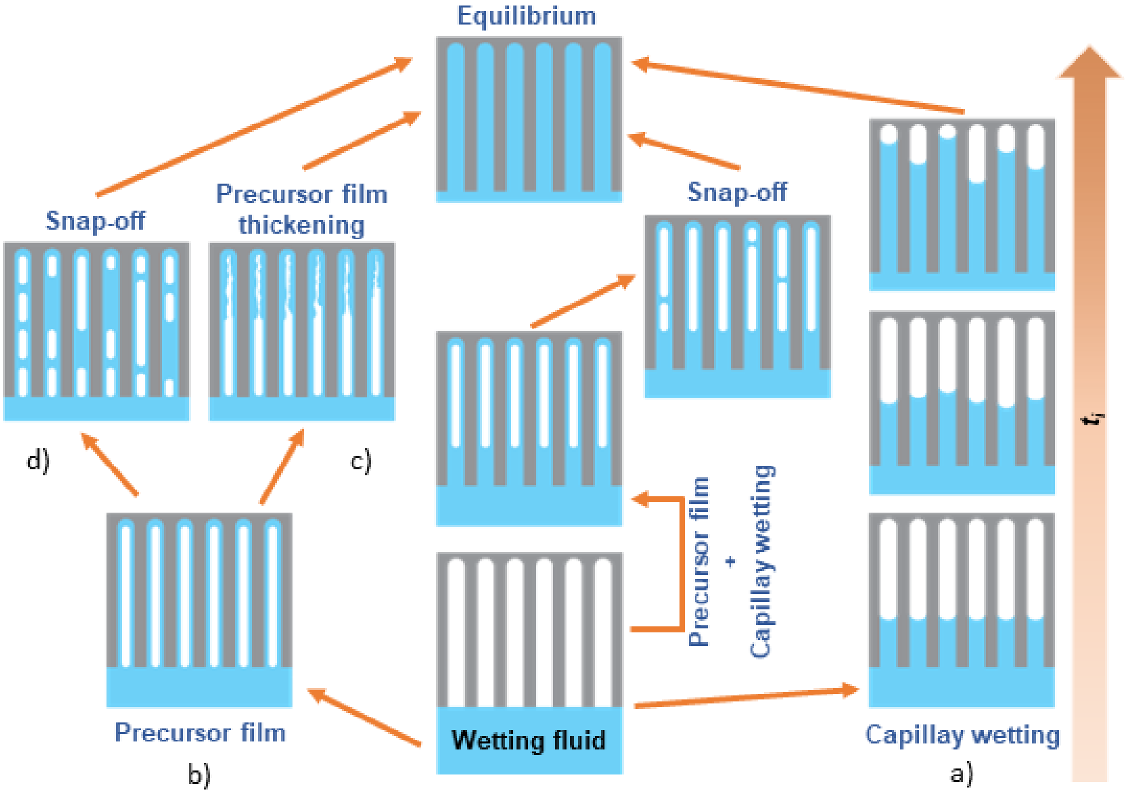

Figure 2.13. Overview of imbibition phenomenology with transient imbibition morphologies on a single-pore level.

As mentioned above, the presence of “dead layers” of immobilized molecules from the invading liquid on the pore walls, also called “dead zone”[17] (**Figure 2.14**) is another way in which imbibition deviates from the classical Lucas-Washburn dynamics due to an increase in effective viscosity and has been reported extensively.[14-16, 46, 113] Yao et al. reported that for polymers, the inner walls of the pores can strongly absorb nearby polymer chains creating a “Dead zone” of immobile polymer chains with thickness Δb, this results in a decrease of the pore radius b_0 to an effective radius b_{eff}, which influences the imbibition speed (**Figure 2.14**). Polymer melts beyond the dead zone show the usual macroscopic flow with parabolic profile. The authors stated that the “dead zone” effect is dominant when the radius of gyration is $R_g << b_0$.[17]

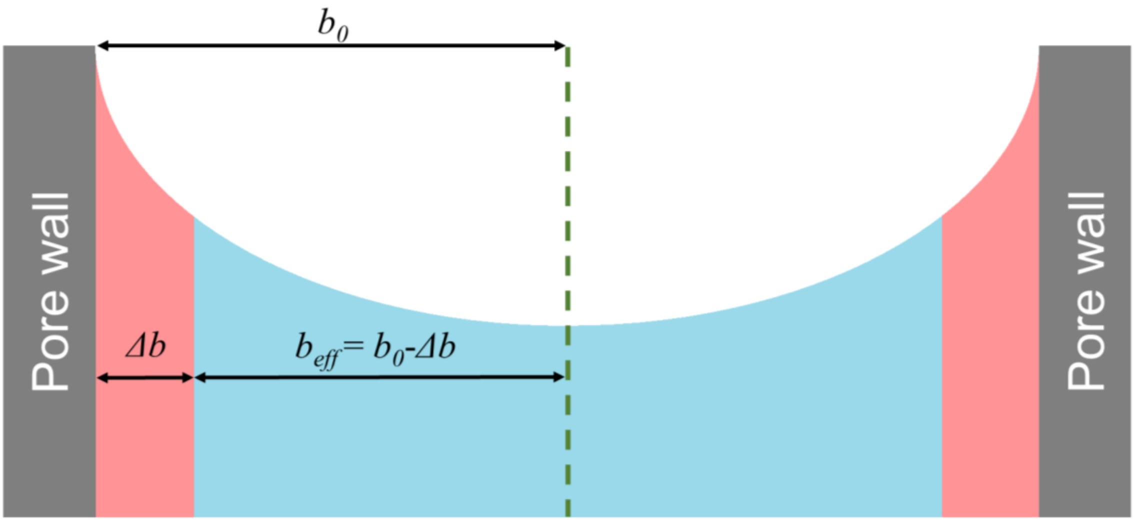

Figure 2.14. Schematic representation of the “Dead zone” with a thickness Δb (red), formed by strongly-absorbed molecules of the infiltrating fluid (blue) on the surface of the pore walls (gray). The dashed green line corresponds to the axis of the pore.

Moreover, Cai et al. stated that “The geometry of a capillary tube has a significant impact on capillary imbibition.”[106] Considerable efforts have been directed to describe imbibition in different pore geometries such as non-uniform cylindrical capillaries, i.e. conical or tortuous, as well as capillaries with triangular, square or rectangular cross-sections (**Figure 2.15**).[106]

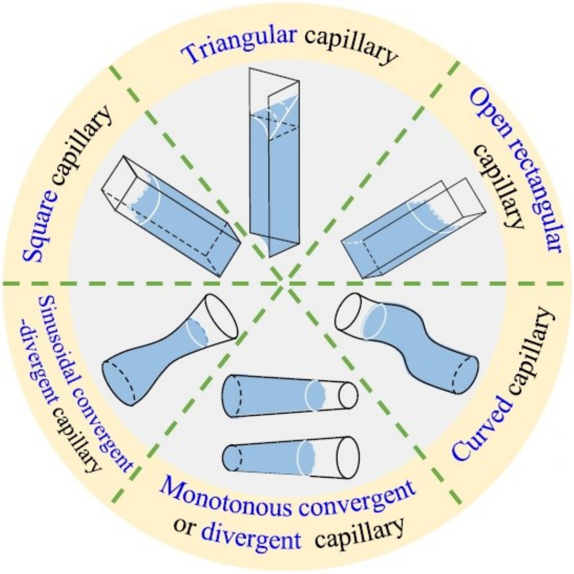

Figure 2.15. Schematic overview of imbibition into capillaries with different geometrical cross-sections and axial variations. Adapted from [106].

Departures from an ideal cylindrical pore geometry can lead to deviations from the classical proportionality of the average imbibition front position L_a to $t_i^{1/2}$. Already conical pore shapes may result in an exponent n of t_i of 0.25.[24] Real-life porous model matrices, such as self-ordered nanoporous anodic aluminum oxide (AAO),[25] may contain isolated parallel cylindrical pores nearly uniform in diameter along their pore axes. However, the AAO pore arrays may exhibit a certain pore diameter dispersion in turn causing dispersion of the single-pore imbibition lengths L_s[41, 49] and, consequently, imbibition front roughening.[23]

Besides, Cai stated that the tortuosity of the porous media "…plays and important role in describing fluid flow characters such as permeability, effective diffusivity, and flow resistance in porous media."[33] Therefore, several attempts[50, 114-117] have been made to modify the Lucas-Washburn law to account for the tortuosity. For example, Lundblad and Bergman adapted the Lucas-Washburn law by replacing in the prefactor the capillary radius by an effective hydraulic radius (**Figure 2.16**).[117]

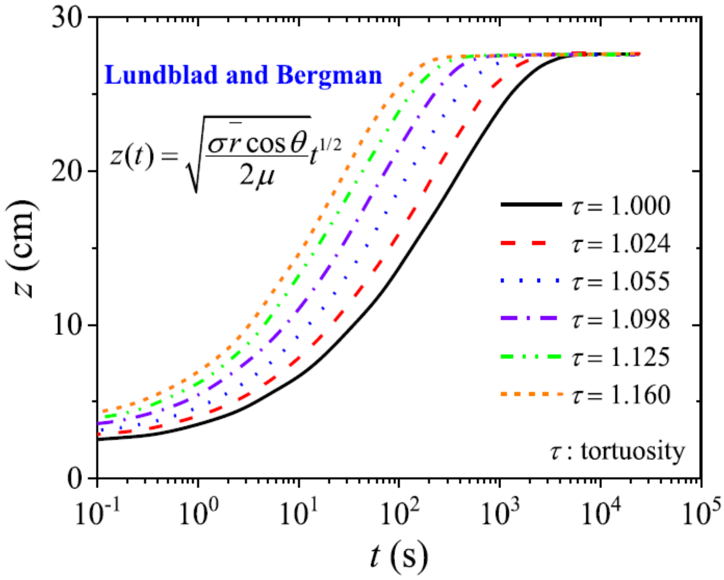

Figure 2.16. Imbibition length z vs imbibition time t in porous media with different tortuosities. Adapted from [106]

2.2.3 Imbibition in interconnected pore models

Imbibition that takes place inside porous materials that contain tortuous interconnected pores such as CPG differs from imbibition into single-pores such as in AAO. In such cases, single-pore imbibition phenomena are superimposed by cooperative effects related to the presence of hydraulically coupled menisci at the imbibition front.[2, 30-32] Cai and Yu state "…that most values of time exponent are less than 0.5. This may be explained that the LW equation may not be well suitable to depict the imbibition in a complex tri-dimensional porous medium. (…) The anomalous value of time exponent (<0.5) suggests that the imbibition speed becomes slower than that of pure considerations of capillary pressure and viscous drag as the average interface height increases."[33]

If local variations of the pore diameters of the porous matrix exist at the imbibition front, menisci in different pores have different curvatures so that the Laplace pressure across these menisci varies. These pressure differences between hydraulically coupled menisci cause in turn cooperative changes of the imbibition front topography resulting in avalanche-like relaxations,[34-38] viscous fingering[35, 39] and imbibition front roughening.[35, 39-42] Thus, modified descriptions of imbibition dynamics considering tortuosity and geometry of the infiltrated pore system were suggested.[43]

Dougherty reported that in Helen-Shaw cells, which have highly interconnected pores, the imbibition front movement is not uniform, instead, some regions stay pinned while others advance. When one of the regions previously immobile starts to move in a sudden way is called an avalanche-like way.[36] Homsy observed instabilities in the invasion of fluids with different viscosities into interconnected porous materials. The author injected water into a Helen-Shaw cell filled with glycerin, where the less viscous fluid penetrates and fingers through the one with higher viscosity (**Figure 2.17**).[39] According to Gruener et al., in an interconnected network of elongated pores (Vycor glass), if the imbibition follows the Lucas-Washburn dynamics, the imbibition front roughening scales with an exponent of time ≈ 0.45, making the ratio of the imbibition front width and the imbibition length a fraction of almost constant value.[41]

Figure 2.17. "Viscous fingering" during the imbibition of water into a Helen-Shaw cell filled with glycerin. Adapted from [39].

2.2.4 *Characterization of imbibition state of porous materials*

The imbibition process is yet not fully understood, especially with respect to the transient states that occur through time during imbibition (**Figure 2.13**). Current efforts aim to analyze the evolution through time of the imbibition length of liquids inside the porous matrix and the imbibition front widening.

The study of imbibition on porous materials requires that the features of interest, such as the imbibition front, the empty pores and the pore walls can be identified. However, most methods especially averaging methods, fail to resolve imbibition lengths and imbibition front widths with features in the submicron range.

Imbibition fronts were, for example, inspected with the naked eye.[44-45] Yao et al. used reflection microscopy (**Figure 2.18**) and SEM to determine the imbibition length of polymer melts with different number of entanglements into AAO. The authors found slower imbibition speeds than the ones predicted by LW scenario for polymers with 27 and 50 entanglements per chain and faster imbibition speeds than expected were observed in polymer melts with more than 50 entanglements per chain.[45]

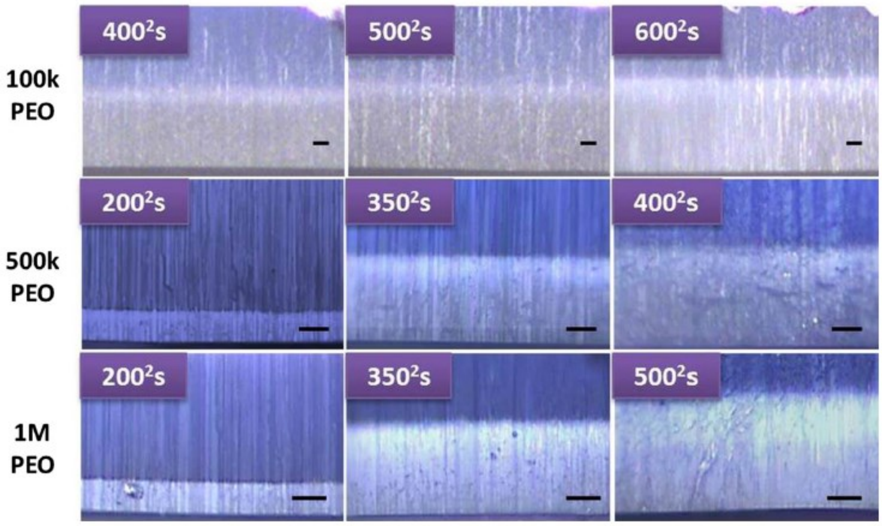

Figure 2.18. Cross-sectional images of imbibition of polyethylene oxide (PEO) with different molecular weights for different times into AAO studied by reflection microscopy. The infiltrated parts are in the bottom of the images, the imbibition front in the center and the top of the images correspond to empty pores. Scale bars are 10 μm. Reproduced from [45]

Imbibition fronts have also been studied by averaging methods, such as small-angle X-ray scattering (SAXS),[22] dielectric spectroscopy,[46-48] neutron radiography,[41, 49] gravimetry[50-52] and opto-fluidic techniques.[19, 53-58] Engel et al. reported the imbibition with polymer melts into ion track etched membranes with SAXS. Imbibition followed a $\sqrt{t}$ law and evidence of a precursor film was found.[22] Cencha et al. stated that "extreme challenges to monitor liquid fronts in nanoscale geometries have resulted in only a few experimental studies on imbibition fronts in nanoporous structures."[19] To tackle this issue, the authors studied the imbibition of glycerol and Polydimethylsiloxane (PDMS) into nanoporous silicon with a specifically designed light interferometry experiment. Their results showed that the spread of a precursor film inside the nanopores by PDMS macromolecules affects the imbibition dynamics.

A powerful way to study imbibition is through imaging methods. Imaging refers to surface visualizations or three-dimensional visualizations of the samples. SEM for example, is a surface analysis technique. However, in combination with a focus ion-beam unit, the surface of the samples can be ablated an imaged several times successively to obtain a reconstructed 3D representation of the probed volume morphology. Drawbacks of this technique include the permanent modification of the original sample by ablation and non-representative sampling due to the small size of the cross-section of the probed sample volume.[96]

A big challenge for imaging techniques arises from the fact that the imbibition front is concealed by the porous matrix.[41] However, nowadays there are techniques that allow the observation of the liquid inside the porous material, such as neutron radiography and tomography[118] and X-ray computed tomography (X-ray CT).[62] Neutron radiography benefits from a larger penetration depth but suffers from a lower spatial resolution compared to X-ray CT. Additionally, with neutrons there is a risk that the sample being probed becomes radioactive. Another drawback from neutron radiography is that it requires a large-scale facility while X-ray CT can be deployed in large-scale facilities and with laboratory based instruments.[65]

X-ray CT is a non-destructive technique which is gaining relevance for applications where the 3D nature of the analyzed samples is important. It relies on the volumetric reconstruction of projections acquired by illuminating the samples with X-rays at several different angles. X-ray CT can be deployed in two modes, absorption, and Zernike phase-contrast. In the absorption mode, the contrast of the acquired images is dependent on the attenuation difference of X-rays after passing through the different materials of the sample (**Figure 2.19a**).[66] There are different ways to obtain phase contrast,[119-120] in one of them, a gold phase ring is located between the sample and the detector. The phase ring produces a phase shift of the diffracted X-ray beam by the sample, resulting in a dark appearance for features with a net positive phase shift (**Figure 2.19b**). The phase contrast boost is due to the un-shifted diffracted light by the sample that interferes with the undiffracted phase shifted light.[63] Garcea et al. stated that "imaging modes that exploit the phase shift can deliver increased feature detectability relative to simple absorption contrast, particularly for weakly absorbing objects".[66]

X-ray CT exists as synchrotron and laboratory-based application. In synchrotron facilities, the volumes analyzed are small and the short acquisition times allow for *in situ* experiments, for example, imaging of developing cracks while the sample is loaded. In laboratory based devices larger samples can be studied but with the drawback of poor contrast and long acquisition times.[66]

Due to the advantages mentioned above, X-ray CT imaging has been extensively used to study both qualitatively and quantitatively porous materials with sub-µm resolution and imbibition of fluids into them.[65, 119, 121] Werth et al. argued that "X-ray methods present the highest resolution and flexibility for 3D natural porous media characterization, and 3D characterization of fluid distributions in natural porous media".[122]

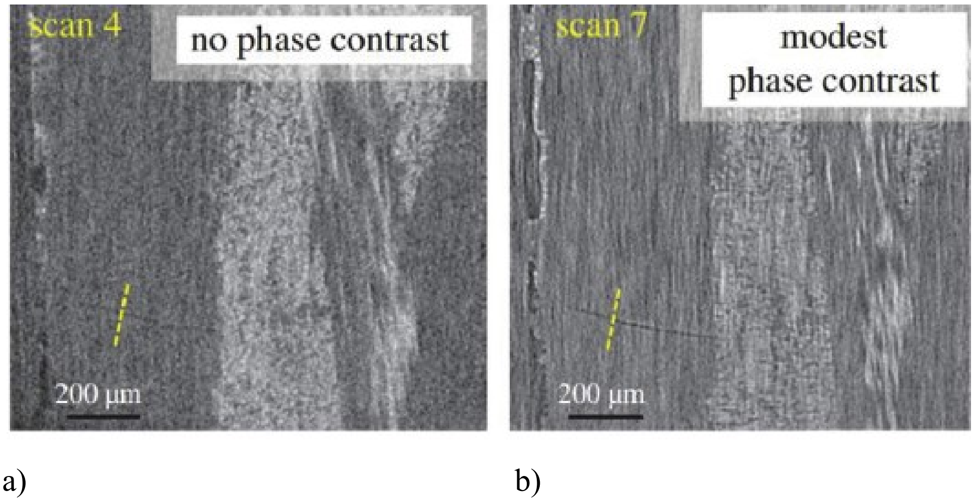

Figure 2.19. Woven glass-fiber cross-sectional images acquired with a laboratory X-ray CT. a) Image acquired without phase contrast, a crack (dashed yellow line) is barely visible. b) Image acquired with phase contrast; the crack (dashed yellow line) is easier to distinguish as well as other interfaces from the sample. Adapted from [66].

3 Materials and Methods

3.1 Materials

Monodisperse sec-butyl- and H-terminated PS (M_w = 239 kg/mol; M_n = 233 kg/mol; PDI = 1.03) was purchased from Polymer Standards Service (Mainz, Germany). Toluene (anhydrous; 99.8 %) was purchased from Sigma Aldrich. Silicon wafers were purchased from Siegert Wafer GmbH. For the experiments shown in **Figures 4.25a** and **4.28a**, PS (M_w = 24.7 kg/mol; M_n = 24 kg/mol; PDI = 1.03) was purchased from Polymer Source Inc., Canada.

Self-ordered AAO was prepared by a two-step anodization procedure reported by Masuda and coworkers.[25] Aluminum chips (diameter 40 mm, thickness 1 mm; purity > 99.99 %) were annealed for 3h at 500°C under argon and electropolished at room temperature with a mixture of 25 vol-% 60 wt-% $HClO_4$ and 75 vol-% ultrapure C_2H_5OH pre-cooled to 6°C under moderate stirring (400 rpm) for 8 min at 4 A and 20 V. The anodizations were carried out at -1 °C in 1 wt-% phosphoric acid solution at 195 V. After the first anodization for 30 h, the formed alumina layer was etched with an aqueous mixture containing 1.8 wt-% CrO_3 and 7.1 wt-% of an 85 wt-% H_3PO_4 solution at 30 °C. The second anodization was carried out for about 40 h until the formed AAO layer had a thickness of 100 µm. The AAO pores were widened by isotropic etching with 10 wt-% phosphoric acid solution at 30 °C for 2h. As a result, AAO layers with a lattice constant of 500 nm, a pore diameter of 400 nm and a pore depth of 100 µm, which were attached to underlying aluminum substrates with a thickness of 900 µm, were obtained. All the AAO samples were prepared by C. Schulz-Kölbel and C. Heß at University of Osnabrück.

CPG membranes[27] with a thickness of 490 µm ± 10 µm extending 5 mm x 5 mm were produced by selective leaching applying a combined acid/alkaline treatment (1 M HCl, 90 °C, 2 h and 0.5 M NaOH, RT, 2 h) of phase-separated alkali borosilicate glass plates (composition: 62.5 wt.% SiO_2, 30.5 wt.% B_2O_3 and 7 wt.-% Na_2O; heat treatment 700 °C for 24 h), which results in the formation of spongy-continuous pore systems. The CPG membranes were characterized by mercury intrusion[98] (**Figure 4.29**) in a pressure range from 1 to 1000 bar with a PASCAl 440 porosimeter (ThermoScientific/POROTEC). Prior to any measurement, the samples were degassed at 0.2 mbar and 23 °C. All the CPG membranes were prepared and characterized by T. Paul at the University of Leipzig.

3.2 Imbibition method for AAO and CPG

Approximately 100 µm thick (as determined by SEM) PS films were prepared by solution casting. 40 µL and 10 µL for AAO and CPG, respectively, of a 10-wt% solution of PS in toluene were dropped on Si wafers previously cleaned three times by successive ultrasonication in acetone, ethanol, and methanol. The films were dried overnight under ambient conditions and then at 80 °C for 18 h under a vacuum. Before infiltration, the PS films were removed from the Si wafers by gently pressing the circumference of the films with a scalpel. The AAO membranes attached to underlying aluminum substrates and the free-standing CPG membranes were heated to 200 °C ± 2 °C in an argon atmosphere ≈ 0.5 Bar, as measured with a manometer, for 10 min in a cylindrical oven with a diameter of 41 mm and a height of 45 mm controlled by an Eurotherm 2416 controller. Then, the unsupported PS films were placed on the membranes surface for the desired infiltration time at the imbibition temperature t_i = 200 °C ± 2 °C in an argon atmosphere. To quench the infiltration, the samples were immersed in ice-cooled bi-distilled water. The samples were then dried overnight at 40 °C in an oven under ambient conditions. The imbibition procedure is schematically represented in **Figure 3.1**.

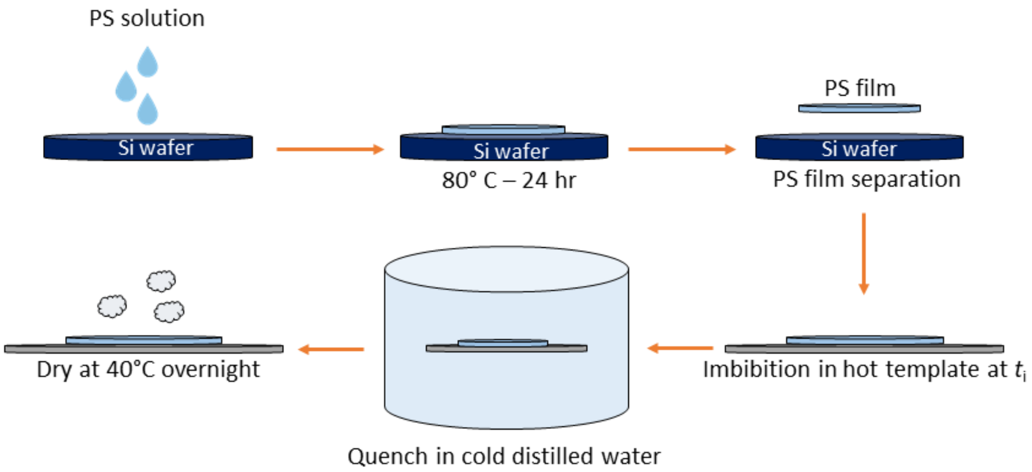

Figure 3.1. Schematic representation of the imbibition procedure for AAO and CPG samples.

3.3 Scanning Electron Microscopy of Imbibed AAO and CPG

Before imaging, the aluminum substrates of the PS-infiltrated AAO membranes were selectively etched with a solution containing 3.4 g $CuCl_2 \bullet 2H_2O$ and 100 mL HCl per 100 mL H_2O at 0°C. The freestanding PS-infiltrated AAO and CPG membranes were then cleaved perpendicularly to the membrane surface. The samples were sputter-coated with a platinum-iridium layer three times at 20 mA for 15 seconds in a K575X Emitech sputter coater. Scanning electron microscopy (SEM) images were obtained using a Zeiss *Auriga* microscope applying an acceleration voltage of 3 kV for AAO samples and 3.5 kV for CPG samples. A secondary electron secondary ion (SESI) detector located at an elevation angle ψ above an horizontal plane perpendicular to the e-beam as well as an in-lens detector located above the objective lens in a plane parallel to the sample surface[123] were used for image acquisition ensuring that the polymer bulk film, the infiltrated pore segments and the empty pores were visible in the images. Analysis of the images was performed with the software ImageJ.[124]

3.4 Energy Dispersive X-ray 2D Elemental Mapping of Imbibed AAO and CPG

Window integral EDX maps of the carbon Kα peak at 0.277 keV were obtained at a working distance of 5 mm using an EDX system Aztec (Oxford) equipped with an 80 mm^2-SDD-detector attached to the Zeiss *Auriga* SEM. Accelerating voltages of 3.0 kV and 3.5 kV were applied for the mappings of cross-sectional AAO and CPG samples. The 2D EDX maps extending 2048 pixels by 1532 pixels were imaged until at least 1 million counts were collected. The original EDX maps had an image depth of 32 bit. Roughness profiles $R_{q,EDX}(D)$ of the pixel intensities along horizontal pixel rows in x direction of an external reference coordinate system parallel to the membrane surfaces, where D is the distance to the membrane surface along the z direction of the reference coordinate system, were then extracted with the software Gwyddion.[125] The software Gwyddion reads the EDX maps with an image depth of 8 bit corresponding to 256 shades of red from 0 to 255. For the visualization of the EDX maps, a pixel binning factor of 2 was applied to combine 4 adjacent pixels forming 2 x 2 square matrices into one new pixel using the Aztec software.

3.5 X-ray Computed Tomography of Imbibed AAO and CPG.

3.5.1 *Sample preparation*

Samples for X-ray computed tomography were prepared by laser-micromachining in a microPREP^{TM} (3D-Micromac) device. Sub-millimeter cuts of the samples yielded the designed conical shapes with an average tip diameter of 50 μm atop a cube-shaped base as shown in **Figure 3.2**. Each sample was glued on top of a metallic pin with a laser-cut fitting for this base, which was then placed in the sample holder. All the samples were prepared and imaged by Dr. Martins de Souza e Silva and Dr. Santos de Oliveira at Martin-Luther-Universität Halle-Wittenberg.

3.5.2 Imaging of imbibed porous materials

To detect the PS imbibition front, Zernike phase-contrast X-ray computed tomography imaging was performed using a Carl Zeiss Xradia Ultra 810 device operating at 5.4 keV with a Cr X-ray source. Samples were imaged with a field-of-view of 64 × 64 μm^2 without camera binning. A total of 901 projections were collected over 180° with an exposure time of 70 s for AAO and 60 s for CPG. Image reconstruction was performed by a filtered back-projection algorithm using the software XMReconstructor integrated into the device, and tomograms obtained were exported as a stack of 16-bit TIFF images of approximately 1024 × 1024 pixels with an isometric pixel size of 64 nm. OriginPro 2020 and MATLAB R2021a were used for data analysis. All samples were imaged by Juliana Martins de Souza e Silva and Dr. Santos de Oliveira at Martin-Luther-Universität Halle-Wittenberg.

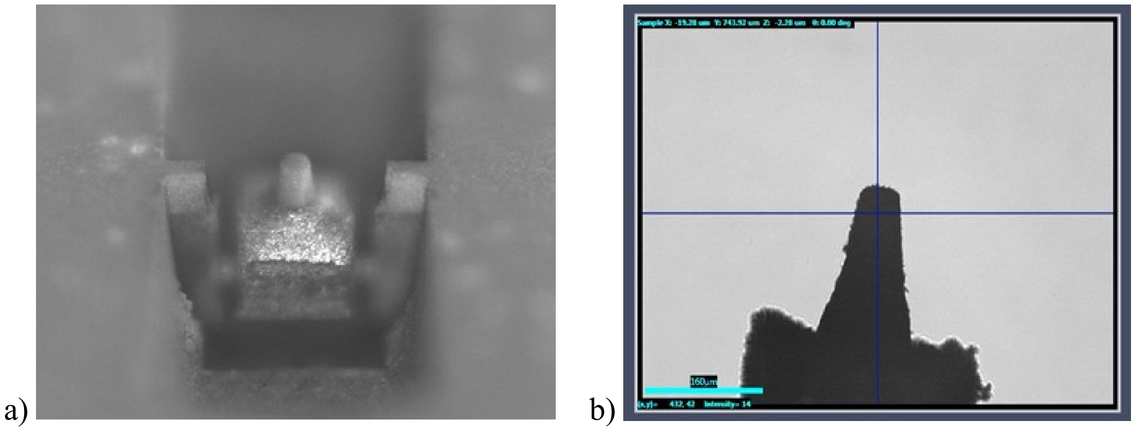

Figure 3.2. a) Photograph and b) optical microscopy image taken with an optical microscope inside the X-ray microscope used for X-ray computed tomography of a sample specimen prepared by laser cutting. The length of the light blue scale bar in b) corresponds to 160 µm.

4 Results

The spatiotemporal evolution of imbibition fronts during the invasion of Polystyrene (PS) at 200 °C into AAO and CPG for different infiltration times was investigated with X-ray CT and the results compared with SEM and 2D EDX results. To determine the average positions of the imbibition fronts and imbibition front widths parameters allowing their quantitative description need to be identified. Thus, algorithmic image analysis procedures based on descriptive statistics of pixel intensity dispersion were developed.

4.1 Determination of Statistical Descriptors for Morphological Features

At first, an adequate statistical descriptor must be chosen that is able to quantify reliably the average positions of the imbibition fronts and the imbibition front widths of the samples. To establish a universally usable descriptor, the X-ray CT data sets were employed as descriptor-choice limiting factor due to larger sample volumes probed compared to SEM and 2D EDX as well as prevention of preparation artifacts that may occur when infiltrated membranes are cleaved to prepare cross-sectional specimens for the SEM or EDX mappings.

4.1.1 Analysis of morphological features from X-ray computed tomography data

To choose a suitable descriptor, first the morphological features of interest must be identified and described. Raw data sets from X-ray CT of an AAO and CPG samples infiltrated for 3 min consisted of at least 1000 16-bit *xy* slices encompassing 65536 shades of gray with a voxel size of 64 nm^3, which were approximately parallel to the membrane surfaces and the *xy* plane of the reference coordinate system (**Figure 4.1a,c**) for each of the samples. The ensemble of all X-ray CT *xy* slices correspond to a volumetric reconstruction of the 3-minute imbibed AAO and CPG samples. The raw *xy* slices were approximately parallel to the membrane surfaces (in the case of AAO normal to the pore axes). To obtain cross-sections of the samples perpendicular to the membrane surfaces, the ensemble of slices needs to be re-sliced and aligned with ImageJ. This procedure yields *xz* slices oriented normal to the membrane surfaces (in the case of AAO parallel to the AAO pore axes). The final result are 3D reconstructions of *xz* slices where the PS-surface film (bottom), the PS-infiltrated pore segments (middle) and the empty pore segments (top) are visible (**Figure 4.1b,d**). The edges of the sample considered as artifacts are shown in green squares and were not considered during image analysis.

AAO and CPG membranes have different pore systems, while AAO contains parallel straight cylindrical pores (**Figure 4.1a,b**), in CPG pore walls and pores form two interpenetrating networks, resembling a sponge, (**Figure 4.1c,d**) making CPG a more challenging porous material to analyze. In AAO 3D reconstructions the pores and pore walls and imbibition front are easier to differentiate with the naked eye due to the parallel alignment of the pores, normal to the membrane surface. For these reasons, AAO data sets were chosen to describe the pixel intensity differences between the pores, pore walls, empty space and imbibition front

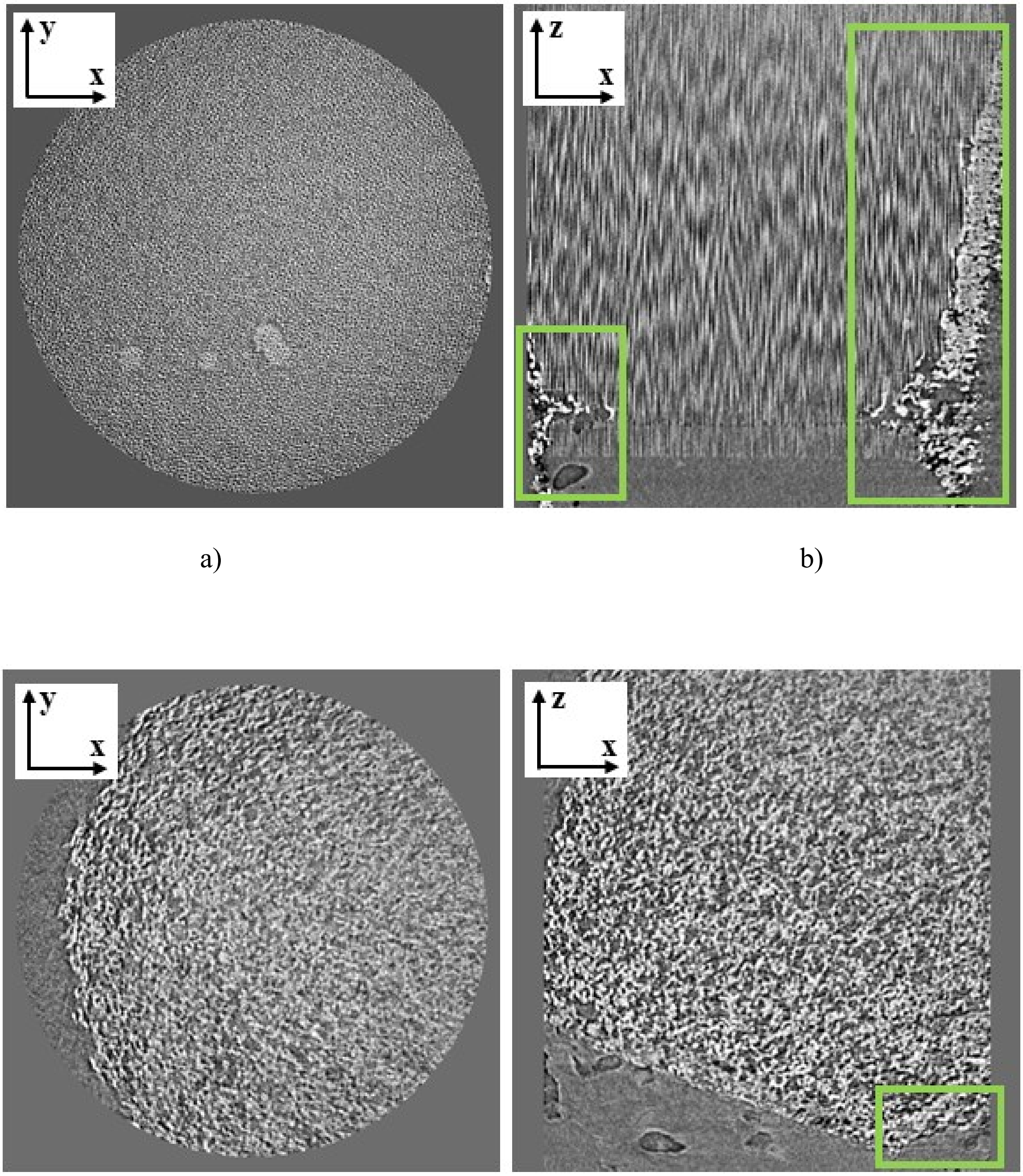

a) b)

c) d)

Figure 4.1. Raw slices of 3D reconstructions obtained by X-ray computed tomography of AAO and CPG membranes infiltrated for 3 min at 200°C with PS. Each pixel has edge lengths of 64 nm and corresponds to one data point. Empty membrane pores appear dark, pore walls bright. a) Raw *xy* slice of AAO with a width of 1012 pixels and a height of 1024 pixels. b) Raw *xz* slice of AAO with a width of 1012 pixels and a height of 1019 pixels showing the imbibition front. Empty pore segments are at the top, a continuous PS surface film attached to the AAO surface is located on the bottom, and PS-filled AAO pore segments are seen in between. c) Raw *xy* slice of CPG with a width of 1016 pixels and a height of 1024 pixels. d) Raw *xz* slice of CPG with a width of 1016 pixels and a height of 1000 pixels showing the imbibition front prior to the adjustment of the membrane surface to the reference coordinate system. Empty pore segments are located at the top, a continuous PS surface film attached to the AAO surface is located on the bottom, and PS-filled CPG pore segments are seen in between. Defects are marked by green boxes.

Details of sections through the three-dimensional volumetric reconstruction of AAO infiltrated with PS for 3 minutes obtained by phase-contrast X-ray computed tomography are shown in **Figure 4.2**. These details are reproduced with single-pixel resolution. Each pixel represents a data point in the volumetric reconstruction. The edge lengths of the pixels correspond to 64 nm. **Figure 4.2a** displays a detail of a *xy* slice, that is, a section normal to the AAO pore axes, which intersects empty AAO pore segments close to the imbibition front. The detail of the section along the AAO pore axes displayed in **Figure 4.2b** shows the imbibition front. The orientation of the section is the same as that of the *xz* slice displayed in **Figure 4.1b**. Furthermore, the section shows a similar sample region. Remarkable features are the dark dot-like areas approximately in the center, which mark the imbibition front within the AAO pores. **Figure 4.2b** demonstrates the advantages of the phase-contrast mode, in which phase boundaries, such as the boundary between PS and air at the imbibition front in the AAO pores, are highlighted. In both sections shown in **Figure 4.2**. the AAO pores are clearly discernible. It should be noted that the surfaces of the AAO pore walls may intersect pixels, which thus contain brightness contributions from the AAO pore walls and from the AAO pore volume.

In general, a pixel can cover two or more objects, the boundary of which intersects the pixel. Therefore, considering two times the pixel edge length, i.e., the minimum distance between a pixel center and the center of its second-nearest neighbor, is suggested as the resolution limit (here 128 nm). This resolution limit is, however, still sufficient to resolve single AAO pores.

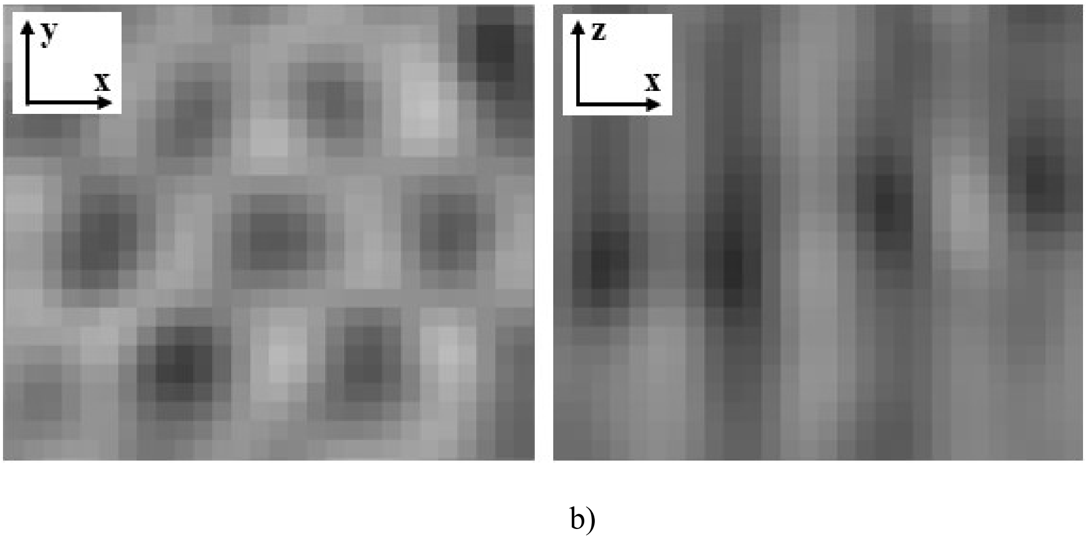

Figure 4.2. Sections with a width of 28 pixels and a height of 24 pixels through the volumetric reconstruction of AAO infiltrated for 3 min at 200°C with PS. Each pixel has edge lengths of 64 nm and corresponds to one data point. a) Slice normal to the AAO pore axes (*xy* slice) intersecting empty AAO pore segments close to the imbibition front. The empty AAO pores appear dark, the AAO pore walls bright. b) Section along the AAO pore axes showing the imbibition front. Empty pore segments are at the top, PS-filled AAO pore segments on the bottom.

As obvious from a pixel intensity line profile along a part of a pixel row of **Figure 4.2a** shown in **Figure 4.3**, about 3 linearly arranged contiguous pixels with low pixel intensities represent the pores, which are separated by pore walls indicated by 1-2 pixels with high pixel intensities. In between, 1-2 pixels with intermediate pixel intensities with contributions from both the AAO pores and the AAO pore walls can be seen. The selected resolution allows the coverage of both the imbibition front and the AAO surface, as required to determine the imbibition lengths, and enables the evaluation of a large, four-digit number of AAO pores to ensure statistical reliability.

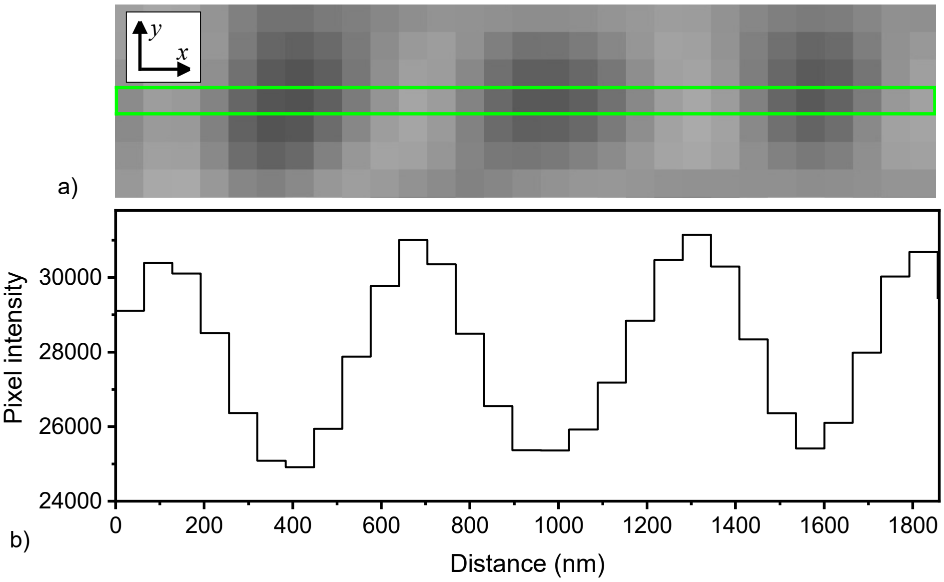

Figure 4.3. Pixel intensity line profile taken from a *xy* slice of a volumetric reconstruction of X-ray computed tomography data of AAO infiltrated for 3 min at 200°C with PS. The *xy* slice intersects empty AAO pore segments close to the imbibition front. Each pixel has edge lengths of 64 nm and corresponds to one data point. a) Detail of the *xy* slice with single-pixel resolution. b) Pixel intensity line profile along the center pixel row in panel a) (marked by green square). Note that the orientation of the pixel row, i.e., the orientation of the pixel intensity line profile, does not necessarily coincide with the direction of the shortest connection between two AAO pore centers corresponding to the nearest-neighbor distance.

4.1.2 Root mean square roughness as statistical descriptor

Each of the three imaging techniques described in Chapter 3 (cf. Sections 3.3, 3.4 and 3.5) consists of 2D visualizations or 3D reconstructions of the PS-imbibed membranes. The 2D images as well as slices of 3D reconstructions may show cross-sectional views approximately normal to the membrane surfaces. The images were obtained or processed in such a way that the bulk PS surface films are at the bottom, the PS-filled pore segments in the middle and the empty parts of the membranes are at the top (**Figure 1.1**). The three mentioned areas are differentiable with the naked eye and contain distinctive pixel brightness value distributions that can thus be quantified statistically.

The arithmetic mean (I_{mean}) and root mean square roughness (R_q) of the pixel intensities along rows of pixels parallel to the membrane surfaces corresponding to the *x* direction of the reference coordinate system, were tested to quantify the morphological features of interest, the PS surface film, the membrane surface and the imbibition front position and width, however, both the X-ray CT datasets, in particular CPG data sets, were particularly challenging regarding data extraction from the imbibition front positions and widths, as compared to SEM and EDX, due to the minute contrast differences between the PS, CPG pore walls and empty space as well as the spongy pore structure of CPG. Therefore, the CPG and AAO X-ray CT data sets (**Figure 4.4**) were used as statistical descriptor choice limiting factor.

The pixel brightness dispersion along rows of pixels parallel to the membrane surfaces, "second moment" of the pixel brightness frequency density, denoted $R_{\mathrm{q,s}}$ or $R_{\mathrm{q,EDX}}$ was chosen as statistical descriptor rather than the arithmetic mean value I_{mean} of the pixel intensities along rows of pixels parallel to the membrane surfaces, "first moment" of the pixel brightness frequency density. To illustrate why, the arithmetic mean I_{mean} (D) (Equation 4.1) profiles that represents the arithmetic mean value of pixel intensities along a pixel row in x-direction as a function of D and the $R_{q,s}$ (D) (Equation 4.2) profiles that represent the average pixel brightness dispersion along a pixel row in x-direction as a function of D of single slices of the X-ray CT data sets of AAO with t_i = 30 min (**Figure 4.4c,d**) and CPG with t_i = 90 min (**Figure 4.4a,b**) were calculated with the software Gwyddion.[125] The original 16-bit xy slices encompassing 65536 shades of gray were resliced so as to obtain xz slices and tilt-corrected using an ImageJ reference grid. As a result, in the processed xz slices the membrane surface was horizontally oriented. The I_{mean} (D) and $R_{q,s}$ (D) were calculated with the following equations:

$$I_{mean} = \frac{1}{N}\sum_{j=1}^{N} I_j \qquad \text{(Equation 4.1)}$$

$$R_{q,s} = \sqrt{\frac{1}{N}\sum_{j=1}^{N}\left(I_j - I_{mean}\right)^2} \qquad \text{(Equation 4.2)}$$

N is the number of pixels per row, I_j is the brightness value of pixel j, j the index of summation ($1 \leq j \leq n$) and I_{mean} the mean brightness value of all pixels in the considered row. Thus, for each pixel row at a certain distance D to the surfaces of the AAO and CPG membranes an $R_{q,s}$ (D) value was obtained.

In **Figure 4.4**, it can be seen that the $R_{q,s}$ descriptor delivers very prominent features at the surface of the membranes as well as at the approximate position of the imbibition front in the form of peaks or steps as compared to I_{mean}. The I_{mean} (D) and the R_q (D) profiles of CPG membranes infiltrated with PS for different infiltration times t_i = 3, 20, 30 and 90 minutes are shown in **Figure 4.5**. The green area represents the empty pore segments, the orange area the PS filled pore segments and the blue area the bulk PS surface films. The color-coded areas were chosen qualitatively from features representing the CPG membrane surface and the position of the imbibition front from the R_q (D) profiles and replicated in the I_{mean} (D) profiles for comparison.

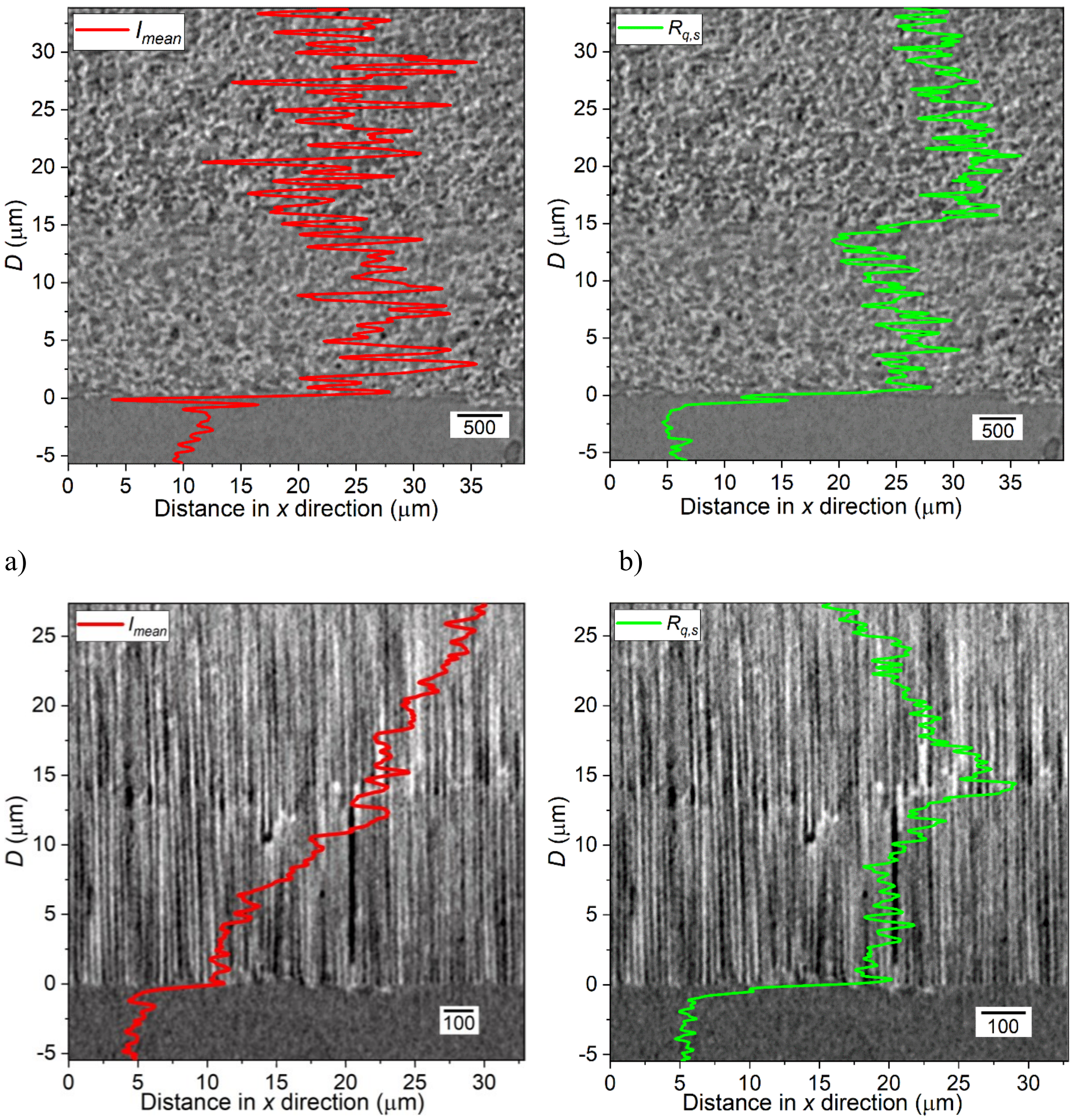

a)

b)

c)

d)

Figure 4.4. The I_{mean} (D) (red lines) and $R_{q,s}$ (D) profiles (green lines) superimposed on 16-bit xz slices encompassing 65536 shades of gray through the volumetric reconstruction of the sample volumes obtained from X-ray computed tomography data from CPG and AAO membranes infiltrated with PS at 200°C. The distance D to the membrane surfaces is plotted along the vertical axis (corresponding to the z direction reference coordinate system). The horizontal axis represents the x direction of the reference coordinate system in the probed sample volume. a) I_{mean} (D) profile of CPG infiltrated for 90 minutes. b) $R_{q,s}$ (D) profile of CPG infiltrated for 90 minutes. c) I_{mean} (D) profile of AAO infiltrated for 30 minutes. d) $R_{q,s}$ (D) profile of AAO infiltrated for 30 minutes.

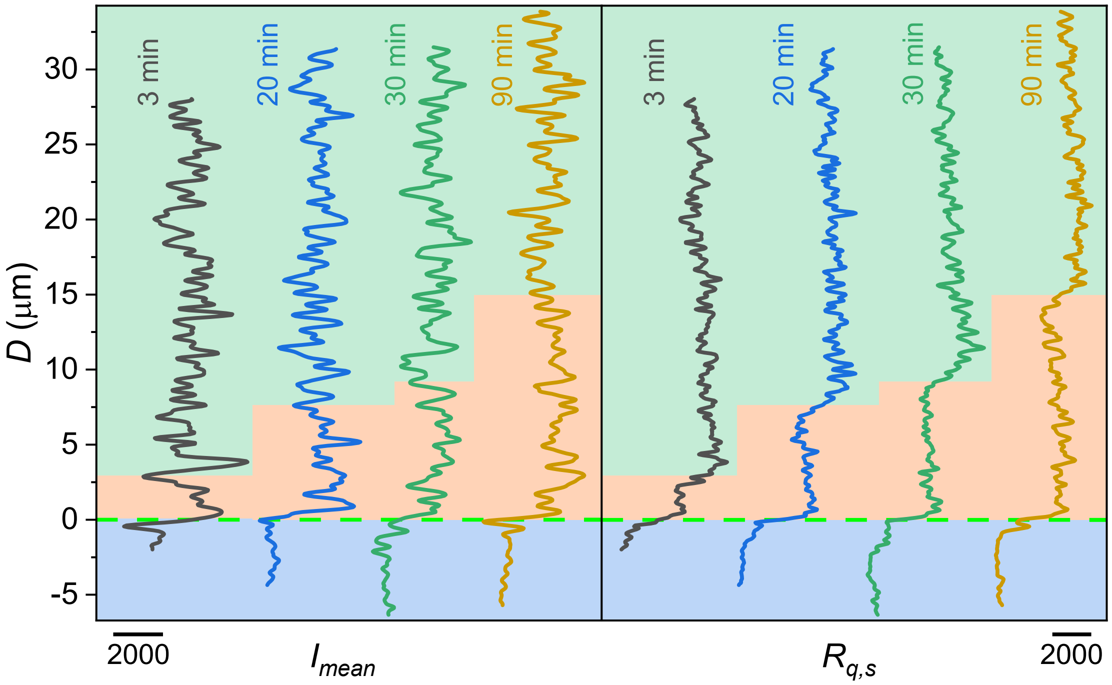

Figure 4.5. Evaluation of a cross-section of CPG infiltrated with PS for t_i = 3, 20, 30 and 90 minutes using mean pixel intensities I_{mean} of pixel rows parallel to the CPG membrane surface as descriptor. I_{mean} is plotted as a function of the distance D to the CPG membrane surface. For comparison, the corresponding R_q (D) profiles are also displayed. The distance D to the membrane surface is plotted along the vertical axes corresponding to the z-axis of the external reference coordinate system. Empty parts of the membranes are seen at the top (green area), membrane parts with PS-filled pore segments in the middle (orange area), and the bulk PS surface films on the membrane surfaces on the bottom (blue area).

For the 8-bit 2D EDX maps of the intensity of the carbon Kα peak indicating the distribution of PS, which predominantly consists of carbon, infiltrated at 200° C for 3 minutes AAO and CPG samples (**Figure 4.6**), the I_{mean} and $R_{q,EDX}$ descriptors provided very similar results but $R_{q,EDX}$ delivered more prominent steps at the interface between PS-infiltrated and empty membrane, thus $R_{q,EDX}$ was chosen for consistency with results from X-ray CT data sets. The 2D EDX maps were adjusted in such a way that the surfaces of the AAO and CPG membranes were parallel to the x axis of an external reference coordinate system, whereas the distance D to the membrane surface was measured along the z axis oriented perpendicularly to the membrane surfaces (and parallel to the AAO pores). The intensities of the carbon Kα peaks were encoded by 256 shades in a color space ranging from black (relative peak intensity zero) to red (relative peak intensity 1). The average root mean square roughness $R_{q,EDX}$ of the pixel intensities along rows of pixels in the x direction parallel to the surfaces of the AAO and CPG membranes was calculated using the software Gwyddion[125] according to:

$$R_{q,EDX} = \sqrt{\frac{1}{N}\sum_{j=1}^{N}\left(I_j - I_{mean}\right)^2} \qquad \text{(Equation 4.3)}$$

N is the width of the evaluated 2D EDX maps in pixels, i.e., the number of pixels per row in the x direction parallel to the surfaces of the AAO and CPG membranes. The pixel intensity is denoted I_j, where j is the index of summation ($1 \leq j \leq N$), and I_{mean} denotes the mean pixel intensity of all pixels in the considered row. Thus, for each pixel row at a certain distance D to the surfaces of the AAO and CPG membranes an $R_{q,EDX}$ (D) value was obtained.

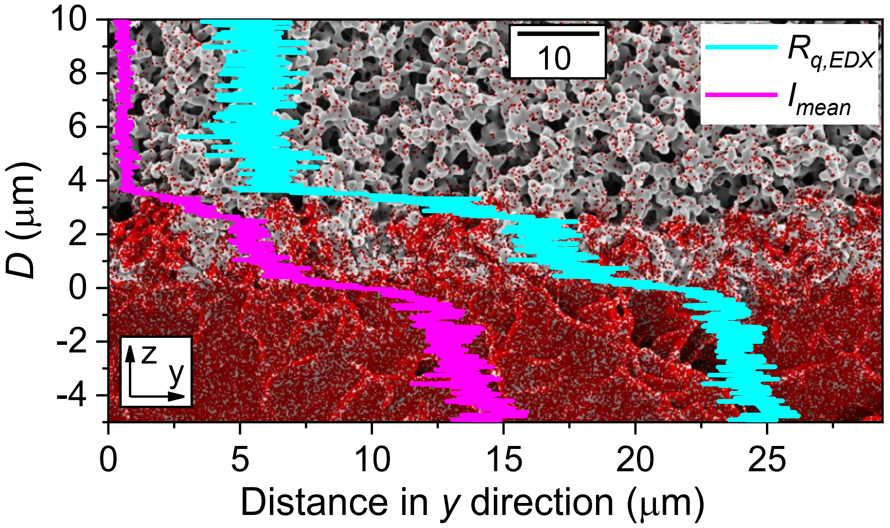

Figure 4.6. Evaluation of 2D EDX maps of a cross-section of CPG infiltrated with PS for infiltrated with PS for t_i = 3 minutes using mean pixel intensities I_{mean} of rows of pixels, on an 8-bit scale encompassing 256 shades of red, parallel to the CPG membrane surface as descriptor. The carbon Kα peak intensity 0.277 keV was mapped. I_{mean} is plotted as a function of the distance D to the CPG membrane surface (pink curve). For comparison, the corresponding R_q (D) profile of the pixel intensities on an 8-bit scale encompassing 256 shades of red is also displayed (light blue curve). The I_{mean} (D) and R_q (D) profiles are superimposed on the corresponding EDX map, which is in turn superimposed on the SEM image of the mapped area. The distance D to the membrane surface is plotted along the vertical axes corresponding to the z-axis of the external reference coordinate system. Empty parts of the membranes are seen at the top, membrane parts with PS-filled pore segments in the middle, and the bulk PS surface films on the membrane surfaces on the bottom.

4.2 Analysis of X-ray CT Data of Imbibed AAO Based on Pore Center Identification

4.2.1 Description of volumetric reconstruction analysis algorithm

The extraction of the relevant features from the volumetric reconstructions obtained by phase-contrast X-ray computed tomography, which include the position of the imbibition front relative to the surface of the AAO membrane (the average imbibition length L_a) and the width of the imbibition front, could not be achieved by segmentation procedures. **Figure 4.7a** shows a three-dimensional region of interest cropped from a volumetric reconstruction of the morphology of AAO, which was infiltrated with PS for 3 minutes at 200 °C. The PS surface film is located on the very bottom, the PS-filled AAO pore segments are seen in the lower part on top of the PS surface film and the part of the AAO membrane, in which the AAO pores are empty, on top. The contrast differences between empty and PS-filled pore segments as well as between PS-filled pore segments and AAO pore walls are minute. Moreover, brightness fluctuations occur not only between but also within the AAO pore walls as well as the PS-filled and the empty AAO pore segments. Hence, a semi-automated algorithmic procedure was devised to extract single-pore imbibition lengths L_s from the morphology reconstructions obtained by phase-contrast X-ray computed tomography, which can be divided into three stages.

Stage 1 comprises data import and preprocessing. After volumetric reconstruction, a suitable sub-volume containing an array of intact AAO pores was manually cropped for further evaluation (**Figure 4.7a**). The cropped volume was then rotated to align the AAO pore axes with the *z*-axis of a Cartesian coordinate system employed as external reference framework using a standard implementation that employs bicubic interpolation for high-quality results.[126] As a result, stacks of *xy* slices oriented normal to the AAO pore axes were obtained. Then, the brightness values of the pixels constituting the *xy* slices in the selected sub-volume were normalized to one.

Stage 2 comprises the identification of the center coordinates of the AAO pores, which need to be determined with high precision because they are used to extract brightness profiles along the identified AAO pores. Thus, a set of AAO pore center coordinates was generated as follows. Several (here 10 – 40) adjacent *xy* slices intersecting empty AAO pore segments close to but ahead of the imbibition front were condensed into one “stage 2” *xy* slice. By this procedure, the signal-to-noise ratio and the contrast between pore walls and pores was improved. The condensed “stage 2” *xy* slice was binarized applying a relative luminance of 30 % as threshold value. The coordinates of the black foreground pixels in the binarized averaged *xy* slice represent a single 2D point cloud with multiple clusters representing the AAO pores. Cluster centers were identified by nonparametric clustering applying a custom-made variation of mean-shift clustering[127], which enables fast computation with limited need of memory.

First, the brightness values of the binarized averaged *xy* slices were initialized as an input matrix by ascribing a frequency value of 1 to black foreground pixels belonging to the AAO pores and a frequency value of 0 to bright background pixels belonging to the AAO pore walls. Clustering was achieved iteratively. A local neighborhood of size 11 x 11 pixels^2 was defined around each non-zero pixel and computed the respective center of mass. In the first iteration, these non-zero pixels were the black pixels of the input image. The *y*-coordinate of the center of mass was the arithmetic mean of the *y*-coordinates of the non-zero pixels inside the neighborhood weighted by their frequency value. As initially a value of 1 was assigned to the black pixels, in the first iteration all weights were 1. The *x*-coordinate of the center of mass was computed in the same way. The initially considered black pixel in the center of its neighborhood was then shifted to the neighborhood's center of mass. This operation increased the frequency value ascribed to the location of the center of mass by the frequency value of the displaced center pixel – in the first iteration by 1. This increase was done in a new matrix, which was initialized with a frequency value of zero for all pixels. Conducting this operation for all black pixels yielded a new output matrix, in which integer frequency values were assigned to all pixel positions in the binarized averaged *xy* slice. The output matrix of the first iteration was then used as input matrix for the second iteration, in which the same steps as in the first operation were repeated. Further iterations were carried out until the output matrices of successive iterations converged. As a result, the black pixels representing specific AAO pores collapsed into a single *xy* pixel position. The computational effort linearly scaled with the number of black foreground pixels in the binarized and averaged *xy* slice, because black foreground pixels belonging to specific AAO pores constituted small clusters with similar size and shape so that the convergence of the pixel clusters representing specific AAO pores required approximately the same time. As clusters may merge during an iteration, fewer pixels needed to be processed in subsequent iterations. In this way, the center coordinates of several thousand AAO pores were computed within seconds.

Figure 4.7b and **Figure 4.8a** show the positions of the AAO pores identified in a representative square area with an edge length of 19.134 µm. **Figure 4.8b** shows the Fourier spectrum obtained with **Figure 4.8a** as input image as well as the corresponding radial intensity profile rescaled into the real space. The radial intensity profile in **Figure 4.8b** shows a characteristic peak (at position indicated with a "2") representing the nearest-neighbor distance of the AAO pores. However, the obtained set of center coordinates does not contain all AAO pores present in the probed sample volume. Using the program ImageJ, 1504 identified AAO pores were counted, whereas the number of AAO pore expected for a perfect hexagonal lattice with a lattice constant of 500 nm would amount to 1691.

Stage 3 comprises the identification of the single-pore imbibition lengths. In each *xy* slice obtained in stage 1 the mean brightness values of 5 x 5 contiguous pixels surrounding the AAO pore centers identified in stage 2, which cover an area extending 320 x 320 nm^2, were calculated. The brightness values obtained for a specific AAO pore center from all *xy* slices were then arranged in a one-dimensional brightness tuple along the AAO pore axis (parallel to the *z* axis of the reference coordinate system). After linear detrending and normalization of the pixel brightness values, each tuple represents the brightness profile along the considered AAO pore. The brightness tuples obtained in this way were assembled into a brightness tuple image (**Figure 4.7c**), in which each vertical pixel column is a brightness tuple representing the brightness profile along one AAO pore (**Figure 4.7d**). Note that the sequence of the brightness tuples has no physical meaning.

The brightness tuple images differ from the volumetric reconstructions of the sample morphology directly accessible by phase-contrast X-ray computed tomography in that the contribution of the AAO pore walls is removed from the region of interest around the imbibition front. The removal of the contribution of the AAO pore walls is crucial for the identification of the imbibition front by phase contrast imaging because phase contrast only emerges at the menisci separating PS-filled and empty pore segments. Thus, the boundary between PS-filled and empty AAO pore segments is, as compared to the original volumetric reconstruction (**Figure 4.2a** and **Figure 4.7a**), much more pronounced in the brightness tuple image seen in **Figure 4.7c**. The imbibition front appears in the brightness tuple images as a pronounced dark band oriented perpendicular to the brightness tuples and the AAO pore axes. The approximate position of the imbibition front was determined by visual inspection.

Then, segments of the brightness tuples centering about the dark band were selected. The selected segments of the individual brightness tuples were linearly detrended. The z position of the darkest pixel within the detrended segments was determined as position of the imbibition front in the AAO pore represented by the considered brightness tuple.

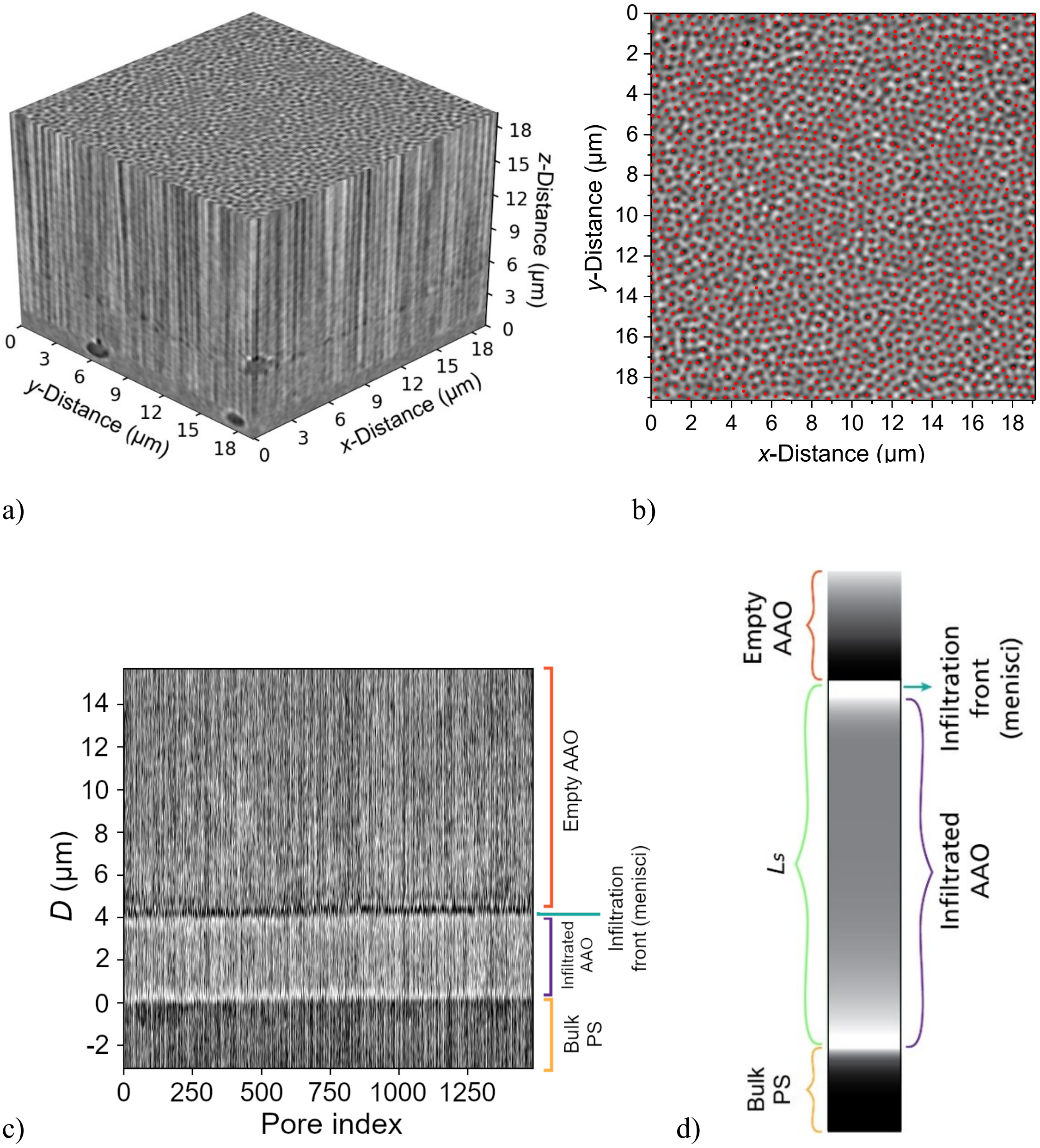

Figure 4.7. Phase-contrast X-ray computed tomography of an AAO membrane infiltrated with PS for 3 minutes. a) Cropped reconstructed volume of interest; b) View of a *xy* slice of the reconstructed volume of interest oriented perpendicularly to the AAO pore axes. The centers of the identified AAO pores are marked by red dots. c) Brightness tuple image, in which vertical pixel columns correspond to brightness tuples representing the brightness profiles along the identified AAO pores at the positions of the red dots in panel b). The distance to the AAO surface *D* is plotted along the vertical axis, which is oriented parallel to the AAO pore axes. The horizontal axis represents an arbitrary index number ascribed to each considered AAO pore without physical meaning. d) Schematic representation of the brightness profile along a single AAO pore.

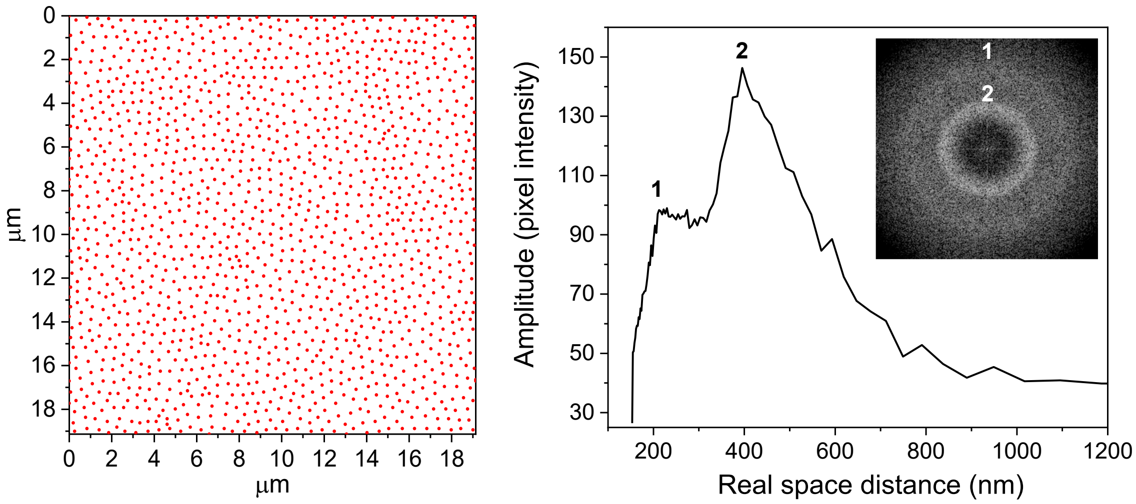

a) b)

Figure 4.8. AAO pore centers identified in X-ray computed tomography data by a custom-made iterative variation of mean-shift clustering. a) AAO pore centers marked by red dots, which were identified in the *xy* slice oriented normal to the AAO pore axes shown in **Figure 4.1a** b) Fourier spectrum of the dot pattern displayed in panel a) and radial intensity profile of the Fourier spectrum rescaled into the real space. A diffuse outer ring 1 corresponding to peak 1 represents the dot diameters. The more pronounced inner ring 2 corresponding to peak 2 represents the nearest-neighbor distance between adjacent AAO pores. The radial intensity profiles were obtained with the ImageJ plugin "Radial Profile Plot" (Author: Paul Baggethun, Pittsburgh, PA; https://imagej.nih.gov/ij/plugins/radial-profile.html; accessed on September 21, 2021). The intensities of all pixels forming a circle about the center point of the Fourier spectrum were added, and the sum was divided by the number of considered pixel. The obtained values were plotted against the spatial frequency and were rescaled into the real space by dividing the spatial frequency by the edge length of the original real space image yielding the evaluated Fourier spectrum.

4.2.2 Calculation of single pore imbibition lengths L_s

To calculate the single pore imbibition length L_s, the distance between the position of the imbibition front and the position of the AAO surface needs to be determined. In the brightness tuple images (**Figure 4.9**), the position of the AAO surface appeared as a bright band consisting of local brightness maxima in the brightness tuples. This outcome is, at first glance, unexpected because no interface separates the PS in the PS-filled AAO pore segments at the pore openings from the bulk PS film located on the AAO surface. However, the center coordinates of the AAO pores were determined from *xy* slices close to but ahead of the imbibition front. It was assumed, that the brightness tuples trend the more away from the AAO pore axes the larger the distance to the imbibition front is. Considering that every pixel of the brightness tuples represents an area extending 320 x 320 nm^2 normal to the brightness tuple, it is straightforward to assume that the brightness tuples at the position of the AAO surface contain significant phase contrast contributions emerging from the interface between the AAO matrix and the bulk PS film located on the AAO surface. Thus, in the individual brightness tuples the position of the AAO surface is marked by local brightness maxima. The positions of these local brightness maxima were determined in the same way as the positions of the imbibition front. Therefore, trending of the brightness tuples away from the AAO pore axes is here rather an advantage than a drawback. As a result, for each brightness tuple, that is, for each AAO pore, L_s could be determined as the distance between the brightness minimum representing the imbibition front and the brightness maximum representing the AAO surface.

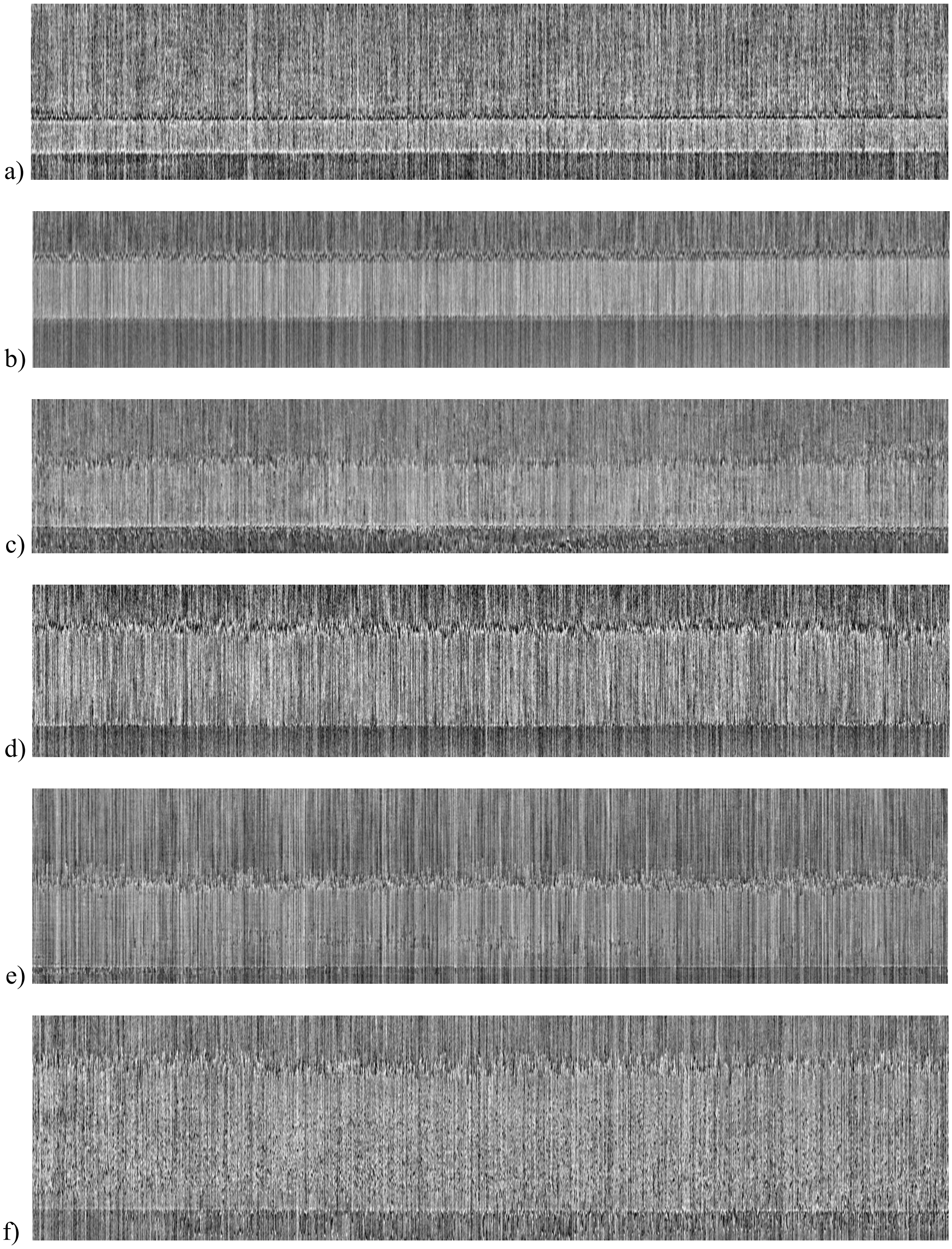

Figure 4.9. Brightness tuple images, in which vertical pixel columns correspond to brightness tuples representing the brightness profiles along the identified AAO pores infiltrated a) for 3 minutes, (1504 y-tuples x 327 pixels), b) for 10 minutes, (4796 y-tuples x 289 pixels), c) for 20 minutes, (2358 y-tuples x 380 pixels), d) for 30 minutes, (1304 y-tuples x 391 pixels), e) 70 minutes, (2631 y-tuples x 751 pixels) and f) for 90 minutes, (1407 y-tuples x 327 pixels) with PS at 200 °C. The PS surface film is at the bottom, the PS-filled segments is in the center and the empty pore segments at the top of the images. The original dimensions of all images were modified to fit the page.

4.2.3 *Average position of the imbibition front*

A straightforward approach to determine the average imbibition length L_a, hereafter referred to as *CT-mean*, is the calculation of the arithmetic mean value of the imbibition lengths L_s of the individual AAO pores extracted from the corresponding brightness tuples (**Figure 4.10**). A second approach to determine L_a, hereafter referred to as *CT-rms*, involves the evaluation of horizontal brightness fluctuations in the brightness tuple images normal to the brightness tuples and the AAO pore axes, that is, parallel to the AAO surface. For this purpose, rows of pixels with the same z value oriented normal to the brightness tuples and the AAO pore axes (**Figure 4.7c** and **Figure 4.9**) were evaluated. Each of these pixel rows contains exactly one pixel of each brightness tuple. Pixel rows behind the imbibition front at distances D from the AAO surface, where all AAO pores are filled with PS, consist of relatively bright pixels. Pixel rows ahead of the imbibition front at D values, where all AAO pores are empty, contain somewhat darker pixels. Because of the non-zero imbibition front width pixel rows at D values approximately corresponding to L_a contain bright pixels belonging to AAO pore segments filled with PS ($L_s > D$), somewhat darker pixels belonging to empty AAO pore segments ($L_s < D$) and very dark pixels indicating the boundary between empty and filled AAO pore segments ($L_s \approx D$). The situation at the AAO surface is similar. Pixel rows belonging to the bulk PS film on the AAO surface ($D < 0$ µm) consist of relatively dark pixels, while the interface between AAO and bulk PS surface film is indicated by very bright pixels. However, since the position of the brightness maximum slightly varies between the individual brightness tuples, pixel rows at the approximate position of the AAO surface ($D \approx 0$ µm) contain dark pixels belonging to the bulk PS surface film, brighter pixels belonging to filled AAO pore segments and very bright pixels representing the interface between the AAO and bulk PS surface film. Therefore, particularly pronounced scattering of the pixel brightness values along the pixel rows normal to the brightness tuples representing the brightness profiles along the AAO pores indicates the position of the relevant interfaces, i.e., the imbibition front and the AAO surface **Figure 4.10a**).

To identify the positions of the imbibition front and the AAO surface, the *y-tuple* root mean square roughness $R_{q,y}$ of the pixel brightness values along rows of pixels normal to the brightness tuples in 8-bit brightness tuple images were calculated using the software Gwyddion[125] according to:

$$R_{q,y} = \sqrt{\frac{1}{N}\sum_{j=1}^{N}\left(I_j - I_{mean}\right)^2} \qquad \text{(Equation 4.4)}$$

N is the number of pixels per row, I_j the gray value of pixel j, I_{mean} the mean gray value of all pixels in the considered row and j the index of summation ($1 \leq j \leq N$). If $R_{q,y}$ is plotted against the distance D from the AAO surface (**Figure 4.10b**), the average imbibition length L_a corresponds to the distance between the $R_{q,y}$ extrema indicating the positions of the imbibition front and the AAO surface (**Figure 4.10d**).

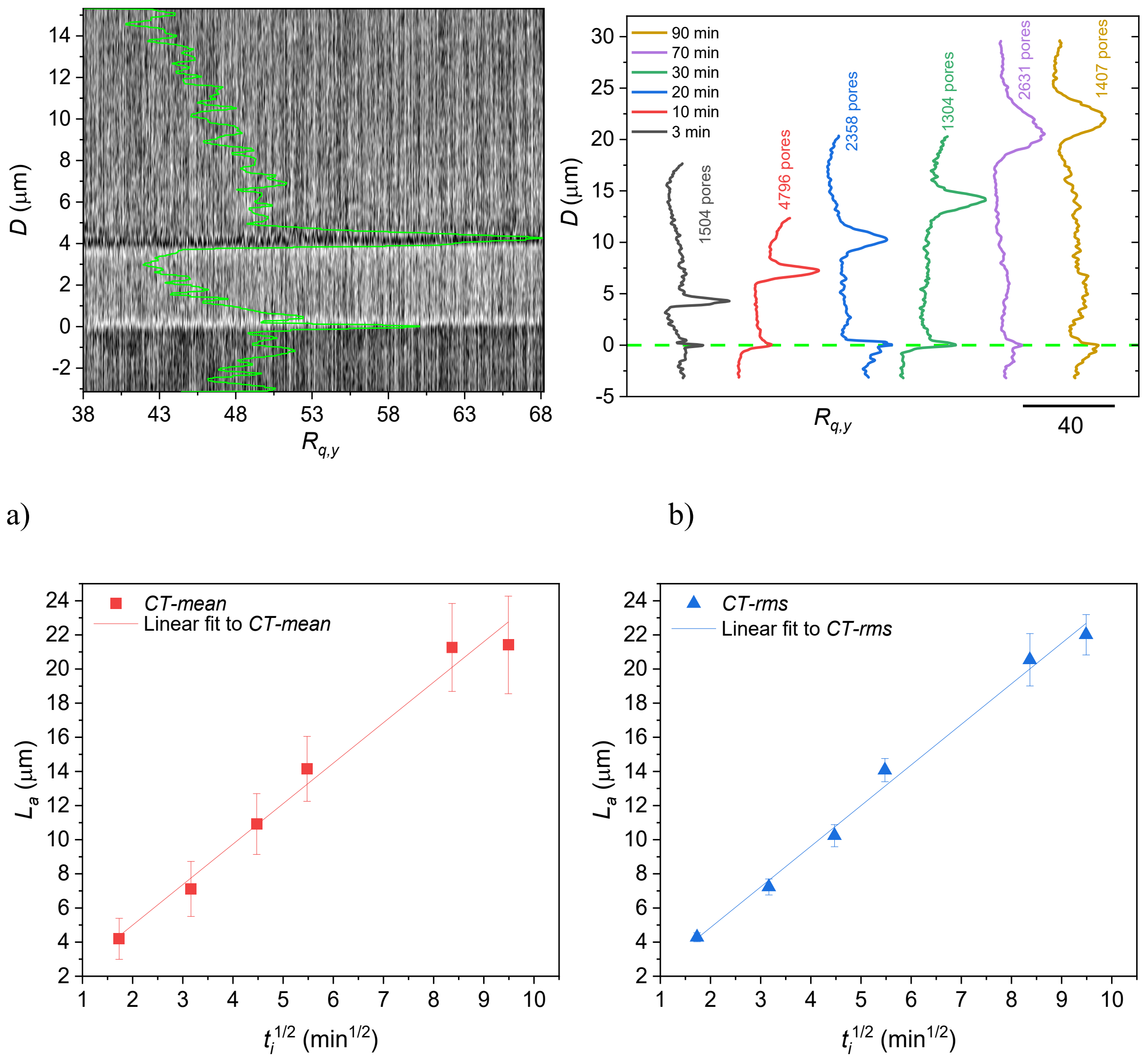

a)

b)

c)

d)

Figure 4.10. a) Brightness tuple image obtained from AAO infiltrated with PS for 3 minutes, on which the root mean square roughness $R_{q,y}$ of the brightness values in pixel rows oriented parallel to the horizontal axis plotted against the distance D from the AAO surface (green) is superimposed. b) $R_{q,y}$ plotted against D for different infiltration times t_i. The AAO surface is located at $D = 0$ µm and indicated by a dashed green line. The indicated $R_{q,y}$ interval corresponds to a range of 40 out of 256 shades. c) Average imbibition lengths $L_a(t_i)$ plotted against the square root $t_i^{1/2}$ of the imbibition time t_i obtained with method *CT-mean*. The error bars correspond to the standard deviation. d) Average imbibition lengths $L_a(t_i)$ plotted against the square root $t_i^{1/2}$ of the imbibition time t_i obtained with method *CT-rms*. The error bars correspond to the standard deviation obtained from the Gaussian fit to the imbibition front peak.

4.2.4 Quantification of the imbibition front width

The standard deviations σ of the frequency densities of the single-pore imbibition lengths L_s were calculated from phase-contrast X-ray computed tomography data (method *CT-mean*, **Figure 4.11a**). As another approach to quantify the widths of the imbibition fronts, the root mean square roughness profiles $R_{q,y}(D)$ obtained by method *CT-rms* were evaluated, which are displayed in **Figure 4.10b**. As a measure of the imbibition front width, the standard deviations σ_G of Gaussian fits to the peaks representing the imbibition front were determined (**Figure 4.11b**).

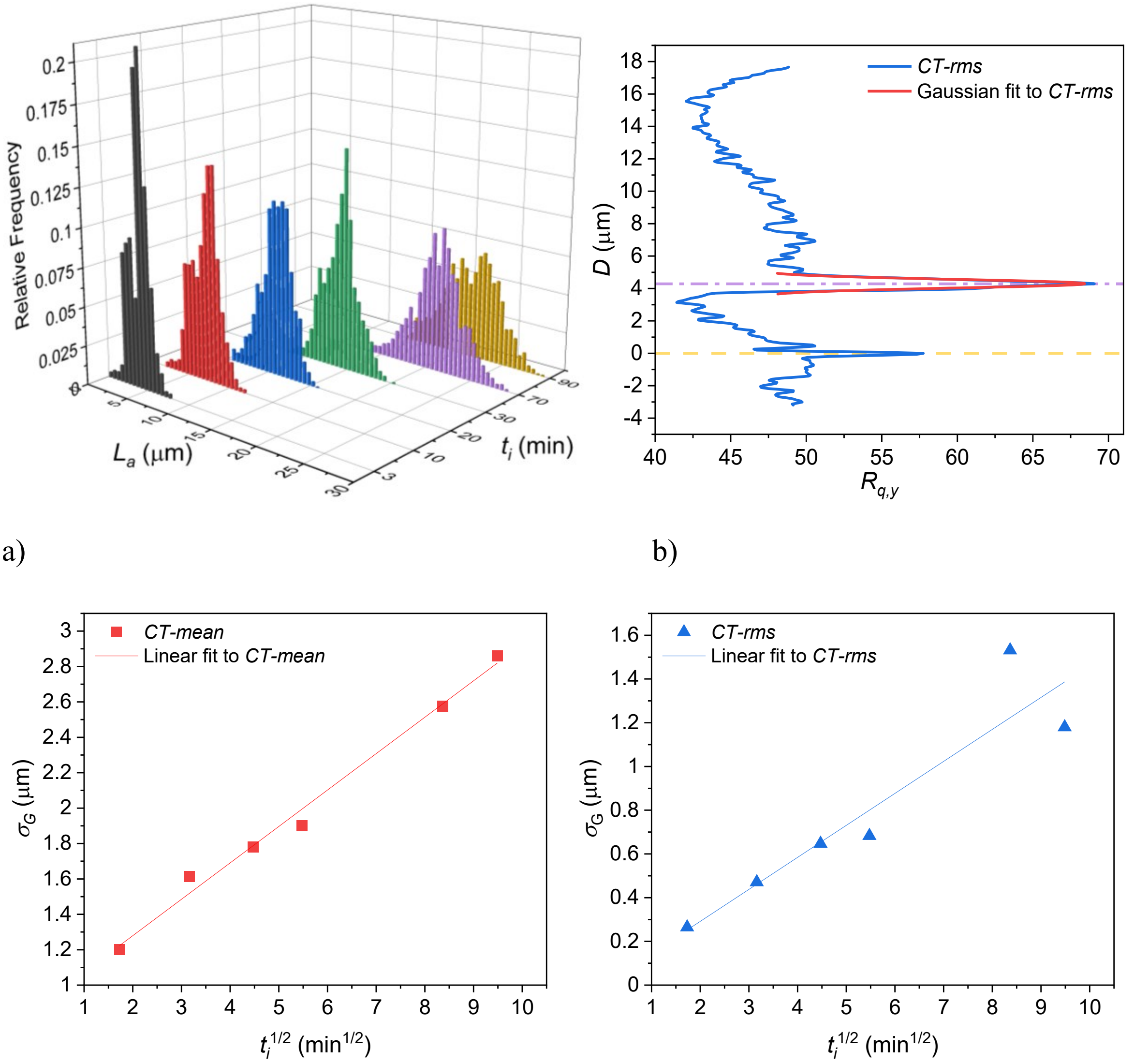

a) b)

c) d)

Figure 4.11. Evaluation of the imbibition front width in PS-infiltrated AAO. a), b) Histograms displaying the relative frequency of the single-pore imbibition length L_s (bin size $\Delta L_s = 0.5$ µm) for different infiltration times t_i obtained by methods a) *CT-mean* and b) *SEM-mean*. c) Gaussian fit (solid red line) to a $R_{q,y}(D)$ profile (root mean square roughness $R_{q,y}$ plotted against the distance D from the AAO surface) obtained by method *CT-rms*. Here, the $R_{q,y}(D)$ profile for $t_i = 3$ minutes is exemplarily shown. The dashed yellow line marks the position of the AAO surface and the purple dash-dot line the position of the imbibition front.

4.3 Comparative Analysis of X-ray CT Data of Imbibed AAO and CPG based on Real-Space Pixel Intensity Roughness

4.3.1 Batch extraction of roughness profiles

As discussed in Section 4.2.1, X-ray computed tomography of AAO and CPG membranes infiltrated with PS for different imbibition times t_i yielded volumetric reconstructions of the probed sample volumes consisting of 16-bit *xy* slices, which were approximately parallel to the membrane surfaces and the *xy* plane of the reference coordinate system (**Figure 4.1b,d**). While the volumetric reconstruction analysis algorithm employed in Section 4.2.1 based on pore center identification works for AAO membranes with pores oriented along the *z* axis and arranged in a hexagonal lattice, it is not applicable to CPG membranes in which the pores form spongy interconnected networks. For this purpose, an adapted version of method *CT-rms* was employed to analyze real space pixel intensity roughness of both AAO and CPG membranes, hereafter referred to as *Batch-CT-rms*.

At first, a suitable sub-volume of the volumetric reconstructions of the probed sample volume was selected. Using the software ImageJ,[128] the original 16-bit *xy* slices were resliced so as to obtain *xz* slices and tilt-corrected using an ImageJ reference grid. As a result, in the processed *xz* slices the membrane surface was horizontally oriented (**Figure 4.12**). The *z* axis was oriented normal to the membrane surface and parallel to the AAO pore axes (**Figure 4.12a**). The selected volumes of interest of the *xz* slices contained portions of the PS surface film, PS-filled pore segments and empty pore segments, while visible large artifacts, such as the edges of the sample or large cracks (green boxes in **Figure 4.1b,d**) were excluded.

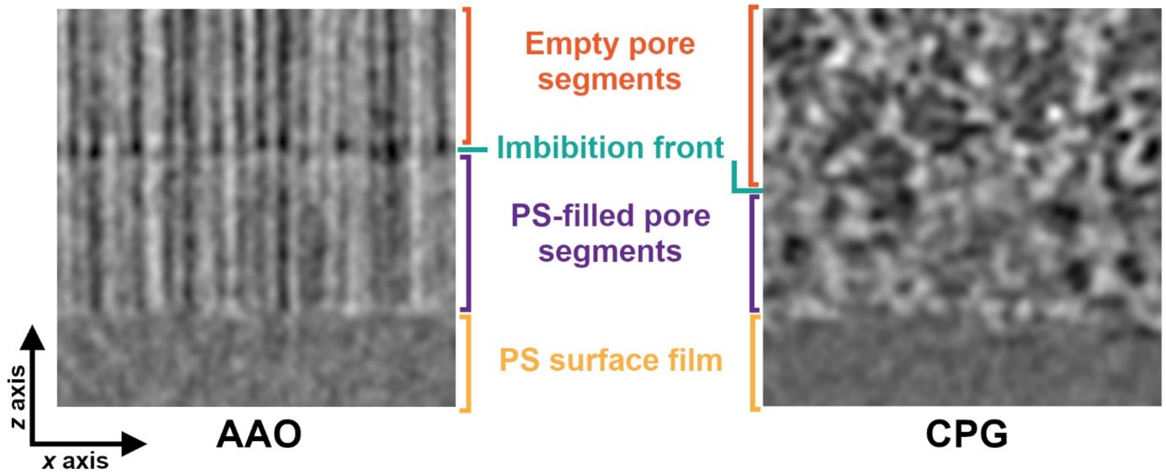

a) b)

Figure 4.12. Parts of processed a) AAO and b) CPG *xz* slices normal to the membrane surfaces obtained by X-ray computed tomography. The AAO and CPG membranes were infiltrated with PS for 3 min at 200°C. Each pixel has edge lengths of 64 nm and corresponds to one data point. The shown areas extend 10.05 x 10.05 µm^2. Empty parts of the membranes are seen at the top, membrane parts with PS-filled pore segments in the middle, and the bulk PS surface films on the membrane surfaces on the bottom. Empty membrane pores appear dark, the pore walls bright.

Secondly, a MATLAB (R2021a, MathWorks Corporation) script was used to extract matrices from the processed *xz* slices, in which gray values were assigned all combinations of x and z values representing positions of pixels. The pixel gray values were then normalized to a scale ranging from 0 to 1. For each row of pixels along the x direction parallel to the membrane surface a roughness value $R_{q,s}$ for the pixel brightness values was calculated according to Equation (4.2) (cf. Section 4.1.2).

Thus, for each *xz* slice a single-slice $R_{q,s}(D)$ profile was obtained that represents the average pixel roughness along a pixel row in x direction as a function of D. The single-slice $R_{q,s}(D)$ profiles are one-dimensional roughness tuples oriented normal to the membrane surfaces and parallel to the z direction, which can be considered projections of the properties of the two-dimensional *xz* slices along the x direction onto the z axis of the reference coordinate system.

Thirdly, all single-slice $R_{q,s}(D)$ profiles of the considered volume of interest were assembled into a two-dimensional array (“color map”) lying in the yz plane of the reference coordinate system (**Figure 4.13** and **Figure 4.14**). Each vertical pixel row parallel to the z axis represents a single-slice $R_{q,s}(D)$ profile. The sequence, in which the single-slice $R_{q,s}(D)$ profiles are arranged in the yz color maps, corresponds to the real-space sequence of the corresponding xz slices. Therefore, the yz color maps are two-dimensional $R_{q,s}$ maps of the probed sample volume in the yz plane; for each yz position, the $R_{q,s}$ values representing the dispersion of the pixel brightness along the x direction are plotted in the yz plane.

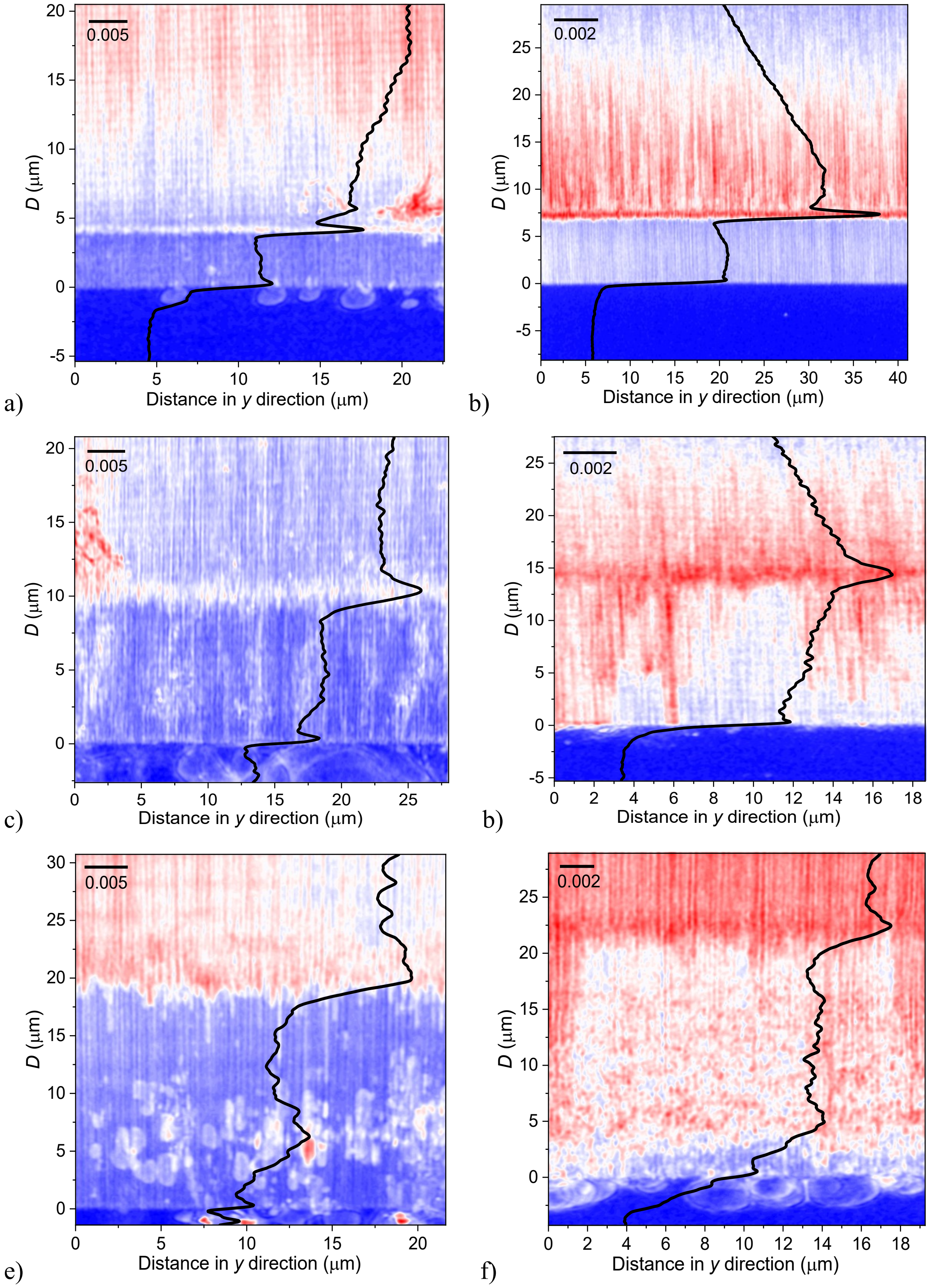

Figure 4.13. *yz* color maps of AAO membranes infiltrated with PS at 200°C, in which each vertical pixel column represents a single-slice $R_{q,s}(D)$ profile of an *xz* slice through the volumetric reconstruction of the sample volume obtained from X-ray computed tomography data. The distance *D* to the AAO membrane surface is plotted along the vertical axis (corresponding to the *z* direction reference coordinate system). The horizontal axis represents the *y* direction of the reference coordinate system in the probed sample volume. On the color maps the color map $R_{q,c}(D)$ profiles (black) are superimposed. The imbibition times t_i amounted to a) 3 minutes, b) 10 minutes, c) 20 minutes, d) 30 minutes, e) 70 minutes and f) 90 minutes.

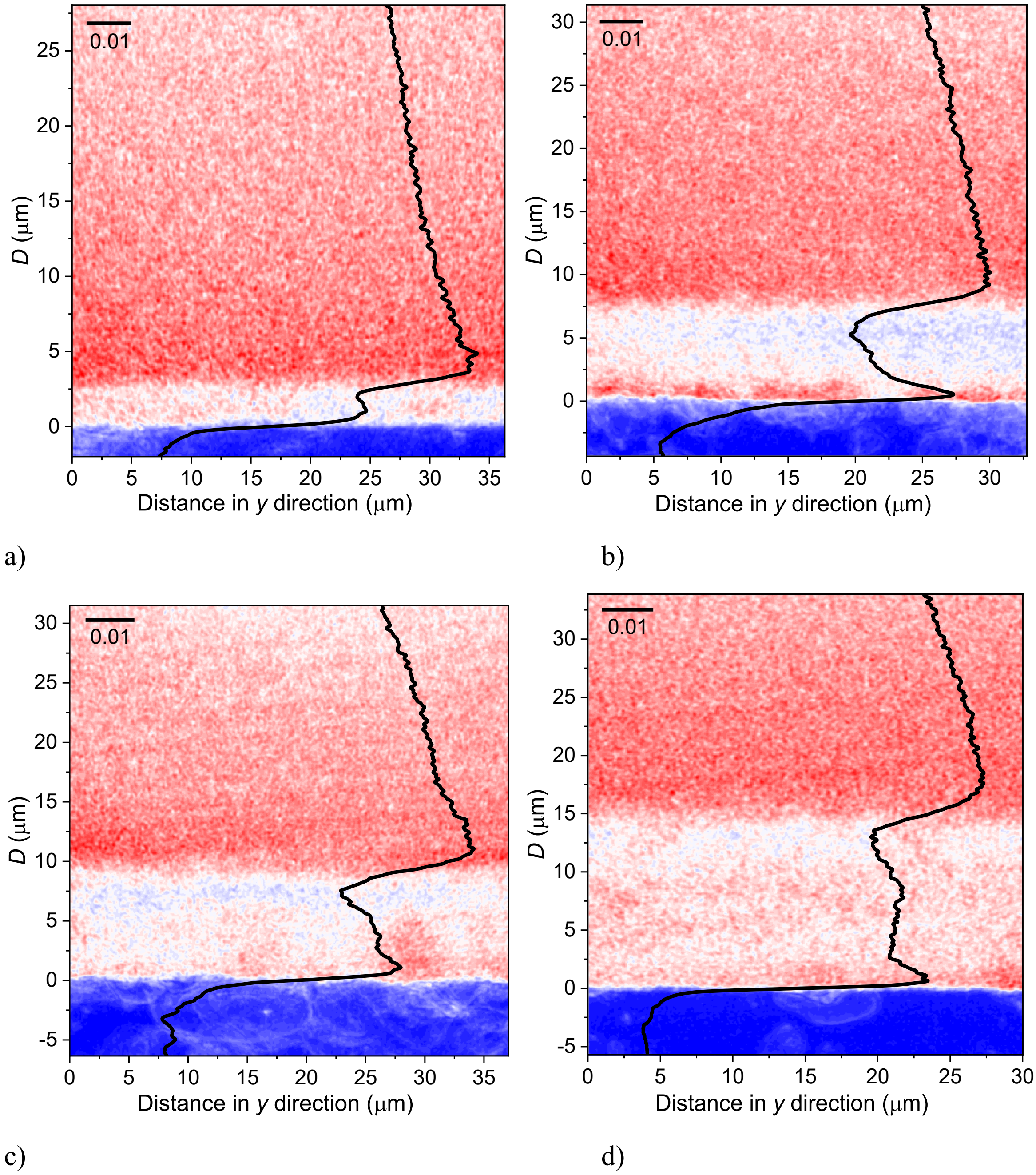

Figure 4.14. *yz* color maps of CPG membranes infiltrated with PS at 200°C, in which each vertical pixel column represents a single-slice $R_{q,s}(D)$ profile of an *xz* slice through the volumetric reconstruction of the sample volume obtained from X-ray computed tomography data. The distance *D* to the AAO membrane surface is plotted along the vertical axis (corresponding to the *z* direction reference coordinate system). The horizontal axis represents the *y* direction of the reference coordinate system in the probed sample volume. On the color maps, color map $R_{q,c}(D)$ profiles (black) are superimposed. The imbibition times t_i amounted to a) 3 minutes, b) 20 minutes, c) 30 minutes and d) 90 minutes.

Fourthly, color map $R_{q,c}(D)$ profiles (black curves in **Figure 4.13** and **Figure 4.14**) were calculated for each pixel row parallel to the *y* direction, that is, for each *D* value along the *z* axis:

$$R_{q,c} = \frac{1}{n}\sum_{j=1}^{n} R_{q,s,j} \qquad \text{(Equation 4.5)}$$

In Equation 4.5, n is the total number of considered *xz* slices corresponding to the total number of single slice $R_{q,s}(D)$ profiles assembled in the *yz* color maps. The index j represents the number of the *xz* slice yielding the considered single-slice $R_{q,s}(D)$ profile in the stack of *xz* slices representing the real-space structure of the volume of interest. The $R_{q,c}(D)$ profiles were calculated using the original 16 bit gray-scale single-slice $R_{q,s}(D)$ profiles, i.e., the color coding of the single-slice $R_{q,s}(D)$ profiles was only used for the color map visualizations. The color map $R_{q,c}(D)$ profiles are one-dimensional projections of the properties of the *yz* color maps. Since the latter are in turn 2D projections of the properties of the volume of interest in the *x* direction parallel to the membrane surfaces, the color map $R_{q,c}(D)$ profiles are one-dimensional representations of the properties of the volume of interest in the direction normal to the membrane surface. The three characteristic parts of PS-Infiltrated AAO (**Figure 4.15a**) and CPG (**Figure 4.15b**) membranes are represented by three distinct segments of the color map $R_{q,c}(D)$ profiles. The areas representing the bulk PS surface films (bottom in **Figure 4.15**) have the lowest pixel intensity dispersion, that is, the lowest $R_{q,c}(D)$ values. The surfaces of the AAO and CPG membranes separating the bulk PS surface film from PS-infiltrated membrane portions are marked by a stepwise increase (1) in the color map $R_{q,c}(D)$ profiles (**Figure 4.15**). The higher $R_{q,c}(D)$ values in the membrane portions filled with PS are caused by the pixel intensity differences between pixels located in the PS-filled pores and pixels located in the PS-filled pore walls (pixels intersected by the pore walls have intermediate pixel intensities). The position of the imbibition front is marked by a second stepwise increase (2) in $R_{q,c}(D)$ because the difference in the pixel intensities between pixels located in the oxidic pore walls and in empty pores is even more pronounced than the difference in the pixel intensities between pixels located in the oxidic pore walls and in PS-filled pore segments. The stepwise increases (1) in $R_{q,c}(D)$ representing the membrane surfaces as well as the stepwise increases (2) in color map $R_{q,c}(D)$ profiles obtained from AAO samples representing the imbibition fronts in the AAO samples are superimposed by peaks. Only the stepwise increases (2) in color map $R_{q,c}(D)$ profiles obtained from CPG samples representing the imbibition fronts in the CPG samples have classical step-like shapes. Therefore, for AAO and CPG membranes different approaches were used to obtain the average imbibition lengths L_a and measures of the imbibition front widths.

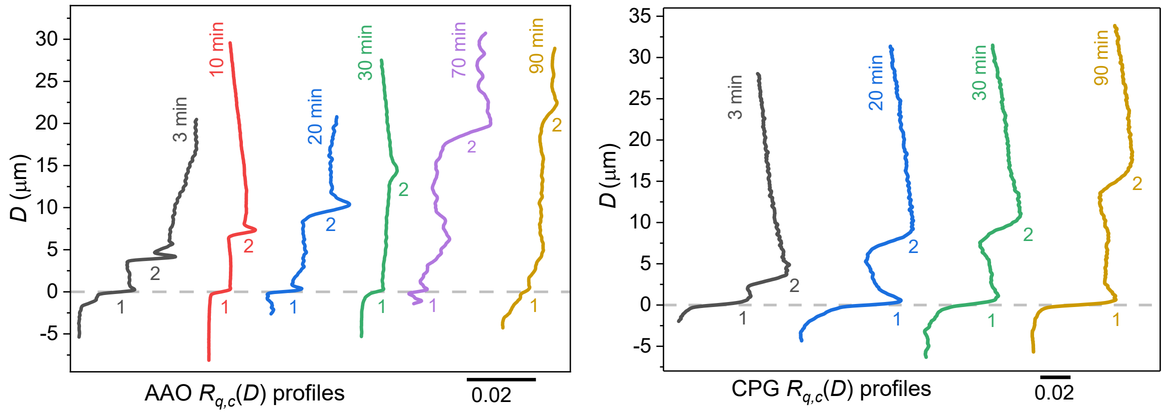

a) b)

Figure 4.15. $R_{q,c}(D)$ profiles plotted against the distance D to the membrane surface obtained for PS-infiltrated AAO and CPG membranes by evaluation of X-ray computed tomography data and their analysis to determine the average imbibition front position L_a and to quantify the imbibition front width. The positions of the membrane surfaces at $D \approx 0$ µm are indicated by dashed grey lines and the $R_{q,c}$ steps labelled (1). The $R_{q,c}$ steps labelled (2) indicate the average positions L_a of the imbibition front. a) AAO $R_{q,c}(D)$ profiles. b) CPG $R_{q,c}(D)$ profiles. a) AAO $R_{q,c}(D)$ profiles containing ~2705 pores ($t_i = 3$ min), ~7166 pores ($t_i = 10$ min), ~3041 pores ($t_i = 20$ min), ~2830 pores ($t_i = 30$ min), ~3216 pores ($t_i = 70$ min) and ~2961 pores ($t_i = 90$ min). The pore numbers were estimated by assuming a perfect hexagonal pore lattice with a lattice constant of 500 nm. b) CPG $R_{q,c}(D)$ profiles, the analyzed volumes of interest amounted to ~32834 µm^3 ($t_i = 3$ min), 41940 µm^3 ($t_i = 20$ min), 53194 µm^3 for ($t_i = 30$ min) and 47108 µm^3 ($t_i = 90$ min).

4.3.2 Determination of average imbibition lengths and imbibition front width descriptors of AAO and CPG

The average imbibition lengths L_a for AAO samples were determined as follows. The first derivatives d$R_{q,c}$/dD of the color map $R_{q,c}(D)$ profiles were calculated. Then, the positions of the maxima of the two largest peaks of the first derivatives d$R_{q,c}$/dD were identified, which represent the AAO membrane surface at $D = 0$ µm (peak (1) and the green dashed line in **Figure 4.16a**) and the position of the imbibition front (peak (2) and the purple dashed-dot line in **Figure 4.16a**). The distances between the maxima (1) and (2) were assumed to correspond to the average imbibition lengths L_a. As a descriptor of the imbibition front width, the standard deviations σ_G of Gaussian fits (red solid line in **Figure 4.16a**) to the peaks (2) of the color map $R_{q,c}$(D) profiles were calculated. The obtained L_a and σ_G are shown in **Figure 4.17**.

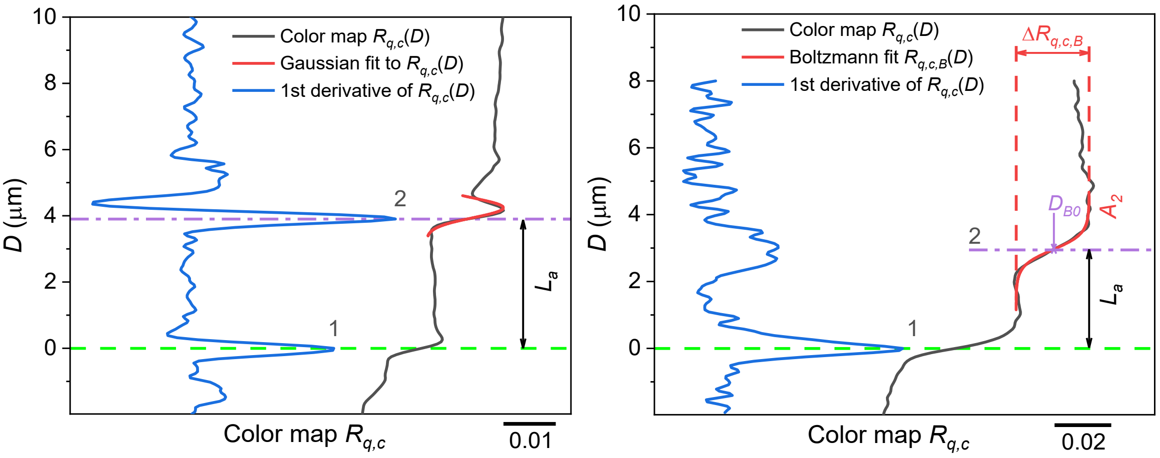

a) b)

Figure 4.16. Determination of the average imbibition lengths L_a and measures of the imbibition front widths for PS-infiltrated AAO and CPG membranes. a) AAO color map $R_{q,c}(D)$ profile (black) for $t_i = 3$ min, its first derivative $dR_{q,c}/dD$ (blue) and a Gaussian fit (red) to the color map $R_{q,c}(D)$ profile in the D range where the imbibition front is located. L_a is the difference between the D values of the peak maximum positions of the 1st derivative $dR_{q,c}/dD$ indicating the presence of the imbibition front [peak (2), purple dashed-dot line] and the AAO surface at $D = 0$ µm [peak (1); green dashed line]. b) CPG color map $R_{q,c}(D)$ profile (black) for $t_i = 3$ min, its first derivative $dR_{q,c}/dD$ (blue) and a sigmoidal Boltzmann fit $R_{q,c,B}(D)$ (red) to the color map $R_{q,c}(D)$ profile in the D range where the imbibition front is located. L_a is the difference between the D values of the peak maximum position (1) of the 1st derivative indicating the position of the CPG surface (green dashed line) and D_{B0}, which is the D value at the half height of $\Delta R_{q,c,B}$ step (2) of the sigmoidal Boltzmann fit indicating the position of the imbibition front (purple dash-dot line). A_2 is the maximum value of the sigmoidal Boltzmann fit $R_{q,c,B}$ representing the non-infiltrated part of the CPG membrane.

The average imbibition lengths L_a for CPG samples were obtained as follows. The first derivatives $dR_{q,c}/dD$ of the color map $R_{q,c}(D)$ profiles were calculated. Then, the peak maximum positions of peaks (1) marking the CPG surface at $D = 0$ µm were determined (green dashed line in **Figure 4.16b**). The steps (2) in the color map $R_{q,c}(D)$ profiles were fitted with a sigmoidal Boltzmann function:

$$R_{q,c,B}(D) = \frac{\Delta R_{q,c}}{1+exp\left(\frac{D-D_{B0}}{k_B}\right)} + A_2 \qquad \text{Equation 4.6}$$

$R_{q,c,B}(D)$ is the value of the sigmoidal Boltzmann function at a distance D to the CPG surface. $\Delta R_{q,c,B}$ is the height of step (2) in the $R_{q,c,B}(D)$ curves. A_2 is the maximum value of $R_{q,c,B}$ representing non-infiltrated parts of the CPG membranes with empty pore segments, whereas D_{B0} is the D value at the half-heights of steps (2) and represents the positions of the imbibition fronts. L_a was determined as the difference between the positions of the inflection points D_{B0} of the sigmoidal Boltzmann fits (red solid lines in **Figure 4.16b**) to steps (2) of the $R_{q,c,B}(D)$ fits and the maxima of peaks (1) of the first derivatives $\mathrm{d}R_{q,c}/\mathrm{d}D$ of the color map $R_{q,c}(D)$ profiles marking the CPG surfaces. The slope factors k_B represent the steepness of steps (2). Plots of the obtained L_a and k_B values against the imbibition time t_i are shown in **Figure 4.18**.

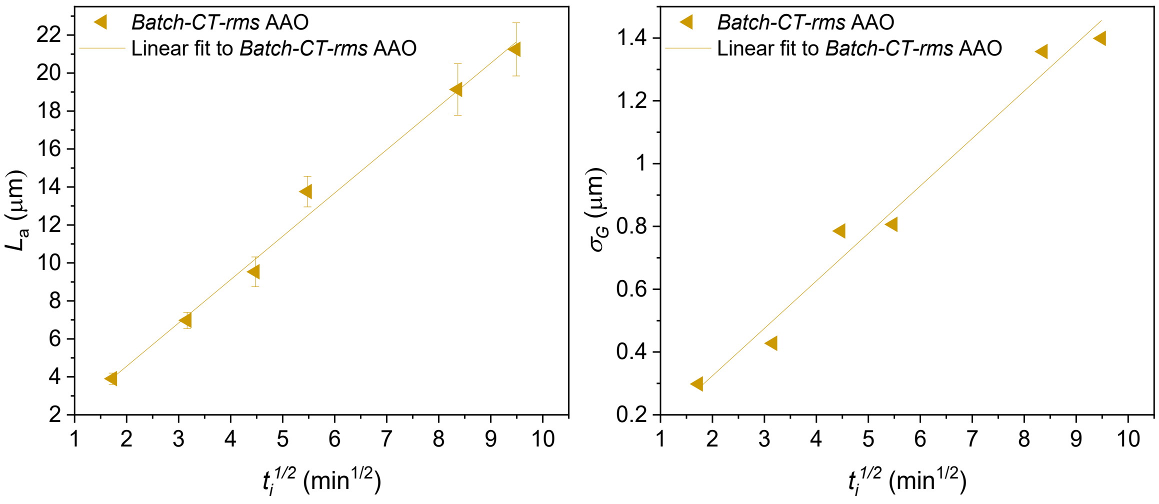

a)

b)

Figure 4.17. a) L_a plotted against the square root of the imbibition time $t_i^{1/2}$ for AAO. Error bars correspond to σ_G as descriptor of imbibition front width. b) Imbibition front width descriptor σ_G plotted against the square root of the imbibition time $t_i^{1/2}$. Solid lines are linear fits to sets of data points obtained with AAO membranes.

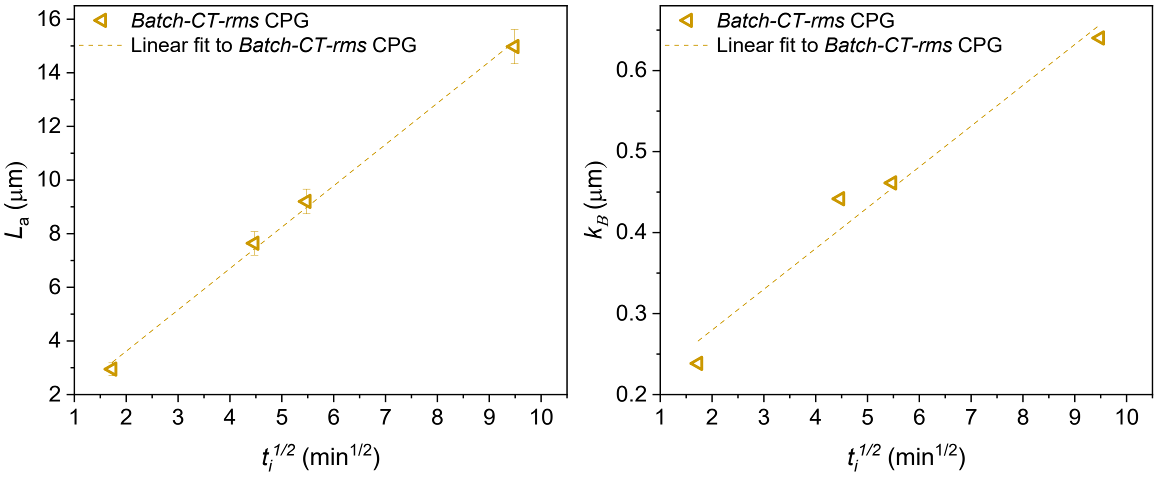

a)

b)

Figure 4.18. a) L_a plotted against the square root of the imbibition time $t_i^{1/2}$ for CPG. Error bars correspond to k_B as descriptor of imbibition front width. b) Imbibition front width descriptor k_B plotted against the square root of the imbibition time $t_i^{1/2}$. Dashed lines are linear fits to sets of data points obtained with CPG membranes.

4.4 Analysis of EDX Data

4.4.1 Determination of imbibition lengths and imbibition front width descriptors of AAO and CPG samples

The sponge-like structure of the CPG pores (**Figure 4.19b**) makes it challenging to identify the boundaries of the PS-infiltrated portions of the CPG membranes by visual inspection. Therefore, another method, hereafter referred to as *EDX-rms*, was developed for the evaluation of EDX elemental mappings that allows to determine the average imbibition lengths L_a and to quantify imbibition front widths.

The average position L_a of the imbibition fronts, as well as measures of the imbibition front widths, were determined by statistical evaluation of 8-bit 2D EDX maps of the intensity of the carbon Kα peak indicating the distribution of PS, which predominantly consists of carbon (**Figure 4.20** and **Figure 4.21**). In **Figure 4.19**, exemplary EDX carbon Kα maps and the corresponding SEM images of cross-sections of AAO and CPG membranes infiltrated with PS for 3 minutes are displayed. It shows the relevant features of a PS-infiltrated AAO and CPG membranes, at the bottom the PS surface film on the membrane surfaces, in the middle PS-filled pore segments and at the top the empty parts of the membranes.

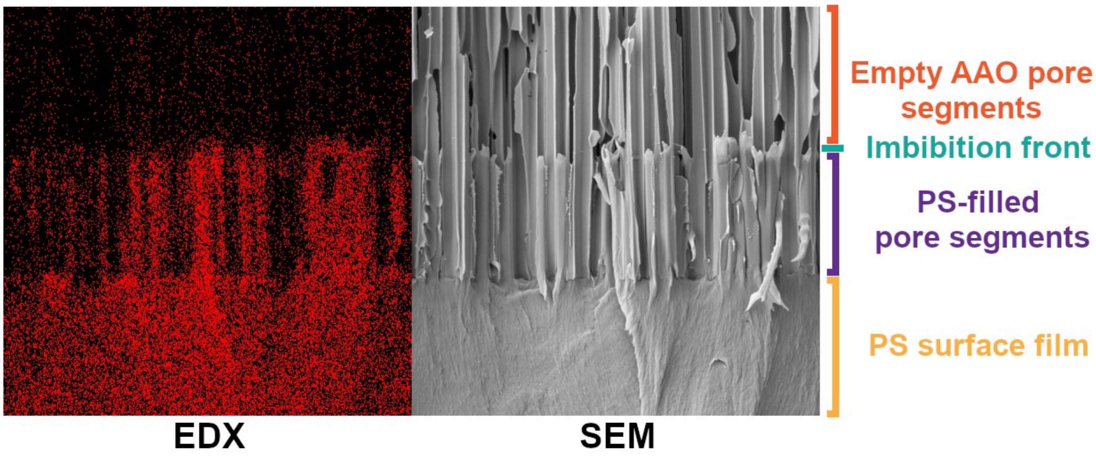

a)

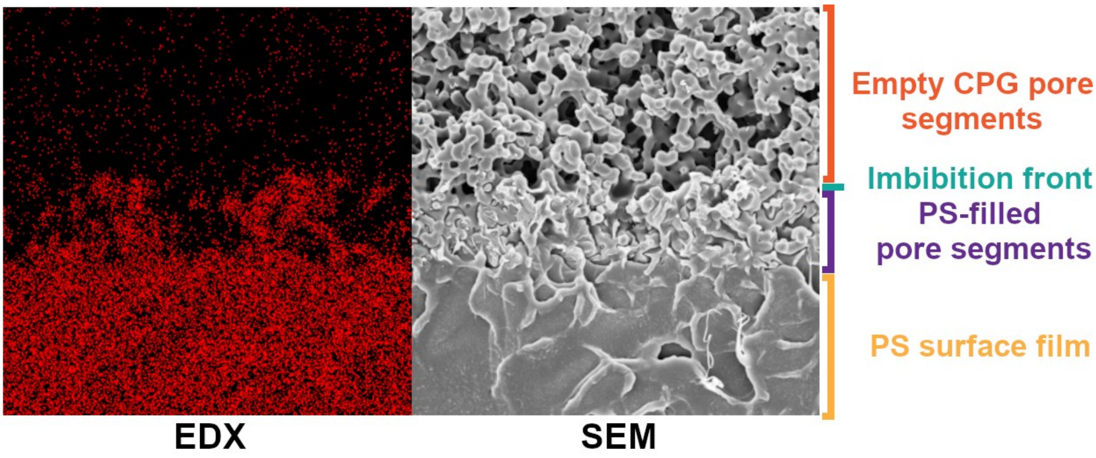

b)

Figure 4.19. Exemplary 2D EDX maps showing the intensity of the carbon Kα peak and SEM images of cross sections of a) AAO and b) CPG infiltrated with PS for t_i = 3 minutes at 200°C. At the top, empty parts of the membranes are seen. PS-filled pore segments are seen in the middle. At the bottom, bulk PS surface films are seen. The shown areas extend 14.47 x 14.47 µm^2.

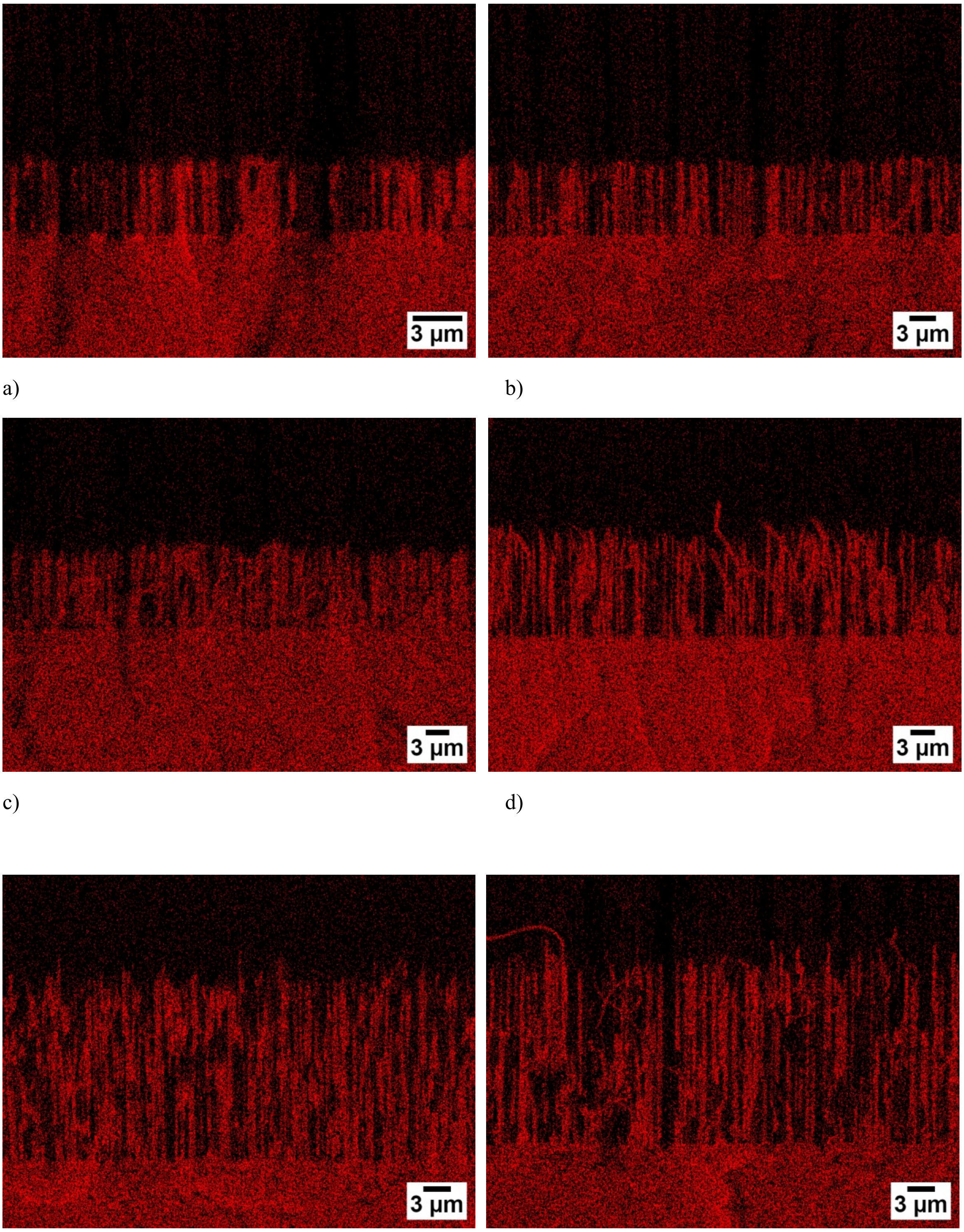

a) b)

c) d)

e) f)

Figure 4.20. 2D EDX maps showing the intensity of the carbon Kα peak of cross-sections of AAO membranes infiltrated with PS at 200 °C for a) 3 minutes, b) 10 minutes, c) 20 minutes, d) 30 minutes, e) 70 minutes and f) 90 minutes. Red pixels indicate the presence of carbon. At the top, empty parts of the AAO membranes are seen. PS-filled pore segments are seen in the middle. At the bottom, bulk PS surface films are seen.

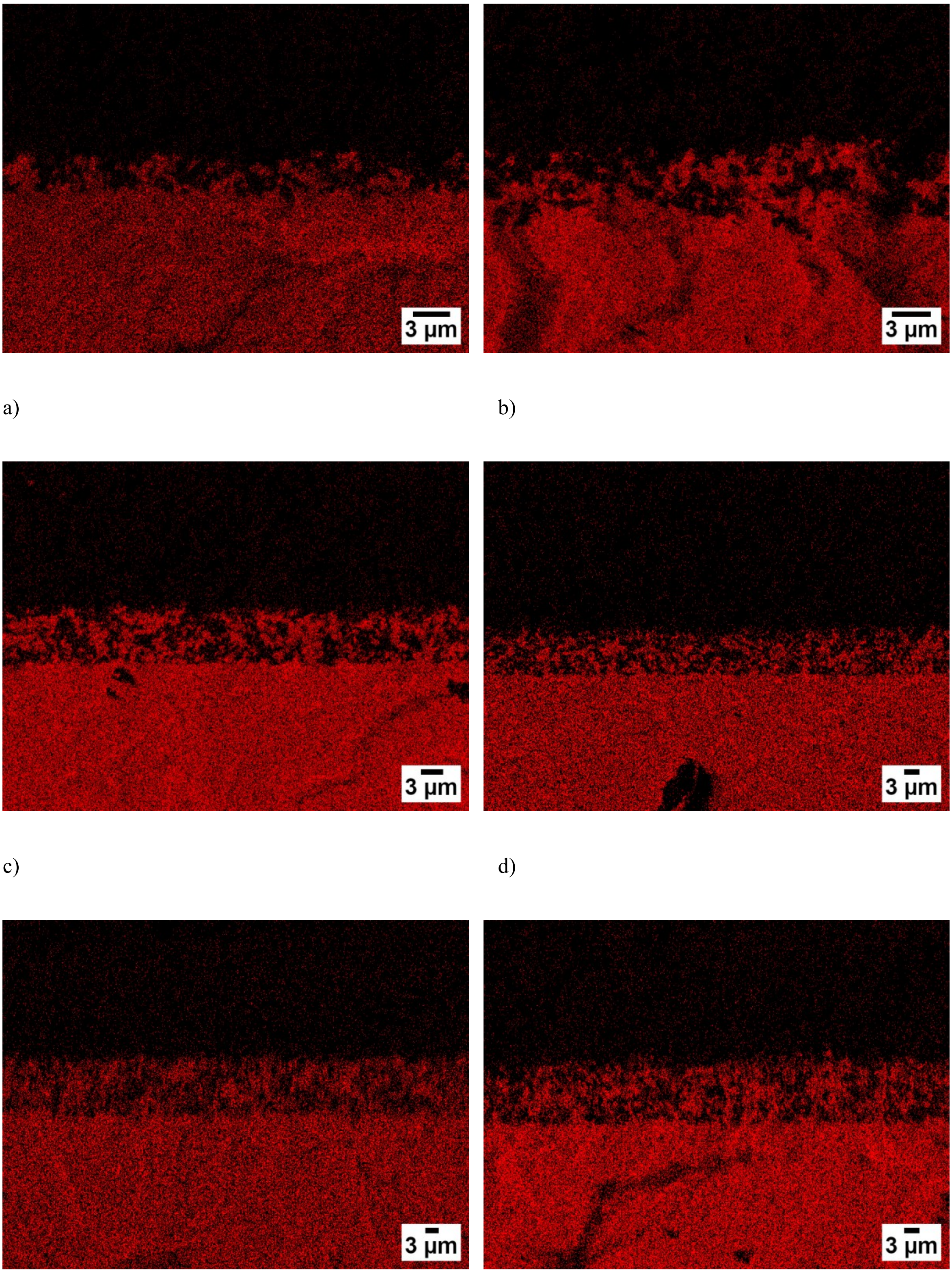

a) b)

c) d)

e) f)

Figure 4.21. 2D EDX maps showing the intensity of the carbon Kα peak of cross-sections of CPG membranes infiltrated with PS at 200 °C for a) 3 minutes, b) 10 minutes, c) 20 minutes, d) 30 minutes, e) 70 minutes and f) 90 minutes. Red pixels indicate the presence of carbon. At the top, empty parts of the CPG membranes are seen. PS-filled pore segments are seen in the middle. At the bottom, bulk PS surface films are seen.

The average root mean square roughness $R_{q,EDX}$ of the pixel intensities along rows of pixels in the x direction parallel to the surfaces of the AAO and CPG membranes was calculated in the same manner as described in Section 4.1.2 according to Equation (4.3).

The $R_{q,EDX}(D)$ profiles for all infiltration times t_i exhibited two $R_{q,EDX}$ steps (**Figure 4.23**). The highest $R_{q,EDX}$ values were found in pixel rows located in the bulk PS films connected to the surfaces of the AAO and CPG membranes (bottom of **Figure 4.22a,b** and **Figure 4.23a,b**). While the entire probed volume consists of PS, local fluctuations in the carbon Kα peak intensity result in high $R_{q,EDX}$ values. The surfaces of the AAO and CPG membranes separating the bulk PS surface film from PS-infiltrated membrane portions are apparent by a stepwise decrease in $R_{q,EDX}$ (step (1) in **Figure 4.23**). The areas occupied by the pore walls are free of carbon. In these areas, no carbon Kα intensity was detected so that no local pixel intensity fluctuations occur. The imbibition front is indicated by a second stepwise decrease in $R_{q,EDX}$ (step (2) in **Figure 4.23**) since beyond the imbibition front only a small number of separated, scattered red pixels is present. Hence, the pixel rows predominantly consist of black pixels with little pixel intensity variations.

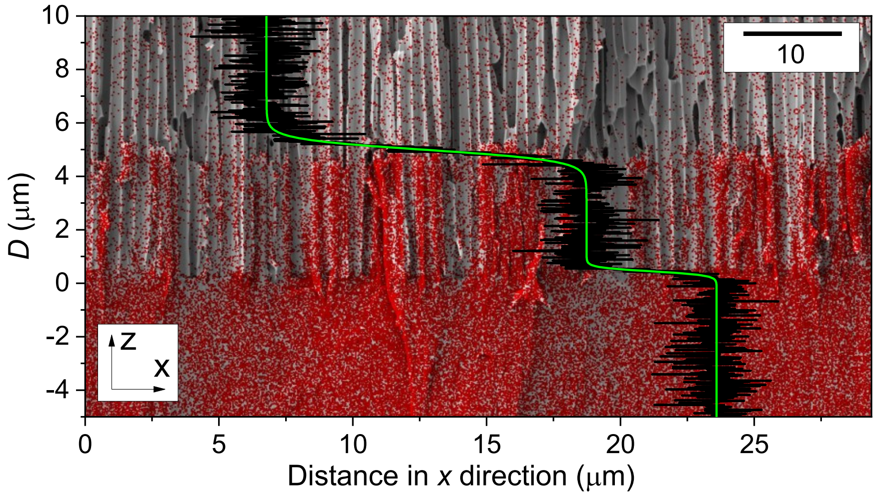

a)

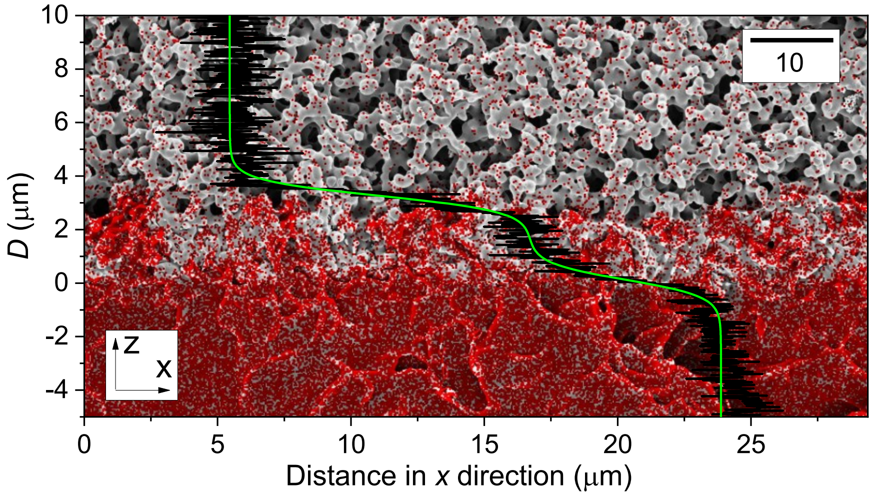

b)

Figure 4.22. 2D EDX maps of the carbon Kα peak at 0.277 keV of cross-sections of a) an AAO membrane and b) a CPG membrane infiltrated with PS for 3 minutes at 200 °C. The EDX maps are superimposed on SEM images of the mapped areas. The distance *D* to the membrane surface is plotted along the vertical axes corresponding to the *z* axis of the external reference coordinate system. Empty parts of the membranes are seen at the top, membrane parts with PS-filled pore segments in the middle, and the bulk PS surface films on the membrane surfaces on the bottom. The noisy black curves superimposed on the EDX maps are $R_{q,EDX}(D)$ profiles of the roughness $R_{q,EDX}$ of the pixel intensities on an 8-bit scale encompassing 256 shades of red. The $R_{q,EDX}(D)$ profiles represent the intensity of the carbon Kα peak along pixel rows in *x* direction parallel to the membrane surfaces (in the case of AAO normal to the pores) at specific distances *D* from the membrane surfaces. The smooth green curves are double-Boltzmann fits to the $R_{q,EDX}(D)$ curves. The length of the scale bars corresponds to $R_{q,EDX} = 10$.

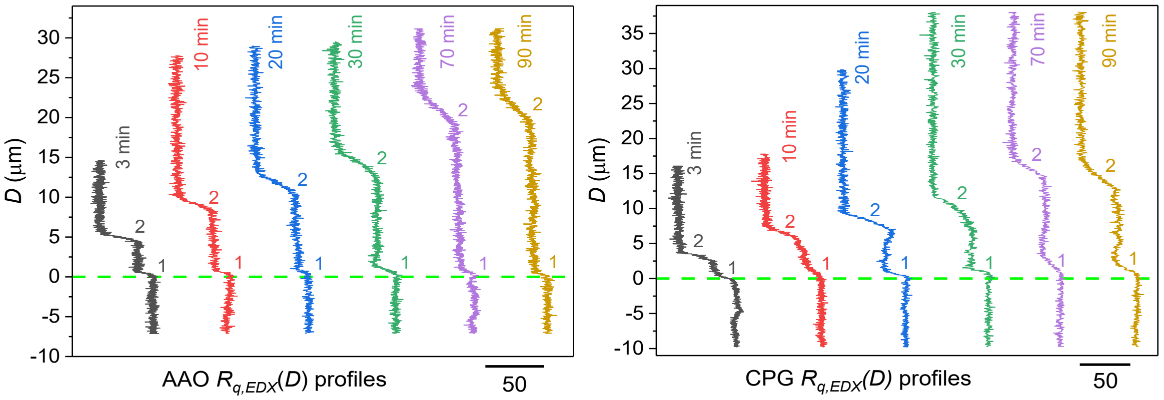

a) b)

Figure 4.23. Statistical evaluation of pixel intensities representing the carbon Kα peak intensities in 2D EDX maps of cross-sectional specimens of a) AAO membranes and b) CPG membranes infiltrated with PS for different imbibition times t_i. The mean roughness $R_{q,EDX}$ of pixel intensities along pixel rows in the x direction parallel to the membrane surface is plotted against the distance D to the membrane surface measured along the z axis of the reference coordinate system. The $R_{q,EDX}$ steps labelled (1) at $D \approx 0$ µm (green dotted line) mark the position of the membrane surface. The $R_{q,EDX}$ steps labelled (2) indicate the average position L_a of the imbibition front. The AAO samples evaluated for panel a) extended 29.40 µm (t_i = 3 min), 55.85 µm (t_i = 10 min), 65.06 µm (t_i = 20 min), 62.06 µm (t_i = 30 min), 53.89 µm (t_i = 70 min) and 54.37 µm (t_i = 90 min) in the x direction parallel to the membrane surface. The CPG samples evaluated for panel b) extended 39.54 µm (t_i = 3 min), 36.83 µm (t_i = 10 min), 67.64 µm (t_i = 20 min), 100.00 µm (t_i = 30 min), 113.27 µm (t_i = 70 min) and 100.39 µm (t_i = 90 min) in the x direction parallel to the membrane surface.

To calculate the average imbibition length L_a, a double sigmoidal Boltzmann function[129] was fitted to the $R_{q,EDX}(D)$ profiles using the software Origin 2020 (OriginLab Corporation):[130]

$$R_{q,dB}(D) = R_{q,0} + A\left[\frac{p}{1+exp\left(\frac{D-D_{EDX,1}}{k_{EDX,1}}\right)} + \frac{1-p}{1+exp\left(\frac{D-D_{EDX,2}}{k_{EDX,2}}\right)}\right] \qquad \text{(Equation 4.7)}$$

$R_{q,dB}(D)$ is the value of the double-Boltzmann fit function at a specific D value (smooth green curves in **Figure 4.22**). $R_{q,0}$ is the $R_{q,dB}$ value in the D range belonging to the bulk PS surface film covering the membrane surfaces. $R_{q,0} + A$ is the $R_{q,dB}$ value in the D range belonging to the membrane parts with empty pore segments ahead of the imbibition front. A is the sum of the heights of the two $R_{q,dB}$ steps (1) and (2) at the membrane surface and the imbibition front. $A \bullet p$ is the height of the $R_{q,dB}$ step (1) at the membrane surface and $A \bullet (1 - p)$ the height of $R_{q,dB}$ step (2) at the imbibition front. $D_{EDX,1}$ is the D value at the half-height of $R_{q,dB}$ step (1), and $D_{EDX,2}$ is the D value at the half-height of $R_{q,dB}$ step (2). L_a was calculated (**Figure 4.24a,c**) as the difference between $D_{EDX,2}$ and $D_{EDX,1}$. The slope factors $k_{EDX,1}$ and $k_{EDX,2}$ represent the steepness of $R_{q,dB}$ steps (1) and (2) in the $R_{q,dB}(D)$ profiles. The slope factor $k_{EDX,2}$ is a suitable descriptor of the imbibition front width. If $k_{EDX,2}$ approaches infinity, the slope of step (2) approaches zero, i.e., step (2) vanishes. If $k_{EDX,2}$ approaches zero, the slope of step (2) approaches infinity, i.e., step (2) is then vertical. The smaller $k_{EDX,2}$ is, the steeper is step (2) and the narrower is the imbibition front. As $k_{EDX,2}$ increases, the steepness of step (2) decreases and the imbibition front width increases (**Figure 4.24,d**).

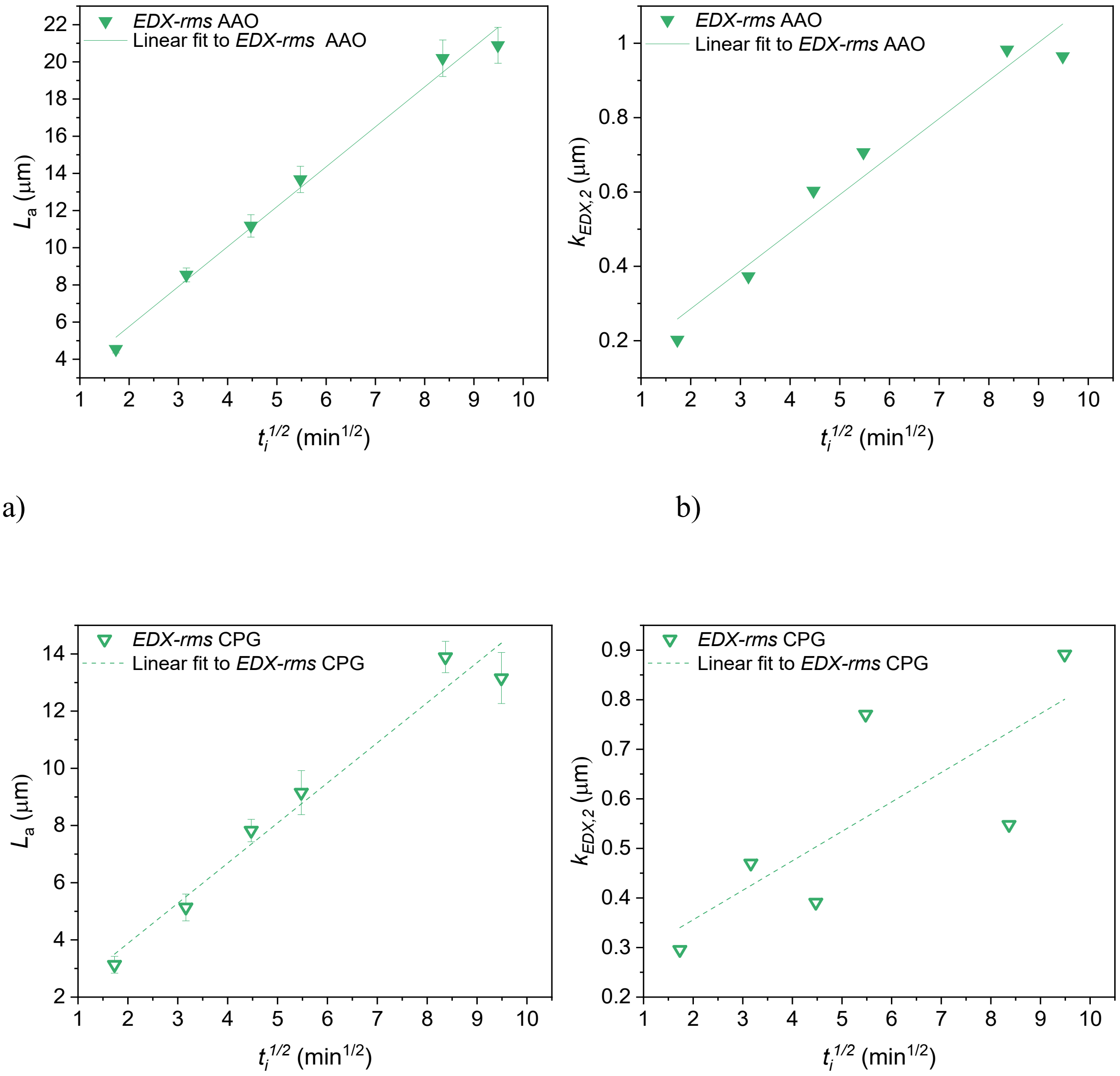

a)

b)

c)

d)

Figure 4.24. a, c) Average imbibition lengths $L_a(t_i)$ and b), d) slope factors $k_{EDX,2}$ as descriptors of imbibition front widths for a), b) AAO and c), d) CPG membranes infiltrated with PS at 200 °C obtained with method *EDX-rms*. Solid symbols represent data points obtained for AAO membranes, open symbols data points obtained for CPG membranes. Solid lines are fits to sets of data points obtained with AAO membranes and dashed lines are fits to sets of data points obtained with CPG membranes. Error bars correspond to the slope factors $k_{EDX,2}$. a) L_a plotted against the square root of the imbibition time $t_i^{1/2}$ for AAO. b) The slope factors $k_{EDX,2}$ of step 2 (position of the imbibition front) of double sigmoidal Boltzmann functions fitted to $R_{q,EDX}(D)$ profiles as measures of the imbibition front width for AAO plotted against the square root of the imbibition time $t_\mathrm{i}^{1/2}$. c) L_a plotted against the square root of the imbibition time $t_i^{1/2}$ for CPG. d) The slope factors $k_{EDX,2}$ of step 2 (position of the imbibition front) of double sigmoidal Boltzmann functions fitted to $R_{q,EDX}(D)$ profiles as measures of the imbibition front width for CPG plotted against the square root of the imbibition time $t_\mathrm{i}^{1/2}$.

4.5 Mean Imbibition Lengths and Imbibition Front Width Descriptors by Analysis of Cross-sectional SEM Images

4.5.1 Evaluation of imbibition lengths, and determination of imbibition front width descriptors of AAO samples

Three AAO membranes were infiltrated for each specific infiltration time $t_{i,}$ under the same conditions (cf. Section 3.2). Then, the single-pore imbibition lengths L_s, which correspond to the red vertical lines in **Figure 4.25b**, were determined for 10 pores per AAO membrane using the software ImageJ[124] measuring from the membrane surface, indicated with a green horizontal line in **Figure 4.25b,** to the menisci indicated with a blue arrow in **Figure 4.25a**. Thus, overall 30 AAO pores of three different AAO membranes were evaluated for each t_i value. **Figure 4.26** shows representative cross-sectional SEM images of AAO membranes infiltrated with PS at 200°C a) for 3 minutes, b) for 10 minutes, c) for 20 minutes, d) for 30 minutes, e) 70 minutes and f) for 90 minutes obtained with a SESI detector. This approach is, hereafter, referred to as *SEM-mean*.

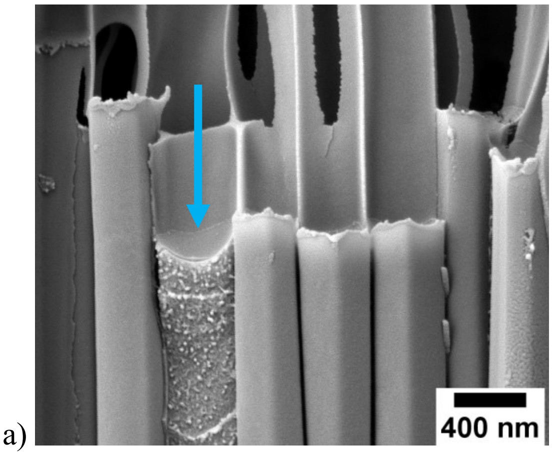

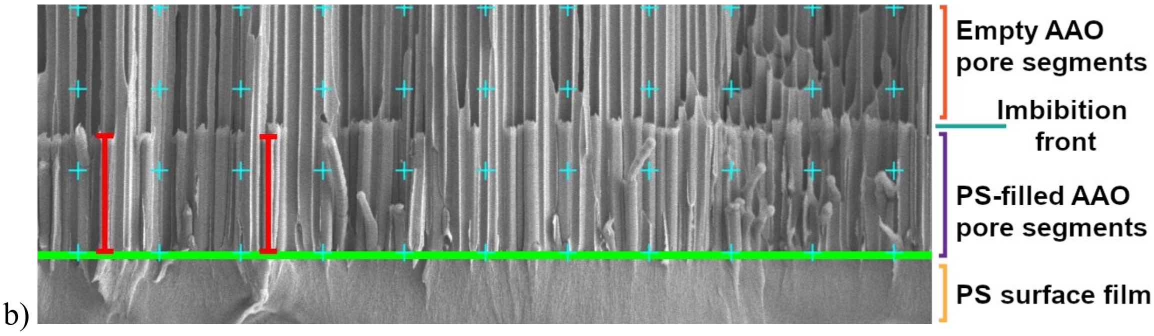

Figure 4.25. a) SEM image of an AAO membrane infiltrated with PS with M_w: 24.7 kg/mol at 140°C for 10 minutes, cleaved parallel to the AAO pores showing the cross-section of a meniscus (blue arrow). PS with M_w: 24.7 kg/mol was exclusively used here to obtain the detail of the menisci due to a more brittle characteristic allowing the PS segment cross-section to be visible. b) SEM image of an AAO membrane infiltrated with PS with M_w: 239 kg/mol at 200°C for 3 minutes. At the bottom, a bulk PS film covering the AAO surface is seen. The green line marks the AAO surface. Above the green line in the center of the micrograph, PS-filled AAO pore segments and at the top empty AAO pore segments are seen. The closed bottoms of the AAO pores are at the very top outside the image. The grid marked by blue crosses helped align the AAO surface horizontally and the AAO pore axes vertically. The red lines indicate single-pore imbibition lengths L_s.

The SEM image displayed in **Figure 4.25b** shows the relevant features of a PS-infiltrated AAO membrane. At the bottom, a bulk PS film located on the AAO surface, which is seen as homogeneous grey area. The AAO surface between the bulk PS surface film and the part of the AAO membrane infiltrated with PS is marked by a green horizontal line. In the center, AAO pore segments filled with PS are seen. At the top, empty AAO pore segments are seen (the closed AAO pore bottoms are at the very top outside the image field).

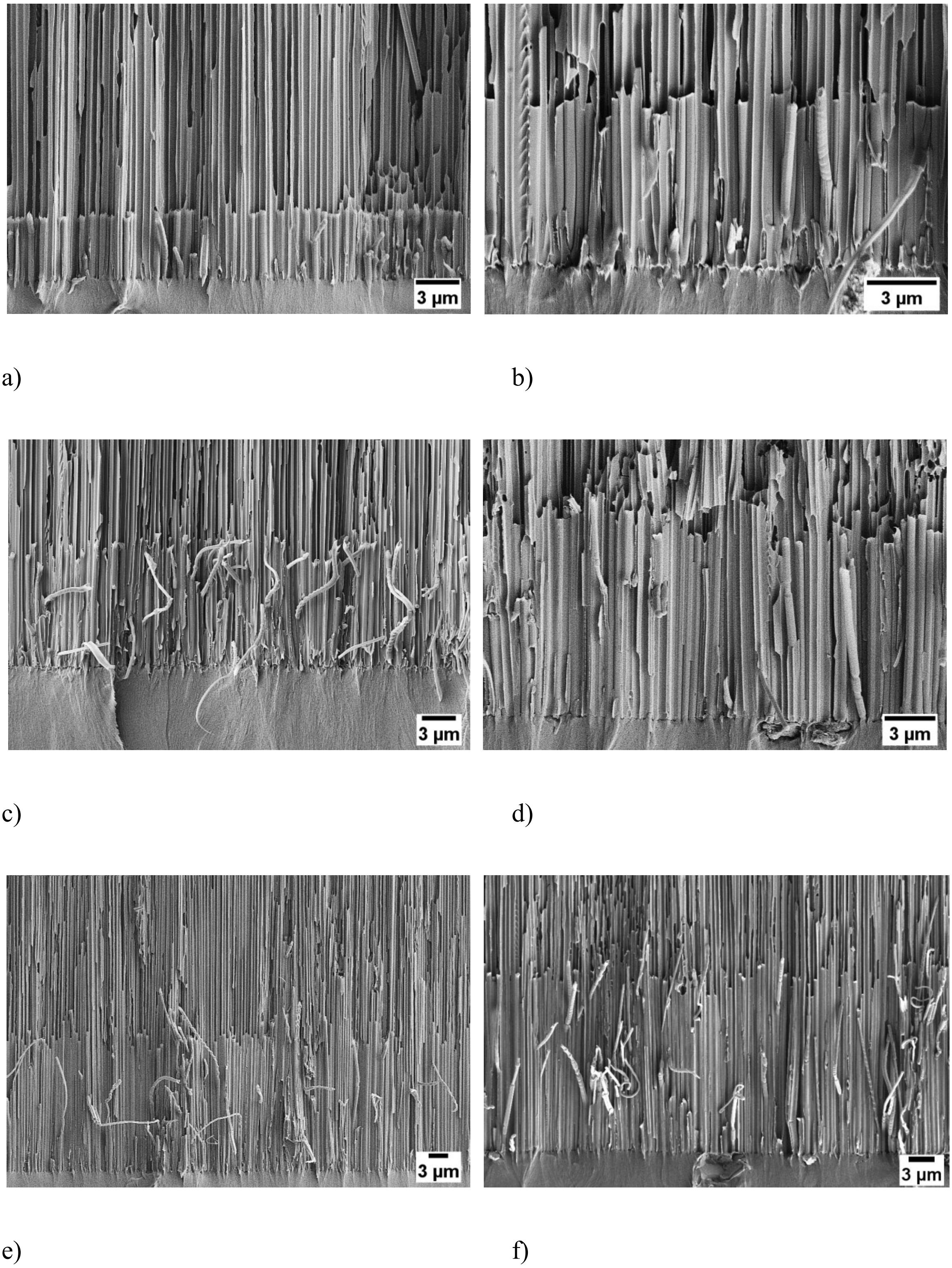

Figure 4.26. SEM cross-sectional images of AAO membranes infiltrated with PS at 200°C a) for 3 minutes, b) for 10 minutes, c) for 20 minutes, d) for 30 minutes, e) 70 minutes and f) for 90 minutes. All images were obtained with a SESI detector.

The average imbibition lengths L_a shown in **Figure 4.27a**, were then calculated as the arithmetic mean value of the L_s values and fitted with a linear function using the software Origin 2019 (OriginLab Corporation)[130]. The standard deviation σ, shown in **Figure 4.27b** of the L_s histograms (**Figure 4.27c**) was employed as measure of the imbibition front width.

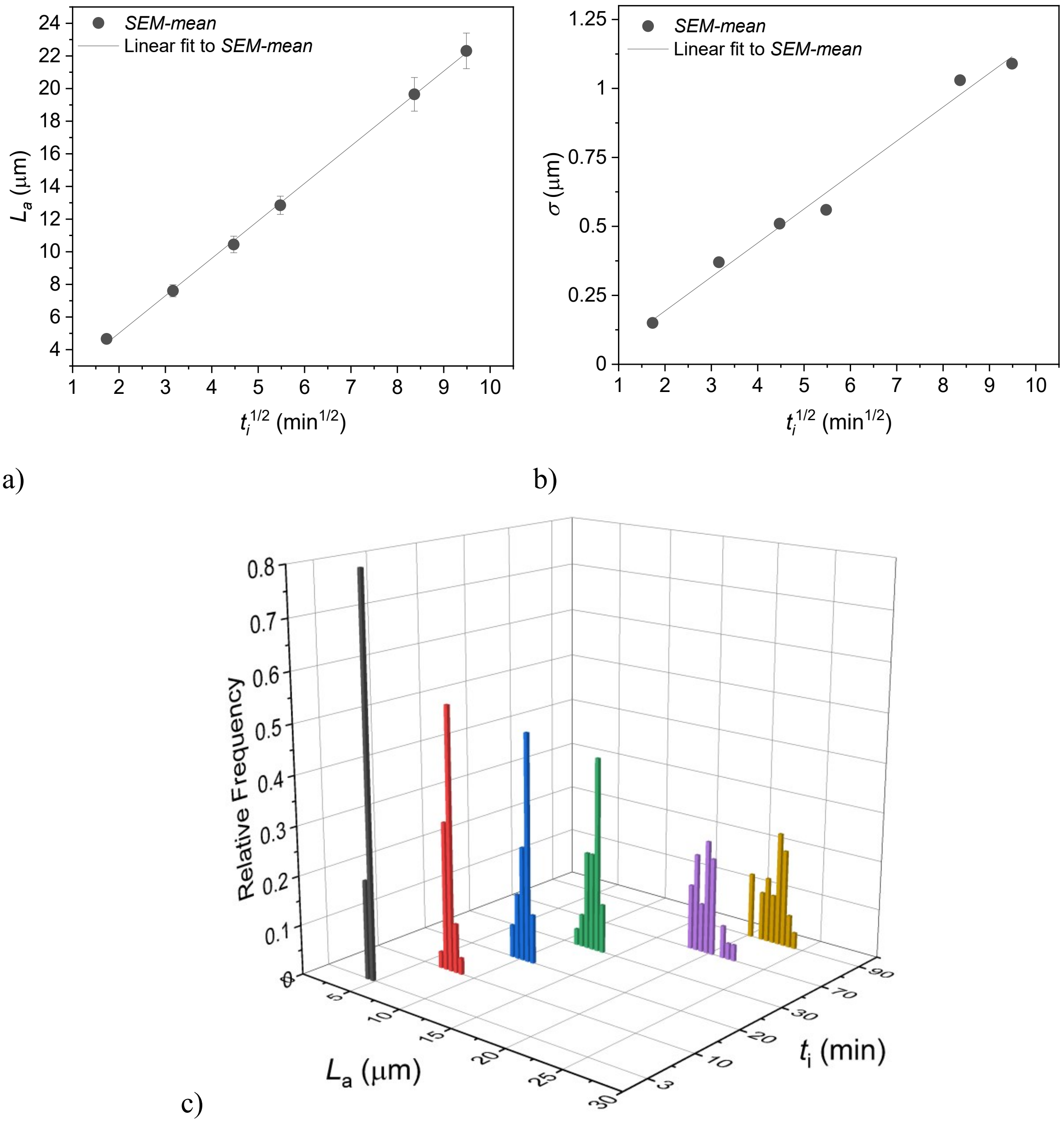

Figure 4.27. a) Average imbibition lengths $L_a(t_i)$ for AAO plotted against the square root $t_i^{1/2}$ of the imbibition time t_i obtained from manual evaluation of SEM images. The error bars correspond to the standard deviation. b) Standard deviations $\sigma(t_i)$ as measures of the imbibition front width plotted against the square root $t_i^{1/2}$ of the imbibition time t_i obtained from manual evaluation of SEM images. c) Histograms displaying the relative frequency of the single-pore imbibition length L_s (bin size ΔL_s = 0.5 µm) for different infiltration times t_i obtained from manual evaluation of SEM images. The solid lines in a) and b) are fits to L_a plotted against the square root $t_i^{1/2}$ of the imbibition time t_i obtained by linear regression.

4.5.2 Evaluation of imbibition lengths, and determination of imbibition front width descriptors of CPG samples

Three CPG membranes for each specific infiltration time $t_{i,}$ were infiltrated under the same conditions. Then, the single-location imbibition lengths L_s were determined in a similar way than the single-pore imbibition lengths for AAO. The single-location imbibition lengths L_s (red vertical lines in **Figure 4.28b)**, were measured from the green line in **Figure 4.28b** to the menisci (blue arrows in **Figure 4.28a**) and were determined for 10 locations per CPG membrane using the software ImageJ.[124] Thus, overall 30 CPG locations of three CPG membranes were evaluated for each t_i value. In contrast to AAO, which consist of straight cylindrical pores, for CPG it is not possible to single out individual pores from SEM images because CPG consists of a highly interconnected 3D network of pores. **Figure 4.29** shows representative cross-sectional SEM images of CPG membranes infiltrated with PS at 200°C a) for 3 minutes, b) for 10 minutes, c) for 20 minutes, d) for 30 minutes, e) 70 minutes and f) for 90 minutes obtained with a SESI detector.

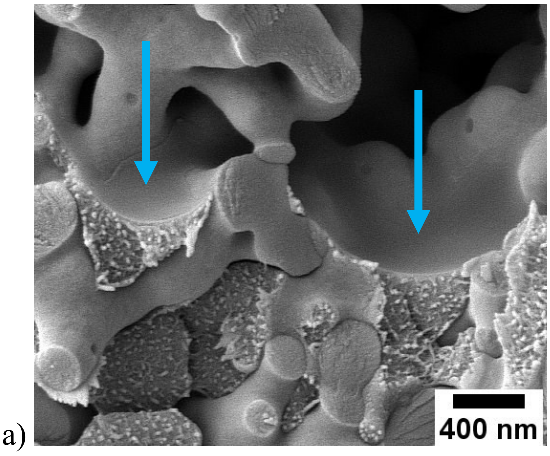

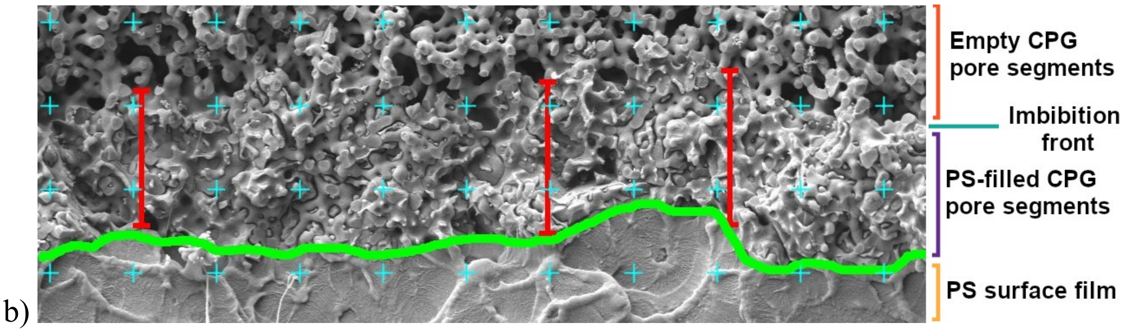

Figure 4.28. a) SEM image of a CPG membrane infiltrated with PS with M_w: 24.7 kg/mol at 140°C for 10 minutes, cleaved normal to the CPG surface showing the cross-section of menisci (blue arrows). PS with M_w: 24.7 kg/mol was exclusively used here to obtain the detail of the menisci due to a more brittle characteristic allowing the PS segment cross-section to be visible. b) SEM image of a CPG membrane infiltrated with PS with M_w: 239 kg/mol at 200°C for 10 minutes. At the bottom, a bulk PS film covering the CPG surface is seen. The green line marks the CPG surface. Above the green line in the center of the micrograph, PS-filled CPG pore segments and at the top empty CPG pore segments are seen. The grid marked by blue crosses helped align the CPG surface horizontally. The red lines indicate single-location imbibition lengths L_s.

The SEM image displayed in **Figure 4.28** of a CPG membrane shows the relevant features of a PS-infiltrated CPG membrane. At the bottom, a bulk PS film located on the CPG surface is seen as a homogeneous grey area. The green line marks the CPG surface. Above the green line in the center of the micrograph, PS-filled CPG pore segments. At the top, empty CPG pore segments are seen.

The average imbibition lengths L_a shown in **Figure 4.30a** were then calculated as the arithmetic mean value of the L_s values and fitted with a linear function. The standard deviation σ, shown in **Figure 4.30b** of the L_s histograms (**Figure 4.30c**) was employed as measure of the imbibition front width.

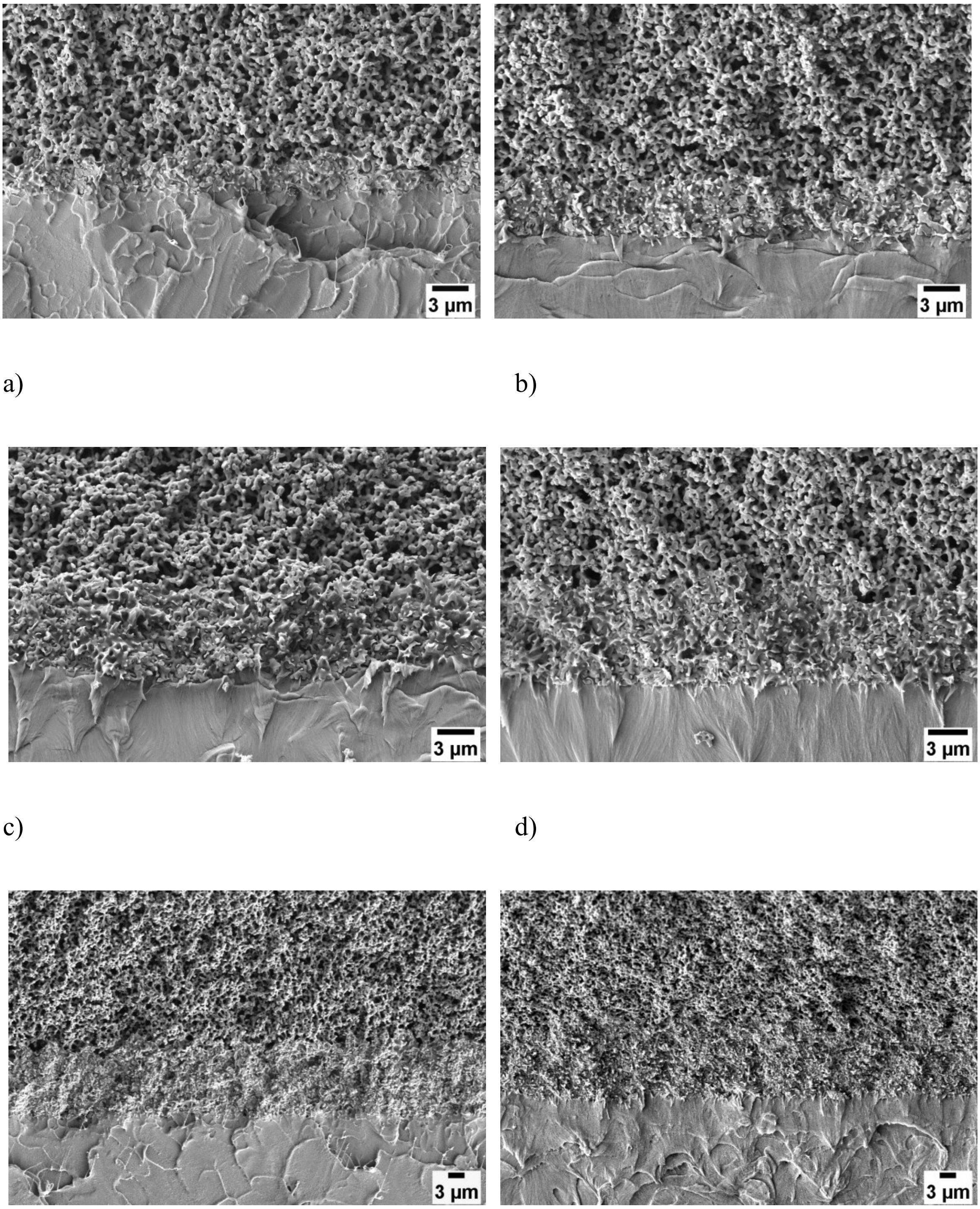

a) b)

c) d)

e) f)

Figure 4.29. SEM cross-sectional images of CPG membranes infiltrated with PS at 200°C a) for 3 minutes, b) for 10 minutes, c) for 20 minutes, d) for 30 minutes, e) 70 minutes and f) for 90 minutes. All images were obtained with a SESI detector.

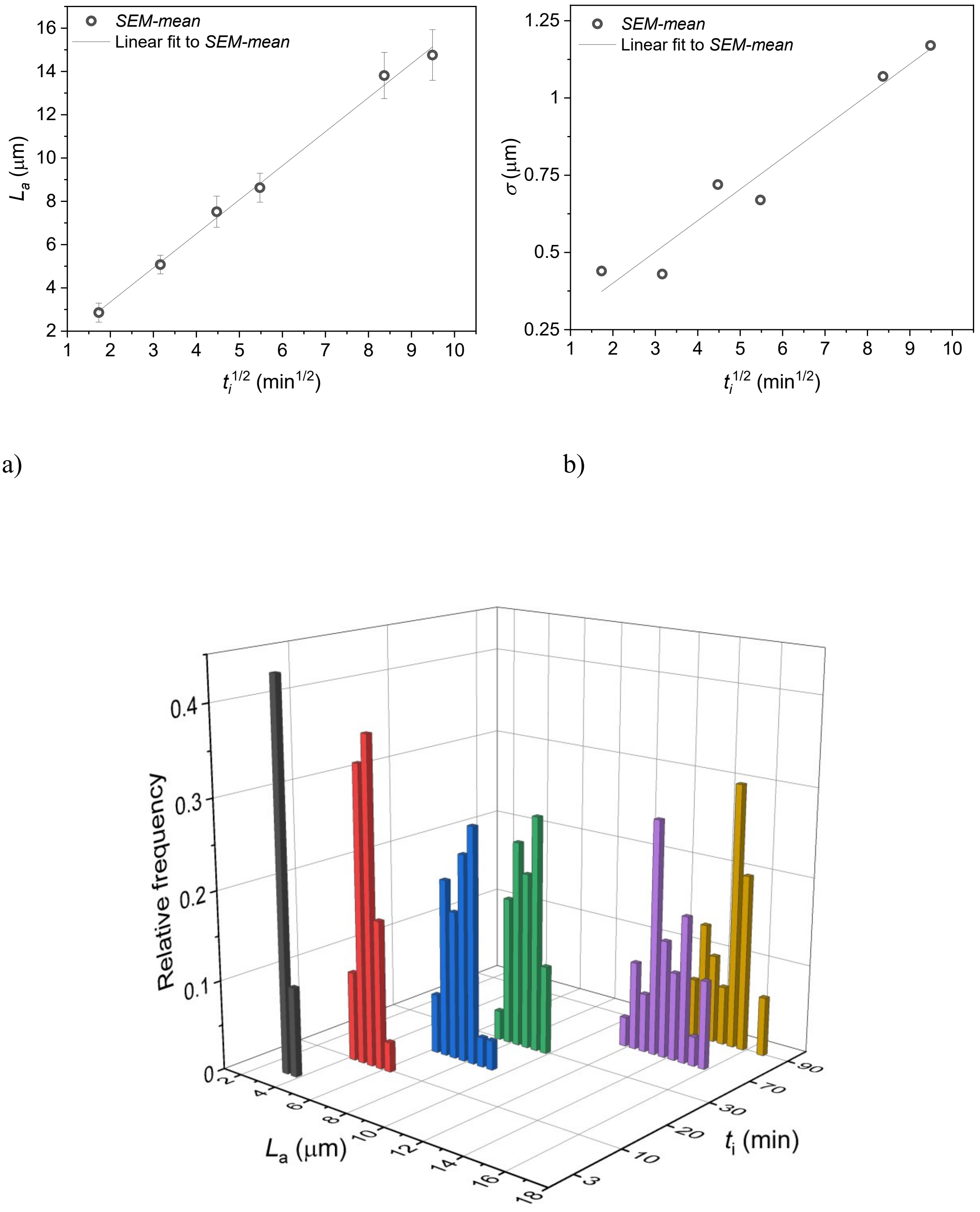

a)

b)

c)

Figure 4.30. a) Average imbibition lengths $L_a(t_i)$ for CPG plotted against the square root $t_i^{1/2}$ of the imbibition time t_i obtained with method *SEM-mean*. The error bars correspond to the standard deviation. b) Standard deviations $\sigma(t_i)$ as measures of the imbibition front width plotted against the square root $t_i^{1/2}$ of the imbibition time t_i obtained with method *SEM-mean*. c) Histograms displaying the relative frequency of the single-pore imbibition length L_s (bin size $\Delta L_s = 0.5$ µm) for different infiltration times t_i obtained by method *SEM-mean*. The solid lines in a) and b) are fits to $L_a(t_i)$ plotted against the square root $t_i^{1/2}$ of the imbibition time t_i obtained by linear regression.

4.6 Calculation of Imbibition Length Frequency Densities from Pore Size Distributions

4.6.1 Estimation of imbibition length frequency densities from a pore diameter histogram of AAO obtained from a SEM image

Single-pore imbibition lengths L_s were calculated based on an AAO pore diameter histogram obtained by the evaluation of a SEM image and the application of a Lucas-Washburn model modified by Yao et al.[17] to consider the presence of a dead layer consisting of PS molecules that are immobilized due to strong attractions on the AAO pore walls which results in a higher effective viscosity and therefore slower imbibition.

First, the determination of AAO pore diameters by evaluation of a SEM image was done in the following manner. An 8-bit grayscale scanning electron microscopy (SEM) image of the surface of an AAO membrane with a nominal pore diameter of 400 nm and a pore depth of 1 µm was taken with a Zeiss Auriga device at 3 kV acceleration voltage and with 8 mm working distance. The SEM image acquired with an in-lens detector extended 2048 pixels x 1350 pixels (**Figure 4.31a**) and showed an image field of 87.52 µm x 57.69 µm (23.4 pixels/µm). The pore diameters were determined using the software ImageJ.[124] Brightness and contrast values were adjusted by setting the minimum pixel intensity value to 90 and the maximum to 216 on a pixel intensity scale ranging from 0 to 255, which correspond to an image depth of 8 bits. In this way, the apparent pore areas did not change when brightness and contrast were modified. The "Make binary" function was used to generate a binary image. Then, the "Analyze particles" function was used to determine the diameters of 19135 evaluated AAO pores. AAO pores touching the edges of the SEM image were not considered. A detail extending 400 pixels x 400 pixels and the outlines of the detected pores of the evaluated SEM image from the sample are shown in **Figure 4.32b, c.** A mean AAO pore diameter of 384 nm ± 22 nm, corresponding to a pore radius b_0 of 192 nm ± 11 nm was obtained, as shown in **Figure 4.32a**

Then, the estimation of the thickness of the dead layer was done as follows, first the bulk viscosity $\eta_0 = 3.5 \cdot 10^4$ Pa · s of PS with a molecular mass M_w = 123 kg/mol determined for a temperature of 170 °C by Kim et al.[131] was used as reference value. The viscosity for the molecular mass was corrected using a power law suggested by Berry and Fox (Equation 4.8) assuming an exponent of 3.4:[132]

$$\eta_0 \propto M^{3,4} \rightarrow \left(\frac{M_1}{M_2}\right)^{3,4} = \frac{\eta_{0,1}}{\eta_{0,2}} \qquad \text{(Equation 4.8)}$$

To correct for the temperature T, the Williams-Landel-Ferry (WLF) equation (Equation 4.9) was used.[133] The viscosity η_g at the glass transition temperature T_g of PS was first calculated assuming T_g = 273 K using WLF parameters C_1 = 17.44 and C_2 = 51.6 K.[133] Then, the bulk viscosity $\eta_0 = 1.15 \cdot 10^4$ Pa · s of the PS used in this work at 200°C was calculated also using Equation 4.9.

$$\log\left(\frac{\eta_0(T)}{\eta_{0,g}}\right) = -\frac{C_1(T-T_g)}{C_2+T-T_g} \qquad \text{(Equation 4.9)}$$

Yao et al.[17] defined an effective radius b_{eff} for cylindrical pores filled with polymers that is the difference of the nominal pore radius b_0 and the thickness Δb of the dead layer formed by molecules immobilized on the pore walls (Equation 4.10):

$$b_{eff} = b_0 - \Delta b \qquad \text{(Equation 4.10)}$$

The presence of a dead layer can then be considered by modifying the Lucas-Washburn equation as follows (Equation 4.11):

$$L_s = \sqrt{\frac{b_{\mathrm{eff}}^4 \gamma \cos\theta}{2\eta_0 b_0^3}}\sqrt{t_i} \qquad \text{(Equation 4.11)}$$

L_s is the single-pore imbibition length, t_i the elapsed imbibition time, γ the surface tension of PS and θ the equilibrium contact angle of PS on the AAO pore walls. To calculate Δb, the first square root of Equation 4.11 was equated with the imbibition prefactors ν determined by methods *CT-mean* (cf. 4.2.3) and *CT-rms* (cf. 4.2.3) with Equation 4.12:

$$\nu = \sqrt{\frac{b_{\mathrm{eff}}^4 \gamma \cos\theta}{2\eta_0 b_0^3}} \qquad \text{(Equation 4.12)}$$

The mean value $b_0 = 192$ nm obtained by the evaluation of a SEM image described above was inserted in Equation 4.12. For γ a value of 29 mJ/m^2 and for cos θ a value of 1 were assumed.[134] In this way, the value of b_{eff} can be calculated. For both methods *CT-mean* and *CT-rms* the thickness of the dead layer was calculated, which in this case amounted to $\Delta b \approx 40$ nm.

Finally, since the AAO pore diameters are known, the single-pore imbibition lengths L_s could be calculated by inserting the radii b_0 determined for single AAO pores by the evaluation of a SEM image, as described above, into Equation 4.11. L_s frequency densities were then obtained. The average imbibition lengths L_a (**Figure 4.32b)** were calculated as mean values of the sets of L_s values ("*Calc-AAO-*L_a") as well as the standard deviations σ of L_s (error bars in **Figure 4.32b**) for the different imbibition times t_i ("*Calc-AAO-WD*").

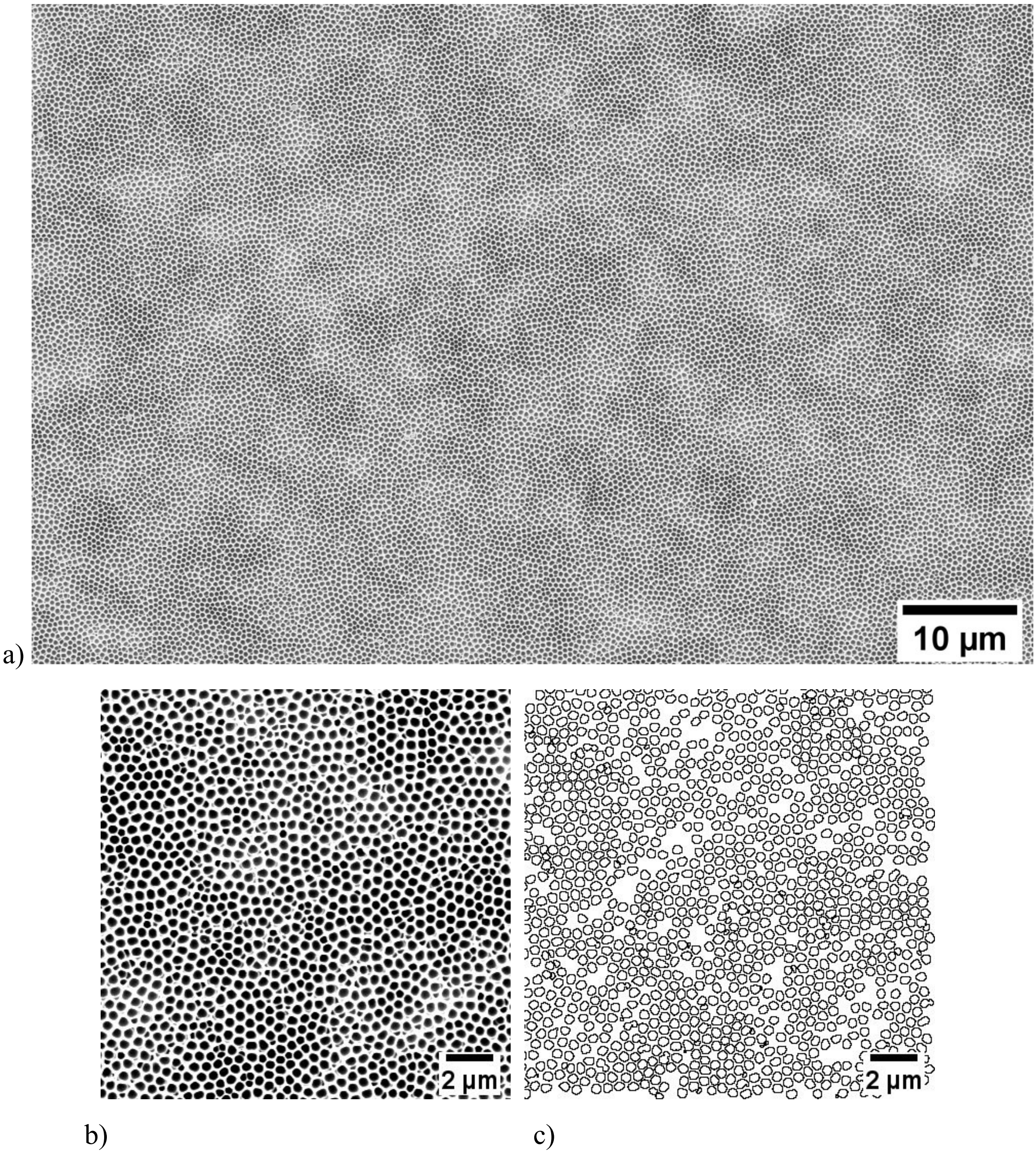

Figure 4.31. a) SEM image extending 2048 pixels x 1350 pixels and showing an image field of 87.52 µm x 57.69 µm (23.4 pixels/µm) acquired with 1290fold magnification by using an InLens detector. b) Detail extending 400 pixels x 400 pixels of the original SEM image used for the determination of the mean pore diameter of AAO. c) Detected outlines with ImageJ of the evaluated pores from b).

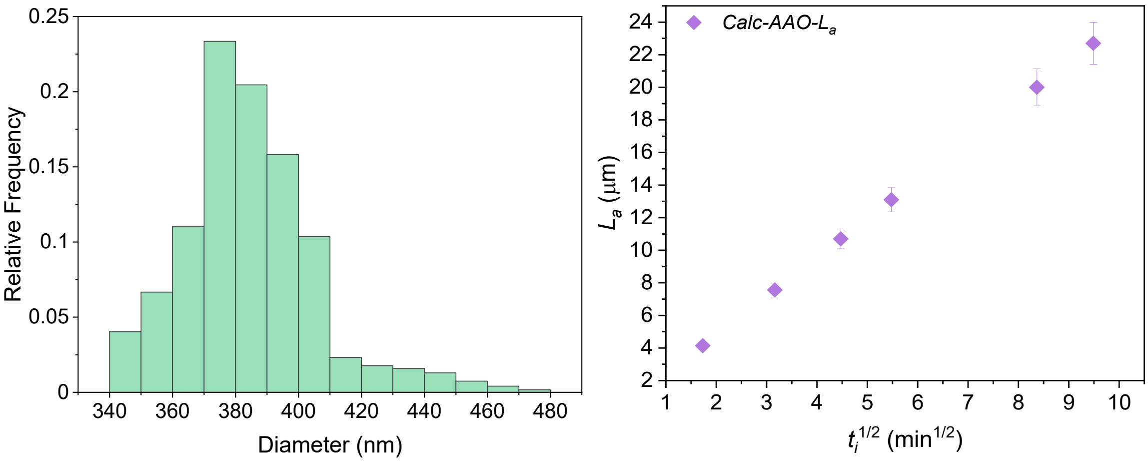

a) b)

Figure 4.32. a) AAO pore diameter histogram obtained by the evaluation of a SEM image in **Figure 4.31a**. The pore depth of the investigated membrane amounted to 1 µm. The bin size of 10 nm was exclusively used for this visualization. b) Calculated L_a and σ (error bars) from the b_0 determined from the SEM image and the calculated v.

4.6.2. Estimation of imbibition length frequency densities in CPG from Mercury Intrusion Measurements

As stated in Section 3.1, the CPG membranes were characterized by mercury intrusion. To obtain a pore diameter histogram, the applied pressure is gradually increased, which causes gradual intrusion of mercury into the probed pore system. The relation between the applied pressure and the diameter of the pore segments filled at the applied pressure is inverse. The pore diameter is calculated by the Washburn equation using a mercury surface tension of 0.484 N/m and a mercury contact angle of 141.3°. The intruded incremental volume of mercury associated with an individual pressure step is the difference between the cumulative intrusion volumes after and prior to the application of the pressure step. The relative incremental pore volume ascribed to a pore diameter increment is the corresponding proportion of the total pore volume, which is the cumulative volume of mercury intruded into the probed pore structure at maximum pressure. Pore diameter histograms are obtained by plotting relative incremental intrusion volumes against the medium values of the corresponding pore diameter intervals. Porosities and specific pore volumes are calculated using the total pore volume. For the CPG membranes used here, a pore diameter ≈ 380 nm, 58 % porosity and a specific pore volume of 0.628 $\mathrm{cm^3/g}$ were obtained.

To consider "dead layers" of adsorbed PS molecules on the pore walls,[14-17] an effective pore radius b_{eff} was introduced by Yao et al.,[17] which is obtained by subtracting the thickness Δb of the dead layer from the geometric pore radius b_0 (Equation 4.10)

For isotropic spongy-continuous pore networks, such as the pore networks of CPGs, the situation is more complex as in the case of AAO (cf. Section 4.5.1). It is reasonable to assume that only a certain proportion of the pores close to the imbibition front exhibits a pressure gradient caused by the presence of a meniscus so that only this proportion of the pore contributes to the flow of the invading fluid. Gruener et al. suggested to consider this aspect by dividing the flow rate by a hydrodynamic tortuosity τ_h.[95] For isotropic spongy-continuous pore systems, the expression for the preexponential factor ν of the Lucas-Washburn law is, therefore, modified as follows:

$$\nu = \sqrt{\frac{b_{\mathrm{eff}}^4 \gamma \cos\theta}{2\eta_0 b_0^3 \tau_h}} = \sqrt{\frac{b_{\mathrm{eff}}^4}{\tau_h}} \cdot \sqrt{\frac{\gamma \cos\theta}{2\eta_0 b_0^3}} \qquad \text{(Equation 4.13)}$$

Besides b_0, the quantities in the second square root $\sqrt{\frac{\gamma \cos\theta}{2\eta_0 b_0^3}}$ are known from literature (cf. Section 4.5.1) The mean pore radius b_0 of CPG was obtained from mercury intrusion data (**Figure 4.33a**). The prefactor ν of the Lucas-Washburn law was experimentally determined from the slopes $\mathrm{d}L_a/\mathrm{d}t_i^{1/2}$ of the linear fits to the sets of $L_a(t_i^{1/2})$ data points obtained by method *Batch-CT-rms*. While b_{eff} and τ_h cannot be determined independently, Equation (4.13) can easily be resolved for $\sqrt{b_{\mathrm{eff}}^4/\tau_h}$ so that the value of this square root can be calculated. Thus, $\sqrt{b_{\mathrm{eff}}^4/\tau_h} \approx 14699\ \mathrm{nm}^2$ was obtained.

Equation (4.13) relates the mean pore radius b_0 of the pore model used, which is typically accessible by independent experimental methods such as mercury intrusion, to the prefactor ν of the Lucas-Washburn law. As apparent from **Figure 4.33a**, mercury intrusion experiments do not only yield a mean pore radius b_0 for the CPG membranes but also the underlying pore radius frequency density. A relative frequency of occurrence $f_{p,g}$, here as relative volume fraction, is assigned to pore segments with radii falling into a pore radius increment centering about a central pore radius value b_g. Thus, pseudo-single-pore imbibition lengths $L_s(b_g,t_i)$ can be calculated for each b_g value and each imbibition time t_i by replacing the mean pore diameter b_0 in equation (4.13) by b_g:

$$L_{s,g}(b_g,t_i) = \sqrt{\frac{b_{eff}^4}{\tau_h}} \cdot \sqrt{\frac{\gamma\cos\theta}{2\eta_0 b_g^3}} \cdot \sqrt{t_i} \qquad \text{(Equation 4.14)}$$

The overall number of considered b_j values and, therefore, of $f_{p,g}\,(b_g)$ data points is z so that $1 \le j \le z$. It should be noted that in Equation (4.14) the constant value of 14699 nm^2 is used for the square root $\sqrt{b_{eff}^4/\tau_h}$. This is a simplification because, in Equation (4.14), b_{eff} depends on b_{g} rather than on b_0. Summation of the $L_s(b_g)$ values obtained for a specific imbibition time t_i according to Equation (4.14) weighed with the relative frequency $f_{p,g}$ displayed in the CPG pore diameter histogram shown in **Figure 4.33a** yields then the average imbibition length L_a (**Figure 4.33b**) for the respective t_i value (Equation 4.15).

$$L_a(t_i) = \sum_{g=1}^{z}\left(f_{p,g} \cdot L_{s,g}\right) = \sum_{g=1}^{z}\left(f_{p,g} \cdot \sqrt{\frac{b_{eff}^4}{\tau_h}} \cdot \sqrt{\frac{\gamma\cos\theta}{2\eta_0 b_g^3}} \cdot \sqrt{t_i}\right) \qquad \text{(Equation 4.15)}$$

Equation (4.15) does not represent an independent approach to the determination of imbibition front positions but rather a cross-check for additional validation.

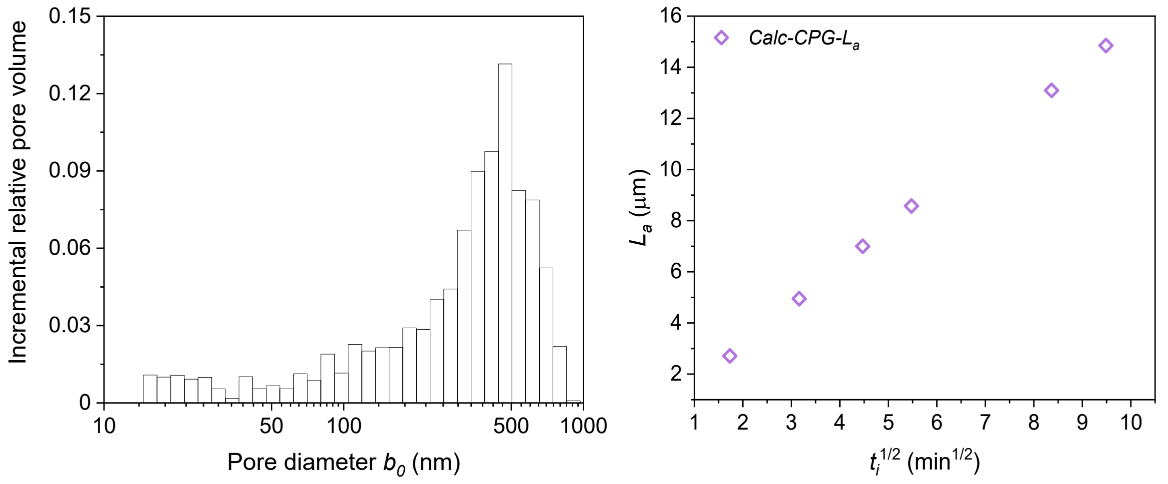

a)

b)

Figure 4.33. a) Pore diameter histogram of CPG membranes derived from a mercury intrusion measurement. showing the portion of the relative pore volume occupied by pore segments with a diameter falling in a pore diameter increment centering about a pore diameter value b_j. The thickness of the investigated membrane amounted to 490 ± 10 µm. b) Average imbibition lengths $L_a(t_i)$ in CPG membranes with results of equation (4.14) using a CPG pore size distribution obtained from a).

Equation (4.13) was used to estimate how variations in the assumed mean CPG pore diameter $2 \cdot b_0$ impact the tortuosity apparent from the comparison of PS infiltration into CPG and AAO as a reference pore model. To this end, the $L_a(t_i)$ profiles assuming values of 150 nm, 170 nm, 190 nm, 210 nm, 230 nm and 250 nm for the CPG pore radius b_0 were calculated according to:

$$L_a(t_i) = \sqrt{\frac{b_{eff}^4}{\tau_h}} \cdot \sqrt{\frac{\gamma \cos\theta}{2\eta_0 b_0^3}} \cdot \sqrt{t_i} \qquad \text{(Equation 4.16)}$$

and determined for each b_0 value the slope $\nu_{\mathrm{CPG}}(b_0)$ of linear fits to the corresponding sets of $L_a(t_i)$ data points corresponding to the Lucas-Washburn prefactors. To estimate the tortuosities $2.280/\nu(b_0)$ apparent from imbibition dynamics, the slope $\nu_{\mathrm{AAO}} = 2.280$ µm/min$^{1/2}$ experimentally obtained for AAO by method *Batch-CT-rms* (cf. Section 4.3.4 and **Table 5.1**) was divided by the slopes $\nu_{\mathrm{CPG}}(b_0)$ and the resulting apparent tortuosities against the CPG mean pore diameter $2 \cdot b_0$ was plotted. The tortuosity changes by 0.25 if the pore diameter $2b_0$ changes by 10 % (**Figure 4.34**).

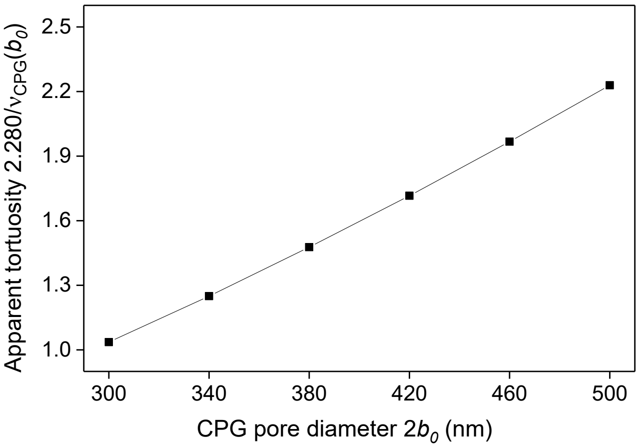

Figure 4.34. Apparent tortuosities $2.280/\nu_{CPG}(b_0)$ apparent from the comparison of the imbibition of PS into CPG and into AAO as a reference pore model, which were calculated using Equation (4.16), plotted against the CPG pore diameter $2b_0$.

5 Discussion

5.1 Imbibition in Isolated Straight Cylindrical AAO Pores

5.1.1 Average imbibition front positions

Real-space monitoring of the imbibition of PS into AAO by phase-contrast X-ray computed tomography with single pore resolution enables the evaluation of large numbers of AAO pores (here at least 1304) as well as the identification of menisci in the individual pores and directly yields frequency distributions of the single-pore imbibition lengths L_s. The number of AAO pores considered when cross-sectional SEM images or EDX maps are evaluated (methods *SEM-mean, EDX-rms*; cf. **Table 5.1**) is typically at least one order of magnitude lower. Moreover, the algorithmic semi-automated analysis of volumetric sample reconstructions obtained by phase-contrast X-ray CT ensures unbiased identification of AAO pores in the probed sample volume. The results obtained by method *SEM-mean* involving the manual determination of single-pore imbibition lengths L_s may be biased because of an implicit tendency to preferentially pick "good" AAO pores for evaluation.

It is commonly assumed that imbibition lengths, be it the single-pore imbibition length L_s or the average imbibition length L_a, scale with $t_i^{1/2}$, as predicted by the classical Lucas-Washburn theory. Indeed, at first glance all tested approaches seem to corroborate this notion. Plotting $L_a(t_i)$ against $t_i^{1/2}$ (**Figure 5.1a** and **Table 5.1**) seems to yield linear $L_a(t_i^{1/2})$ profiles and similar numerical values for the imbibition prefactor ν (cf. Equation 1.1), which corresponds to the slope of the linear fits to the different sets of $L_a(t_i)$ data points. A measure of the linearity of this correlation is the Pearson correlation coefficient *r*.[135] The closer *r* to 1 is, the better is the linearity. In this way, it can be evaluated from a statistical point of view which exponent *n* of t_i yields the best description of the experimental results. This statistical evaluation reflects not only the physics underlying the probed imbibition process but also the quality of the measured data and the procedures for their evaluation. Hence, *r* as a function of *n* was plotted for the linear fits to the $L_a(t_i)$ data sets for exponents *n* to t_i ranging from 0.1 to 1.0 obtained by methods *CT-mean*, *CT-rms*, *EDX-rms* and *Batch-CT-rms* (**Figure 5.1b**) to find out if a value of 1/2 of the exponent *n* of t_i, which corresponds to the classical Lucas-Washburn theory, yields the best linear correlation between L_a and t_i^n. For method *CT-rms*, the best linear correlation between L_a and $t_i^n$was obtained for $n = 0.45$. For method *CT-mean*, the best linear correlation between L_a and $t_i^n$was obtained for $n = 0.40$. For method *EDX-rms*, the best linear correlation between L_a and $t_i^n$was obtained for $n = 0.35$. For method *Batch-CT-rms*, the best linear correlation between L_a and $t_i^n$was obtained for $n = 0.45$. The average *n* value for the best linear correlation across methods is ≈ 0.41. The slopes dL_a/dt_i^n of the linear fits to the sets of $L_a(t_i^n)$ data points obtained by methods *CT-mean*, *CT-rms*, *EDX-rms* and *Batch-CT-rms* represent the imbibition prefactor ν of the power law describing the relation between imbibition length and imbibition time. As obvious from **Figure 5.1c**, the slopes $dL_a/dt_i^n(n)$ for exponents *n* ranging from 0.1 to 1.0 obtained by methods *CT-mean*, *CT-rms*, *EDX-rms* and *Batch-CT-rms* nearly perfectly coincide. However, reducing the value of the exponent *n* from 0.5 to 0.35 resulted in a change in the apparent imbibition speed from ≈ 2.4 µm/min^n to ≈ 5.5 µm/min^n for both methods *CT-mean* and *CT-rms,* from ≈ 2.1 µm/min^n to ≈ 5 µm/min^n for method *EDX-rms* and from ≈ 2.3 µm/min^n to ≈ 5.3 µm/min^n for method *Batch-CT-rms*. On average, there is a reduction of ≈ 3 µm/min^n between methods by reducing the value of the exponent *n* from

0.5 to 0.35. It is assumed that methods CT-rms and *Batch-CT-rms* yields more valid results because much larger sample volumes are probed and preparation artifacts are prevented that may occur when infiltrated membranes are cleaved to prepare cross-sectional specimens for the EDX mappings.

The classical Lucas-Washburn theory does not account for the tendency of macromolecules, such as PS, to form interphases with reduced molecular mobility at substrate surfaces.[136] Indeed, the existence of so-called "dead zones" consisting of molecules of pore-invading polymers immobilized on the pore walls (**Figure 2.14**) was reported previously.[45] Notably, the estimated thickness Δb of the dead layers exceeded the radii of gyration of the invading polymer species several times. Yao et al. thus modified the classical Lucas-Washburn model considering the occurrence of dead layers by the introduction of a reduced effective pore radius b_{eff} and an increased effective fluid viscosity η_{eff} (Equation 4.3).[17] Using an average AAO pore radius b_0 = 192 nm obtained by evaluation of a SEM image of the surface of an AAO membrane (**Figure 4.32a**), the expression for the imbibition prefactor resulting from the modified imbibition model with the slopes $dL_a/dt_i^{1/2}$ of the linear fits to the sets of $L_a\left(t_i^{1/2}\right)$ data points obtained by methods *CT-mean* and *CT-rms* was equated. The results indicate the presence of a PS dead layer with a thickness $\Delta b \approx 40$ nm on the AAO pore walls. Using this value and the single pore diameter values determined by the previously mentioned evaluation of a SEM image (cf. Section 4.5.1), the modified Lucas-Washburn model to calculate single-pore imbibition lengths L_s was applied for each AAO pore. The average values L_a obtained from the L_s frequency density for the different imbibition times t_i ("*Calc-AAO-L_a*" data points **Figure 4.32b** and **Figure 5.1a**) are in excellent agreement with the experimental values obtained by methods *CT-mean*, *CT-rms*, *SEM-mean*, *EDX-rms* and *Batch-CT-rms*. This outcome is remarkable considering that the metrological precision of scanning electron microscopy is limited and that the values for the PS melt viscosity and the PS surface tension were approximated.

It would also be straightforward to calculate AAO pore diameters from the single-pore imbibition lengths L_s, if the classical Lucas-Washburn law was valid. However, the simple derivation of a pore diameter frequency density from an imbibition length frequency density is no longer possible if dead layers of PS molecules immobilized on the AAO pore walls are present. The equations resulting from the modified Lucas-Washburn model devised by Yao et al. can no longer be solved for the AAO pore diameter.

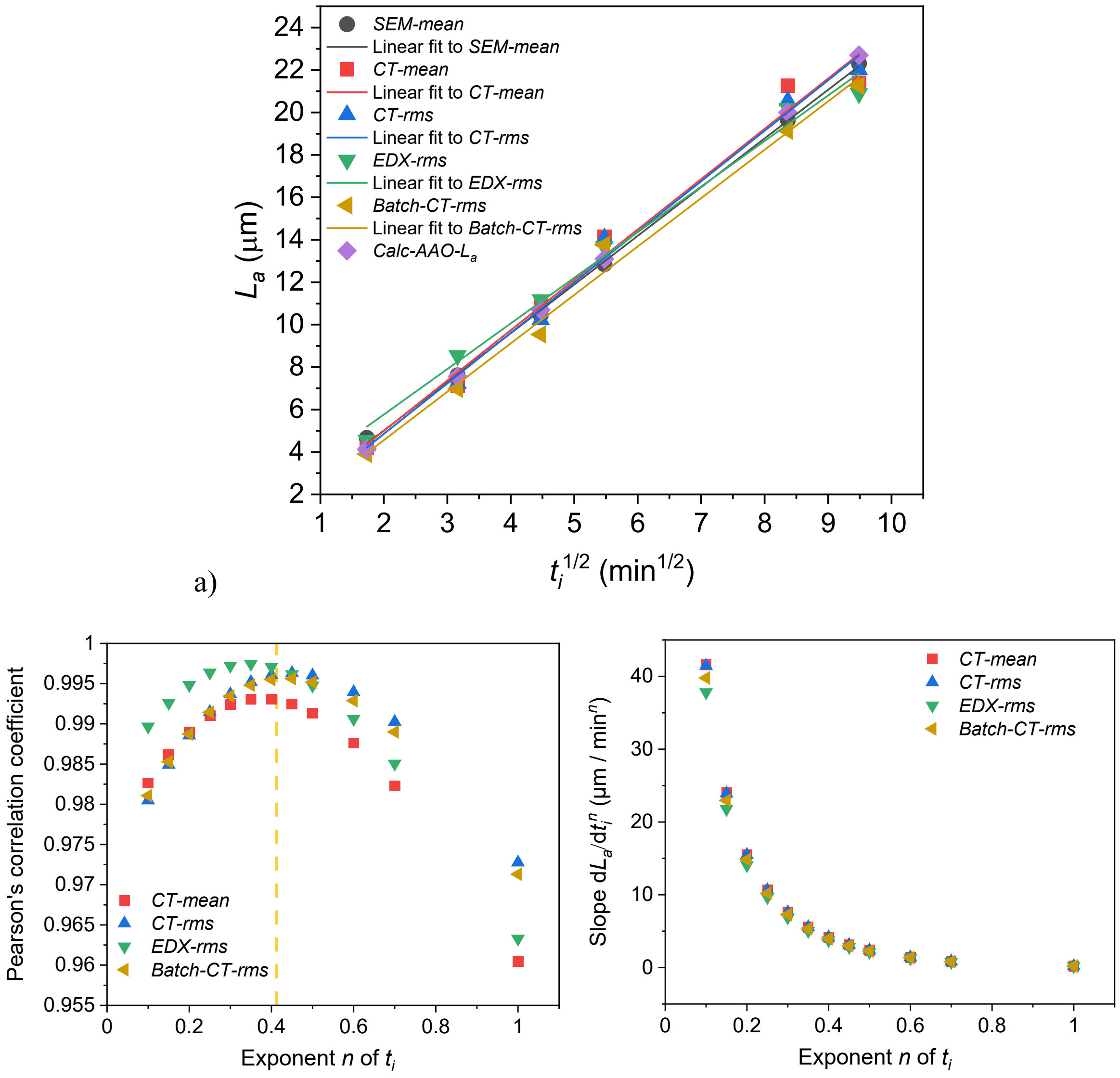

a)

b)

c)

Figure 5.1. Comparison of the average imbibition lengths $L_a(t_i)$. a) Sets of $L_a(t_i)$ data points obtained by methods *SEM-mean* (black circles), *CT-mean* (red squares), *CT-rms* (blue up-triangles), *EDX-rms* (green down-triangles) and *Batch-CT-rms* (ochre left-pointing triangles) as well as linear fits to the sets of data points plotted against the square root $t_i^{1/2}$ of the imbibition time t_i. For comparison, data points obtained by the evaluation of a SEM image of AAO and application of the modified Lucas-Washburn model devised by Yao et al.[17] are shown ("*Calc-AAO-L_a*", purple diamonds). b) Pearson correlation coefficients of linear fits to sets of $L_a(t_i^n)$ data points obtained by methods *CT-mean, CT-rms, EDX-rms* and *Batch-CT-rms* for exponents n of t_i ranging from 0.1 to 1.0. The dashed yellow line at $n \approx 0.41$, indicates the average n value at which r of each method is closer to 1. c) Slopes dL_a/dt_i^n of linear fits to sets of $L_a(t_i^n)$ data points obtained by methods *CT-mean, CT-rms, EDX-rms* and *Batch-CT-rms* for exponents n ranging from 0.1 to 1.0 plotted against n.

5.1.2 Imbibition front widths

The comparison of experimentally obtained measures for average imbibition lengths L_a and imbibition front widths with predictions by theoretical models is far from being trivial. A first problem is the interpretation of experimental results. Even imbibition into straight cylindrical pores comes along with a complex phenomenology of transient imbibition states, including the presence of precursor films ahead of the imbibition front and voids in (**Figure 2.13**) infiltrated pore segments behind the imbibition front.[20] Hence, there might be no "natural" absolute measures for the onsets, the positions and the widths of imbibition fronts. Moreover, quite different physical effects can be exploited for the imaging of imbibition fronts, and quite different statistical evaluation methods and measures can be used for the quantification of L_a and the imbibition front widths. Depending on the applied methodology, different numerical values may be obtained.

The spatiotemporal evolution of the imbibition front width in the course of imbibition processes reveals morphological properties of the pore system being imbibed. Continuum-hydrodynamical concepts suggest that the single-pore imbibition prefactor ν (cf. Equation 1.1) depends on the balance of the flow-driving Laplace pressure and the pressure-drop caused by the viscous drag in the PS melt imbibing the AAO pores.[13] As a result of the distinct dependencies of these contributions on the AAO pore diameters, the Lucas-Washburn kinetics for the advancement of the imbibition front is thus naturally transmitted into the broadening kinetics of the latter. The imbibition front width and measures thereof scale with a power function t_i^n of the imbibition time t_i. The slope $d\sigma/dt_i^n$ of linear fits to sets of $\sigma(t_i)$ data points represents the scaling of the imbibition front width with the imbibition time t_i. The exponent n reveals morphological properties of the pore system being imbibed. For a set of parallel pores with a random pore diameter distribution but uniform diameters along the individual pores the dispersion of the single-pore imbibition lengths L_s scales with $t_i^{1/2}$.[41, 49] By contrast, for spontaneous imbibition into an ensemble of independent pores characterized by random diameter variations along the individual pores the imbibition front widening scales with $t_i^{1/4}$, as exactly derived by Gruener et al.[41]

Discussion

The direct algorithmic quantification of imbibition front widths is challenging. Methods *CT-mean*, *CT-rms, EDX-rms,* and *Batch-CT-rms* yield raw curves of quantities accessible by evaluation of microscopic raw data, in which the positions of the AAO surface and the imbibition front are indicated by peaks or steps. Statistical dispersion measures, such as standard deviations σ, or parameters from curve fitting with adequate mathematical models, such as the slope factor k from Boltzmann step function allow the quantification of the widths of the peaks or steepness of the steps indicating the positions of the imbibition front and, indirectly, the quantification of the imbibition front width, the chosen statistical descriptors are hereafter referred to as "width descriptors" *WD*. However, the average imbibition length L_a for the samples studied here amounts to a few µm up to several 10 µm, whereas the length scales relevant to the quantification of the imbibition front widths are one order of magnitude smaller and range from a few 100 nm up to a few µm. Therefore, the applied imaging method and the applied statistical data evaluation algorithm impact the quantification of the imbibition front widths more sensitively than the determination of L_a. Assuming that the pore diameter along the AAO pores is uniform, whereas AAO pore arrays are characterized by a certain pore diameter dispersion, σ against $t_i^{1/2}$ was plotted and linear fits added to the different sets of $WD\left(t_i^{1/2}\right)$ data points (**Figure 5.2a** and **Table 5.1**). For comparison, the standard deviations $\sigma\left(t_i^{1/2}\right)$ of sets of L_s values (*"Calc-AAO-σ")* from the AAO pore diameters extracted from a SEM image were calculated (cf. Section 4.5.1) using the modified Lucas-Washburn model reported by Yao et al.[17] The results obtained in this way are in reasonable agreement with the experimental results obtained by methods *CT-mean*, *SEM-mean, CT-rms, EDX-rms* as well as *Batch-CT-rms* and corroborate the notion that a dead layer is present when PS is infiltrated into AAO.

In analogy to the statistical evaluation of the power laws describing the dependence of L_a on t_i (cf. Section 5.1.1), which exponent n of t_i yields the best description of the experimental results was tested by plotting the Pearson correlation coefficient *r* of the linear fits to the *WD*(t_i) data sets obtained by methods *CT-mean, CT-rms, EDX-rms,* and *Batch-CT-rms* against the exponent *n* (**Figure 5.2b**). The obtained *r*(*n*) profiles are vertically shifted and reveal that the best linear correlation is obtained for n = 0.60 in the case of method *CT-mean*, for n = 0.45 in the case of method *CT-rms*, for n = 0.15 in the case of method *EDX-rms* and for n = 0.45 in the case of method *Batch-CT-rms,* whereas the *r*(*n*) values drop for smaller and larger *n* values. Method *EDX-rms* yielded an optimum *n* value of 0.15, however the differences between the *r* values in the *n* range below 0.3 are small. In contrast, method *Batch-CT-rms* yielded an optimum *n* value of 0.45 (with little differences in *r* in the range $0.4 \leq n \leq 0.5$), which is in good agreement with the values obtained with methods *CT-rms* and *CT-mean*.

The slopes dWD/dt_i^n represent the scaling of the imbibition front widening with t_i. In the broader picture represented by **Figure 5.2c**, both methods *CT-rms* and *Batch-CT-rms* yield slopes dWD/dt_i^n, which nearly perfectly coincide. For n = 0.45 in the case of method *CT-rms*, $dWD/dt_i^{0.45}$ amounts to 0.19 µm/min$^{0.45}$. For n = 0.45 in the case of method *Batch-CT-rms*, $dWD/dt_i^{0.45}$ amounts to 0.20 µm/min$^{0.45}$. This outcome is consistent with the results of previous studies on imbibition front broadening. In arrays of independent cylindrical pores exhibiting a certain pore diameter dispersion within the pore array, whereas individual pores are uniform in diameter, as it is the case for AAO, the menisci located in the separated pores move independently. If the movements of the menisci follow Lucas-Washburn dynamics, the imbibition front roughening scales with the square root of the imbibition time t_i. As mentioned previously (cf. Section 5.1.1), it is assumed method *Batch-CT-rms* yields more valid results because much larger probed sample volumes and prevention of artifacts.

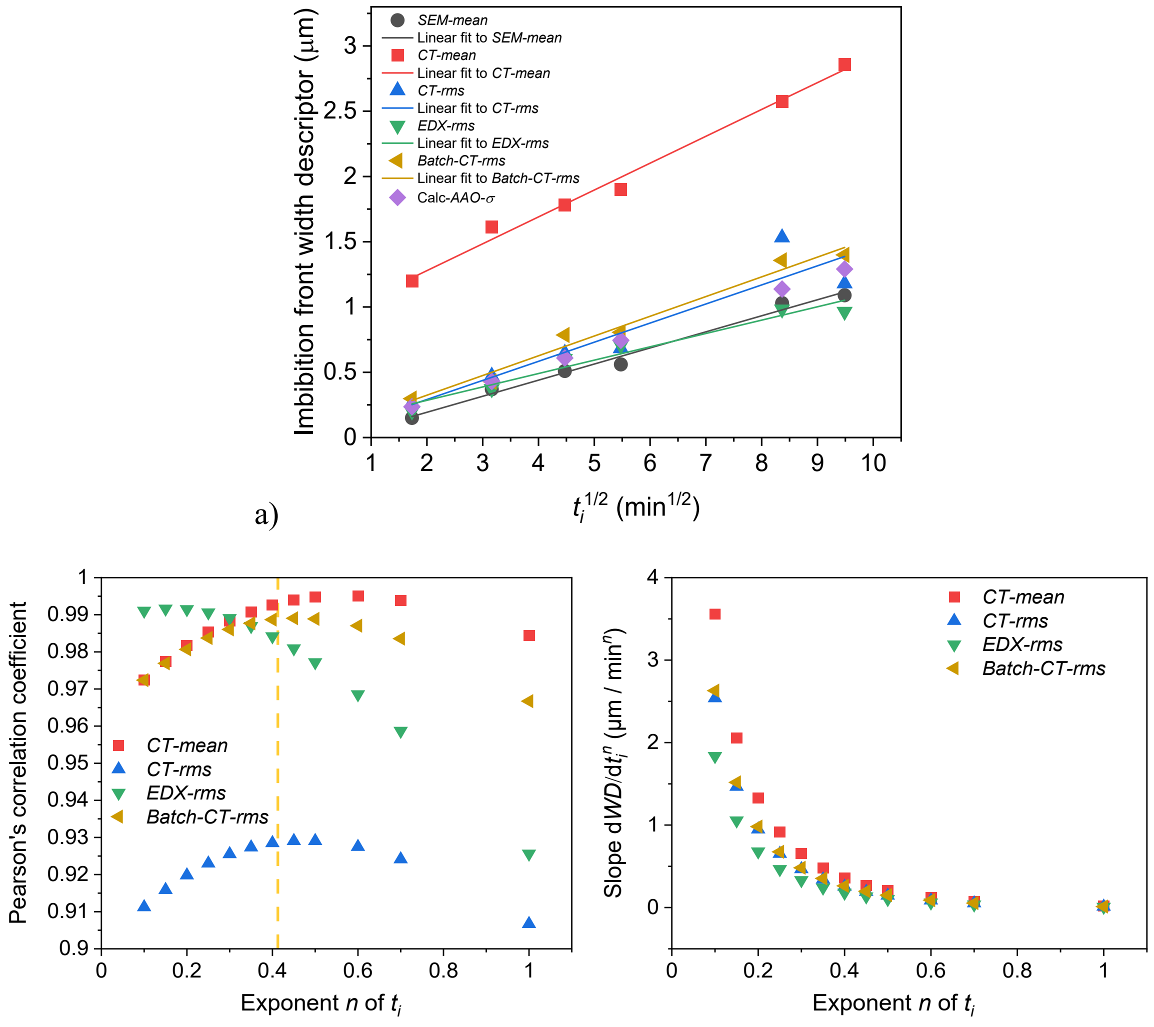

a)

b)

c)

Figure 5.2. a) Comparison of imbibition front width descriptors $WD(t_i^n)$ as measure of the imbibition front width obtained by methods *CT-mean* (red squares), *SEM-mean* (black circles), *CT-rms* (blue up-triangles), *EDX-rms*(green down-triangles) and *Batch-CT-rms* (ochre left-pointing triangles) plotted against the square root $t_i^{1/2}$ of the imbibition time t_i. The solid lines are fits obtained by linear regression. As WDs for methods *CT-mean* and *SEM-mean* $\sigma(t_i)$ is the standard deviation of the single-pore imbibition lengths L_s calculated from the histograms displayed in **Figure 4.11a** and **Figure 4.27c**. As WD for method *CT-rms,* $\sigma(t_i)$ is the standard deviation of Gaussian fits to the peaks in the $R_{q,y}(D)$ profiles displayed in **Figure 4.10b** that represent the imbibition front. As WD for method *Batch-CT-rms* $\sigma(t_i)$ is the standard deviation of Gaussian fits to the peaks in the $R_{q,c}(D)$ profiles displayed in **Figure 4.15a**. As WD for method *EDX-rms* slope factors k_2 of double sigmoidal Boltzmann functions fitted to $R_{q,EDX}(D)$ profiles displayed in **Figure 4.23a**. For comparison, standard deviations of L_s frequency densities obtained by the evaluation of a SEM image of AAO and application of the modified Lucas-Washburn model devised by Yao et al.[17] are shown ("*Calc-AAO-σ*", purple diamonds). b) Pearson correlation coefficients of linear fits to sets of $WD(t_i^n)$ data points obtained by methods *CT-mean*, *CT-rms*, *EDX-rms* and *Batch-CT-rms* for exponents n ranging from 0.1 to 1.0. The dashed yellow line at $n = 0.4125$, indicates the average n value at which r of each method is closer to 1. c) Slopes dWD/dt_i^n plotted against n, the power of t_i^n.

5.2 Imbibition in Isolated Straight *vs* Interconnected Spongy Pores

5.2.1 Average imbibition front positions

Self-ordered AAO containing isolated straight cylindrical pores, with a tortuosity close to 1, is a nearly ideal pore model. CPG contains interconnected sponge-like pores with tortuosity larger than 1. To obtain crucial information on the pore morphology of CPG, the imbibition of PS in CPG was compared with that in AAO. This comparative evaluation of the imbibition provides information on the pore morphology of CPG membranes and on the imbibition mechanisms. Both inorganic oxidic pore models have hydroxyl-terminated pore walls with high specific surface energy so that the interactions between the pore walls and the polystyrene melt should be similar. The pore diameters of ~380 nm of both pore models are one order of magnitude larger than the diameter of gyration of 24 nm of the PS used here.[69] The slopes $\mathrm{d}L_a/\mathrm{d}t_i^{1/2}$ of the linear fits to sets of $L_a(t_i^{1/2})$ data points (**Figure 5.3a** and **Table 5.1**), which correspond to the preexponential factor ν of the Lucas-Washburn law (equation 1.1) are measures of the imbibition velocities. For AAO, methods *SEM-mean* (cf. Section 4.5.2), *CT-mean* (cf. Section 4.2), *CT-rms* (cf. Section 4.2), *EDX-rms* (cf. Section 4.4) and *Batch-CT-rms* (cf. Section 4.3) yielded results which are in good agreement. For the CPG samples, the results obtained by methods *SEM-mean* (cf. Section 4.5.3), *Batch-CT-rms* and *EDX-rms* are likewise in line.

A direct comparison of the slopes $\mathrm{d}L_a/\mathrm{d}t_i^{1/2}$ for AAO and CPG can be drawn by considering the values obtained with the same evaluation method. The slope $\mathrm{d}L_a/\mathrm{d}t_i^{1/2}$ obtained by method *Batch-CT-rms* for the AAO samples is 1.48 times higher than the slope $\mathrm{d}L_a/\mathrm{d}t_i^{1/2}$ obtained by method *Batch-CT-rms* for the CPG samples. The slope $\mathrm{d}L_a/\mathrm{d}t_i^{1/2}$ obtained by method *SEM-mean* is 1.46 times higher than the one obtained by method *SEM-mean* for CPG and finally the slope $\mathrm{d}L_a/\mathrm{d}t_i^{1/2}$ obtained with method *EDX-rms* for the AAO samples is 1.53 times higher than the slope dL_a/d$t_i^{1/2}$ obtained by method *EDX-rms* for the CPG samples. Considering the slopes of the six methods for AAO and the slopes of the four methods for CPG, the average slope obtained for AAO $v_{a,A}$ is 1.52 times higher than the average slope $v_{a,C}$ for CPG. The differences in the slopes dL_a/d$t_i^{1/2}$ can be rationalized by the different tortuosities of AAO and CPG. The geometric tortuosity is defined as the ratio of the lengths of a curvilinear percolation path and the linear distance between two points in a porous matrix.[73] The average imbibition length L_a is the linear distance D between the membrane surface and the center of the imbibition front. For straight cylindrical pores, as in self-ordered AAO, the tortuosity is close to 1, and L_a corresponds to the actual distance the invading fluid has to travel through the AAO pores to reach a distance D from the membrane surface corresponding to L_a. The lengths of the curvilinear percolation paths through the CPG pore systems, which are available to an invading fluid to reach a distance D from the membrane surface corresponding to L_a, are larger than L_a. Hence, the phenomenological imbibition velocities and, therefore, the slopes dL_a/d$t_i^{1/2}$ are smaller for CPG than for AAO. The 1.52 times faster imbibition front movement in AAO relative to that in CPG with a porosity of 58 % used here suggests a CPG tortuosity on the order of 1.5 This value is indeed a reasonable estimate, as discussed below. At first glance, a tortuosity of 1.5 appears to be low for an isotropic pore model. However, it was shown that the nature of percolation paths through a pore model and, therefore, the tortuosity mainly depends on the porosity[75] (whereas the pore radius is typically not being considered a relevant parameter). CPGs with pore diameters of 10 - 20 nm but a porosity of 50 % – 60 % were reported to have tortuosities of 1.5 - 1.6, as determined by permeability measurements.[137-138] Furthermore, Shelekhin et al. showed that the porosity and the tortuosity in porous glass membranes can be described by means of the percolation theory.[139] These authors defined the tortuosity as an empirical coefficient to describe the random orientation of the pores determined not only by the diffusion paths but also by the amount of throughout porosity and calculated the tortuosity based on the porosity (fraction of leachables). For low porosities (< 30 %) high tortuosities were obtained. In good agreement with the experimental value of 5.9, a tortuosity of 6.5 was calculated for VYCOR glass with a porosity of 31 %. The theoretical calculations also showed that an increase in the porosity of the membranes to 60 % results in a decrease of the tortuosity to 1.5.

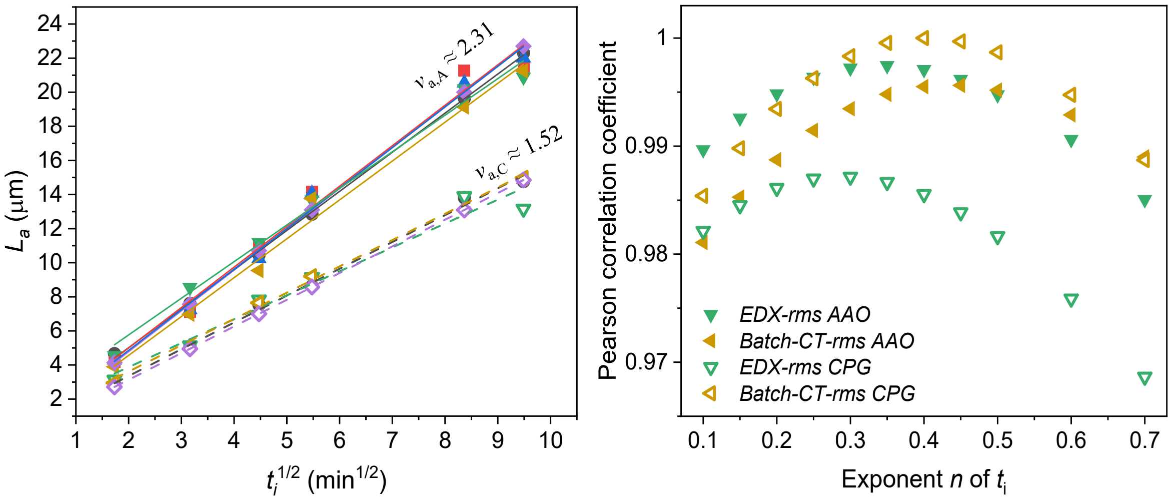

a) b)

Figure 5.3. Comparison of the average imbibition lengths $L_a(t_i)$ obtained with methods *CT-mean* (red squares), *SEM-mean* (black circles), *CT-rms* (blue up-triangles), *EDX-rms* (green down-triangles) and *Batch-CT-rms* (ochre left-pointing triangles) for AAO (solid symbols) and CPG (open symbols) membranes infiltrated with PS at 200°C. Pink diamonds are results of calculations of L_a from L_s with equation (4.4) for AAO and L_a for CPG with equation (4.13). a) L_a plotted against the square root of the imbibition time $t_i^{1/2}$. Solid lines are fits to sets of data points obtained with AAO membranes and dashed lines fits to sets of data points obtained with CPG membranes. b) Pearson correlation coefficients of linear fits to sets of $L_a(t_i^n)$ data points obtained by methods *EDX-rms* and *Batch-CT-rms* plotted against the exponent n of t_i.

Next, comparison of the Pearson correlation coefficients with the highest linearity, r closest to 1, between AAO and CPG was done (**Figure 5.3b**). The analysis of 3D reconstructions of the CPG samples obtained by X-ray computed tomography using method *Batch-CT-rms* revealed that r was closest to 1 for $n = 0.4$, whereas the analysis of 3D reconstructions of the AAO samples obtained by X-ray computed tomography using method *Batch-CT-rms* revealed that r was closest to 1 for $n = 0.45$. Analysis of the EDX maps by method *EDX-*

rms yielded the best *r* values for *n* values of 0.35 (AAO) and 0.3 (CPG), as compared to the *n* value of 0.5 predicted by the classical Lucas-Washburn theory.[103-104] This outcome is interpreted as follows. The exponents *n* of t_i yielding the best linear fits to the sets of $L_a(t_i)$ data points obtained by X-ray CT (method *Batch-CT-rms*) are in reasonable agreement with the expectations emerging from physical considerations (cf. Chapter 1). The exponent obtained for AAO with its separated cylindrical pores is close to 0.5, the exponents obtained for CPG are somewhat smaller. However, the exponents *n* of t_i obtained by statistical evaluation of results computed X-ray tomography (method *Batch-CT-rms*) and EDX mappings (method *EDX-rms*) differ to some extent. Method *Batch-CT-rms* is assumed to yield more valid results because much larger sample volumes are probed and preparation artifacts are prevented that may occur when infiltrated membranes are cleaved to prepare cross-sectional specimens for the EDX mappings. In this context it should be noted that Cai and Yu suggested to correct the exponent *n* of t_i describing the scaling of the imbibition length L_a with t_i by a fractal dimension for tortuosity.[33]

5.2.2 Imbibition front widths

As discussed in Section 5.1, for imbibition processes and imbibition stages characterized by imbibition front widths from the sub-micron range to a few microns it is challenging, if not impossible, to reliably determine absolute imbibition front widths. Instead, statistical descriptors of imbibition front widths (width descriptors, *WD*) may be used, which can be extracted from experimental raw data by means of defined algorithms. The color map $R_{q,c}(D)$ profiles obtained by method *Batch-CT-rms* illustrate that specifically adapted descriptors for the imbibition front widths are required. In the case of the color map $R_{q,c}(D)$ profiles obtained by method *Batch-CT-rms* for the AAO samples the position of the imbibition front is marked by peaks (2) rather than by steps **(Figure 4.15a**). Therefore, in this case standard deviations σ of Gaussian fits to the color map $R_{q,c}(D)$ profiles in a D range around L_a were used as *WD* (**Figure 4.16a**). However, step (2) in the color map $R_{q,c}(D)$ profiles obtained for CPG samples (**Figure 4.15b**) was fitted by a sigmoidal Boltzmann function (**Figure 4.16b**). In this case, the slope factor k_B is a suitable *WD*. In the case of method *EDX-rms*, the imbibition front in the AAO as well as the CPG membranes is indicated by step (2) in the sigmoidal double-Boltzmann functions fitted to the $R_{q,EDX}(D)$ profiles obtained by evaluation of EDX maps (**Figure 4.22**). In this case, the slope factor $k_{EDX,2}$ of step (2), which has the same properties as slope factor k_B, is used descriptor of the imbibition front width. The slopes $\mathrm{d}WD/\mathrm{d}t_i^{1/2}$ of linear fits to sets of $WD(t_i^{1/2})$ data points were used to comparatively quantify the spatiotemporal evolution of the imbibition front width (**Figure 5.4a**). However, only $WD(t_i^{1/2})$ data points obtained with slope factors k_B or $k_{EDX,2}$ as *WD* can be compared directly. The slope $\mathrm{d}k_B/\mathrm{d}t_i^{1/2}$ to sets of $k_B(t_i^{1/2})$ data points obtained for CPG samples by method *Batch-CT-rms* amounts to 0.50 µm $s^{-1/2}$, while method *EDX-rms* yielded for the CPG samples $\mathrm{d}k_{EDX,2}/\mathrm{d}t_i^{1/2}$ = 0.59 µm $s^{-1/2}$. Furthermore, the $\mathrm{d}k_{EDX,2}/\mathrm{d}t_i^{1/2}$ value obtained for the CPG samples amounted to 58 % of the value obtained for the AAO samples (as compared to 65–68 % for the $\mathrm{d}L_a/\mathrm{d}t_i^{1/2}$ values).

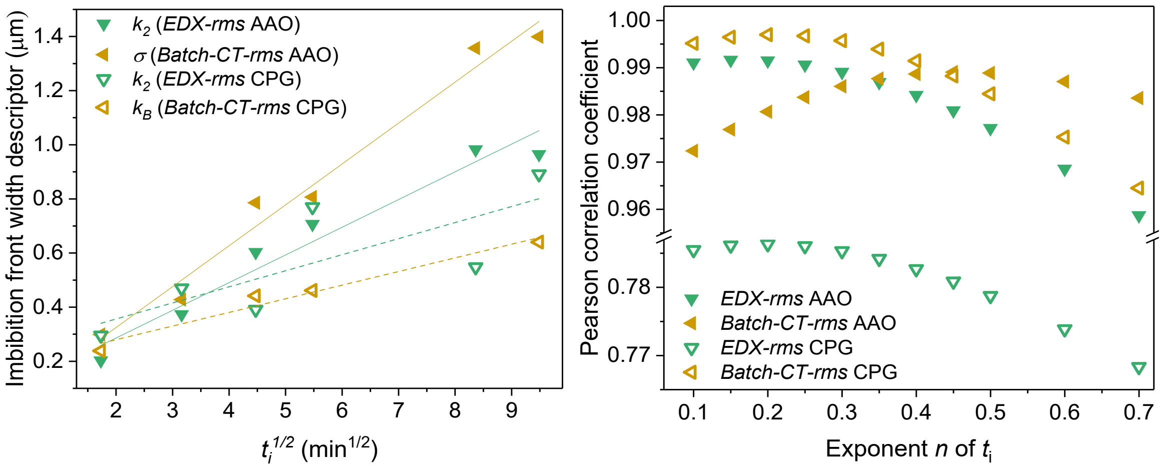

a) b)

Figure 5.4. Comparison of the imbibition front width descriptors (*WD*) obtained by methods *Batch-CT-rms* (ochre left-pointing triangles) and *EDX-rms* (green down-triangles) for AAO (solid symbols) and CPG (open symbols) infiltrated with PS at 200°C. As *WDs* standard deviations σ of Gaussian functions fitted to peaks (2) in color map $R_{q,c}(D)$ profiles (method *Batch-CT-rms* for AAO), slope factors k_B of sigmoidal Boltzmann functions fitted to step (2) of color map $R_{q,c}(D)$ profiles (method *Batch-CT-rms* for CPG) and slope factors k_2 of double sigmoidal Boltzmann functions fitted to $R_{q,EDX}(D)$ profiles (method *EDX-rms* for AAO and CPG) were used. a) *WD* plotted against the square root of the imbibition time $t_i^{1/2}$. Solid lines are fits to sets of data points obtained with AAO membranes and dashed lines fits to sets of data points obtained with CPG membranes. b) Pearson correlation coefficients of linear fits to sets of $WD(t_i^n)$ data points obtained by methods *EDX-rms* and *Batch-CT-rms* plotted against the exponent n of t_i.

In analogy with Section 5.2.1, a comparison between the Pearson correlation coefficients that yield the best linear correlation to sets of $WD(t_i^n)$ data points was made as well (**Figure 5.4b**). For this purpose, the Pearson correlation coefficient r of linear fits obtained for different values of the exponent n of t_i was determined. An n value of 0.20 yielded the best linear fits to sets of data points obtained with methods *Batch-CT-rms* and *EDX-rms* for the CPG samples. However, due to the minute r variations for n values smaller than 0.30 it is difficult to unambiguously determine optimum n values. Moreover, the linear fits to the data points resulting from method *EDX-rms* have low r values smaller than 0.79. For the AAO samples, methods *Batch-CT-rms* and *EDX-rms* yielded inconclusive results. Method *EDX-rms* yielded an optimum n value of 0.15, albeit also here the differences between the r values in the n range below 0.3 are small. In contrast, method *Batch-CT-rms* yielded an optimum n value of 0.45 (with little differences in r in the range $0.4 \leq n \leq 0.5$), which is in good agreement with the values obtained previously with methods *CT-rms* and *CT-mean* (cf. Section 5.1.2).

Considering the results of method *Batch-CT-rms*, for which sample volumes of at least 30 000 µm^3 were evaluated (in contrast to method *EDX-rms* considering only 2D maps), it can be concluded that the imbibition front width in AAO increases faster with t_i than in CPG (**Figure 5.4a**). This outcome agrees with previously reported models of imbibition front broadening.[41] In arrays of independent cylindrical nanopores with uniform diameter along individual pores but a certain pore diameter dispersion within the pore array, as in AAO, the menisci located in the separated pores move independently. If the movements of the menisci follow Lucas-Washburn dynamics, the imbibition front roughening scales with the square root of the imbibition time t_i. By contrast, for spongy-continuous pore networks without neck-like pore segments, as in the CPGs used here, the imbibition front roughening scales with t_i raised to the power of an exponent smaller than 0.5. In this case, the menisci do not move independently along the pores. Instead, an effective surface tension counteracts the broadening mechanisms.[28, 41] The powers n of t_i in the power laws describing the scaling of the imbibition front width descriptors *WD* with t_i determined by method *Batch-CT-rms*, which are associated with the best Pearson correlation coefficients, amount to 0.45 for AAO and 0.20 for CPG. These values are in good agreement with the theoretical predictions. Notably, imaging of spontaneous imbibition of water into nanoporous Vycor glass with a pore diameter two orders of magnitude smaller than that of the CPGs studied here using reflected light and neutrons revealed that imbibition front roughening scaled with the square root of t_i.[41] This outcome was traced to independent menisci movements in elongated pore segments. Thus, the results obtained by method *Batch-CT-rms* corroborate the notion that Vycor glass with pore diameters below 10 nm contains a higher proportion of cylindrical pore segments than the CPGs used here with a mean pore diameter of 380 nm.

5.3 Comparison of Statistical Methods

To evaluate the phase-contrast X-ray computed tomography data from AAO a three-stage semi-automatic algorithm was developed to analyze 3D reconstructions of X-ray CT, which yields brightness profiles along all identified AAO pores in the probed sample volume. Then, histograms of single-pore imbibition lengths (*CT-mean*, cf. Section 4.2), or the statistical brightness dispersion as a function of the distance to the AAO surface (*CT-rms*, cf. Section 4.2) were evaluated. Both *CT-mean* and *CT-rms* methods have the advantage of determination of individual AAO pore coordinates, single pore imbibition lengths and provide quantitative information on thousands of pores. However, the aforementioned methods can only be applied on ordered straight pores like the ones found in AAO.

To overcome the restriction of the previous above-mentioned method, a second approach able to analyze 3D reconstructions of X-ray CT that does neither involve segmentation procedures nor requires the determination of pore coordinates based on the evaluation of pixel intensity dispersion parallel to the membrane surfaces and thus applicable to both AAO and CPG membranes (*Batch-CT-rms*, cf. Section 4.3) was developed. The 3D reconstructions were condensed into 1D profiles normal to the membrane surfaces representing the pixel intensity dispersion as a function of the distance to the membrane surface. To process the 3D reconstructions in this way, a two-step algorithm was developed comprising the successive calculation of pixel intensity dispersion profiles along two orthogonal directions parallel to the membrane surface. This method provides quantitative information on thousands of pores for AAO and tens of thousands of cubic micrometers in the case of CPG. However, the volume of interest must be chosen and processed carefully to remove artifacts that might reduce the accuracy of the algorithm to identify the relevant morphological features.

The same pixel intensity dispersion approach from *Batch-CT-rms* method was used for comparison with 2D EDX maps (*EDX-rms* cf. Section 4.4). It extracts the spatial distribution of carbon from PS in the sample thus not requiring segmentation or determination of pore coordinates and therefore it can be applied to AAO and CPG as well. The $R_{q,EDX}$ (D) profiles obtained of both AAO and CPG, consist of characteristic steps at approximate positions of the membrane surfaces and the imbibition front that are easy to analyze with a sigmoidal Boltzmann function. However, the information extraction is limited to the surface of the cross-section of the infiltrated membranes without access to the bulk, providing quantitative information of only tens of pores.

The final approach, *SEM-mean* is based on the evaluation of histograms of single-pore imbibition lengths obtained by manually measuring in the probed sample cross-sections of AAO and CPG (cf. Sections 4.5.2 and 4.5.3). It reproduces the morphological features of the membranes such as the membrane surfaces, pores, PS surface film, PS-filled pore segments and imbibition front with the largest resolution but only the surface of the sample cross-section is available for analysis and thus provides quantitative information of only tens of pores. It is also prone to bias due to the measurements done manually.

Each method is capable of determining the imbibition front position and width and providing descriptors for it after histogram evaluation or fitting of the $R_q(D)$ profiles obtained from each one. **Table 5.1** summarizes all the relevant parameters obtained with the aforementioned methods.

Table 5.1. Numbers N of the AAO pores considered per sample, Pearson correlation coefficients r and slopes $\nu = \mathrm{d}L_a/\mathrm{d}t_i^{1/2}$ of the linear fits $L_a(t_i^{1/2})$ in **Figure 5.1b,c** and **Figure 5.3b** as well as Pearson correlation coefficients r and slopes $\mathrm{d}WD/\mathrm{d}t_i^{1/2}$ of the linear fits to the used imbibition front width descriptors (WD) plotted against $t_i^{1/2}$ data sets in **Figure 5.2b,c** and **Figure 5.4b**. As imbibition front width descriptors, σ (methods *SEM-mean*, *CT-mean*, *CT-rms*, *Batch-CT-rms* for AAO), k_B (method *Batch-CT-rms* for CPG), k_2 (method *EDX-rms* for AAO and CPG).

Porous Material	N	Method	*r value* L_a $(t_i^{1/2})$	ν [µm/min$^{1/2}$]	r value $WD(t_i^{1/2})$	$\mathrm{d}WD/\mathrm{d}t_i^{1/2}$ [µm/min$^{1/2}$]
AAO	*≈2705-7166*	*Batch-CT-rms*	0.995	2.280	0.989	0.151
AAO	*≈59-130*	*EDX-rms*	0.994	2.148	0.977	0.102
AAO	*30*	*SEM-mean*	0.999	2.293	0.993	0.123
AAO	*1304-4796*	*CT-rms*	0.996	2.380	0.929	0.146
AAO	*1304-4796*	*CT-mean*	0.991	2.372	0.994	0.205
AAO	*1304-4796*	*Calc-AAO*	--	2.392	--	0.136
CPG		*Batch-CT-rms*	0.999	1.542	0.984	0.050
CPG		*EDX-rms*	0.981	1.402	0.778	0.059
CPG		*SEM-mean*	0.997	1.573	0.974	0.101
CPG		*Calc-CPG*	--	1.565	--	--

6 Conclusion and Outlook

Liquid imbibition has been and remains a relevant topic of study among diverse fields of science and industry. However, the understanding of liquid imbibition into porous scaffolds with submicron-sized pores is still premature – even for separated straight cylindrical pores, in which cooperative effects related to hydraulically coupled menisci are ruled out. To nourish this knowledge field, the imbibition of polystyrene into AAO containing isolated straight cylindrical pores and CPG containing spongy-continuous pore systems was comparatively studied with specifically developed statistical methods. Both pore models have hydroxyl-terminated oxidic pore walls and pore diameters of ~380 nm, which exceed the dimensions of the infiltrated macromolecules by one order of magnitude. Additionally, the polymer with a high glass transition temperature used here allows freezing of transient imbibition stages by cooling and vitrification. Therefore, *ex situ* characterization of frozen transient imbibition stages using techniques that require several hours of measurements, such as X-ray tomography, is possible.

Focus was given to data obtained from phase-contrast X-ray computed tomography, which can resolve single pores with diameters in the submicron range and is particularly suitable for detecting interfaces in three dimensions. Compared to averaging methods to monitor imbibition without single-pore resolution, phase-contrast X-ray CT allowed direct microscopic real-space observation of the relevant sample features. In comparison with standard microscopy, much larger sample volumes are probed and compared to FIB tomography, preparation artifacts were prevented. The results were compared for validation with results from two-dimensional techniques, scanning electron microscopy, and energy-dispersive x-ray elemental mapping.

Five image analysis methods in total were developed in which descriptive statistics were used to determine imbibition front positions and imbibition front widths.

- Methods *CT-mean* and *CT-rms* (cf. Section 4.2) have the advantage of determination of individual AAO pore coordinates, single pore imbibition lengths and provide information on thousands of pores. However, the aforementioned methods can only be applied on straight parallel pores like the ones found in AAO.
- Method *Batch-CT-rms* (cf. Section 4.3) does neither involve segmentation procedures nor requires the determination of pore coordinates and can be applied to both AAO and CPG. It provides quantitative information on thousands of pores for AAO and tens of thousands of cubic micrometers in the case of CPG. However, the volume of interest must be processed carefully to remove artifacts that might reduce the accuracy of the algorithm to identify the relevant morphological features. This method is assumed to yield the more valid results because it is the one with the largest sample volumes probed.
- Method *EDX-rms* has the advantage of extracting the spatial distribution of carbon from PS in the sample thus not requiring segmentation or determination of pore coordinates and thus it can be applied to AAO and CPG. However, the information extraction is limited to the surface of the cross-section of the infiltrated membranes without access to the bulk, providing quantitative information of only tens of pores. Preparation artifacts may occur when infiltrated membranes are cleaved to prepare cross-sectional specimens for the EDX mappings.
- Method *SEM-mean* is based on the evaluation of histograms of single-pore imbibition lengths obtained by manually measuring the PS-filled pore segments from the probed

sample cross-sections of AAO and CPG (cf. Sections 4.5.2 and 4.5.3). It has the advantage of reproducing the morphological features of interest from the imbibed membranes with the largest resolution but only the surface of the sample cross-section is available for analysis and thus provides quantitative information of only tens of pores. It is also prone to bias due to the measurements done manually.

It is commonly assumed that the imbibition length scales with the imbibition time to the power of 0.5, as predicted by the Lucas-Washburn theory. The Pearson correlation coefficient of linear fits to sets of imbibition length/imbibition time data sets for different exponents was determined, and the best linear correlation was found for exponents slightly deviating from 0.5. This outcome suggests that not only the imbibition prefactor in the Lucas-Washburn equation but also the exponent of the imbibition time should be scrutinized.

Using the preexponential factor ν experimentally determined from X-ray computed tomography data and CPG pore diameter frequency densities obtained by mercury intrusion, the average imbibition front positions in CPG could be reproduced by the Lucas-Washburn law. Using the preexponential factor ν and a pore diameter histogram of AAO obtained from an SEM image, the imbibition length frequency densities and thickness of the dead layers were calculated with the Lucas-Washburn law as well. The preexponential factor ν of the Lucas-Washburn law relating the imbibition front position to the imbibition time found for the AAO samples is 1.5 times larger than that found for the CPG samples. This outcome is in excellent agreement with the geometric tortuosity of CPG reported earlier. Thus, imbibition retardation with respect to AAO reference samples having a geometric tortuosity of 1 may quantify the geometric tortuosity of a probed pore system on the condition that surface interactions are comparable.

The scaling of imbibition front widths with the elapsed imbibition time represents the dispersion of the AAO or CPG pore diameters and yields information on the pore morphology. However, it is demanding to unambiguously identify the two imbibition front onset points for the direct determination of imbibition front widths. Instead, dispersion measures of peaks or steps indicating the presence of imbibition fronts in plots of suitable image properties against the distance from the membranes surface were used to quantify imbibition front widths. Since the relevant length scales are one order of magnitude smaller than the length scales relevant to the determination of the mean imbibition front position, numerical values of measures of the imbibition front width stronger depend on the applied imaging method and the statistical evaluation methodology.

Hence, a naïve comparison of numerical values obtained by different experimental methodologies is misleading. To get comparable results, clearly defined, reproducible algorithms comprising the measurement method and statistical data evaluation need to be applied. This implies that attention needs to be directed to the compatibility of experimental measures of imbibition front widths and theoretical imbibition models.

The results of methods *CT-mean*, *CT-rms,* and *Batch-CT-rms* obtained with AAO as well-characterized pore model validate theoretical predictions by Gruener et al.,[41, 49] according to which the imbibition front width scales with $t_i^{1/2}$ if pore models containing cylindrical pores uniform in diameter are used. Also, the results obtained corroborate the notion that a dead layer of macromolecules immobilized on the AAO pore walls influences imbibition dynamics.

Analysis of the 1D brightness dispersion profiles also yields statistical descriptors of the imbibition front widths, the dependence of which on the imbibition times reveals to what extent individual or cooperative meniscus movements govern imbibition. X-ray computed tomography data indicate that, in contrast to Vycor glass with sub-10-nm pores, meniscus movements in the CPGs used here are governed by cooperative effects. This outcome indicates that neck-like cylindrical pore segments do not significantly impact the spatiotemporal imbibition front evolution in the CPGs tested here.

The results presented here may help achieve a predictive understanding of imbibition into synthetic self-ordered porous materials with isolated straight cylindrical pores and synthetic or real-life materials with spongy-continuous pore systems relevant to applications including printing and adhesive bonding and the fabrication of hybrid materials.

7 Bibliography

[1] R. Lenormand, *Journal of Physics-Condensed Matter* **1990**, 2, SA79.
[2] A. G. Hunt, M. Sahimi, *Reviews of Geophysics* **2017**, 55, 993.
[3] S. Saraf, A. Bera, *Renew Sust Energ Rev* **2021**, 144.
[4] J. X. Chen, K. Zhang, K. Y. Zhang, L. Yang, B. Jiang, *Journal of Applied Polymer Science* **2021**, 138, e50894.
[5] M. Zakizade, A. Davoudi, A. Akhavan, F. Shirban, *Journal of Evidence-Based Dental Practice* **2020**, 20.
[6] P. E. de Jongh, T. M. Eggenhuisen, *Advanced Materials* **2013**, 25, 6672.
[7] C. Mijangos, R. Hernandez, J. Martin, *Progress in Polymer Science* **2016**, 54-55, 148.
[8] H. Wu, Y. Higaki, A. Takahara, *Progress in Polymer Science* **2018**, 77, 95.
[9] D. N. Dirin, L. Protesescu, D. Trummer, I. V. Kochetygov, S. Yakunin, F. Krumeich, N. P. Stadie, M. V. Kovalenko, *Nano Lett.* **2016**, 16, 5866.
[10] K. Sentker, A. Yildirim, M. Lippmann, A. W. Zantop, F. Bertram, T. Hofmann, O. H. Seeck, A. V. Kityk, M. G. Mazza, A. Schonhals, P. Huber, *Nanoscale* **2019**, 11, 23304.
[11] E. J. W. Crossland, M. Kamperman, M. Nedelcu, C. Ducati, U. Wiesner, D. M. Smilgies, G. E. S. Toombes, M. A. Hillmyer, S. Ludwigs, U. Steiner, H. J. Snaith, *Nano Lett.* **2009**, 9, 2807.
[12] M. Beiner, G. T. Rengarajan, S. Pankaj, D. Enke, M. Steinhart, *Nano Lett.* **2007**, 7, 1381.
[13] M. Rauscher, S. Dietrich, *Annual Review of Materials Research* **2008**, 38, 143.
[14] P. Debye, R. L. Cleland, *Journal of Applied Physics* **1959**, 30, 843.
[15] S. Gruener, T. Hofmann, D. Wallacher, A. V. Kityk, P. Huber, *Physical Review E* **2009**, 79.
[16] A. Kusmin, S. Gruener, A. Henschel, O. Holderer, J. Allgaier, D. Richter, P. Huber, *Journal of Physical Chemistry Letters* **2010**, 1, 3116.
[17] Y. Yao, H. J. Butt, G. Floudas, J. J. Zhou, M. Doi, *Macromolecular Rapid Communications* **2018**, 39.
[18] T. Sochi, *Polymer Reviews* **2011**, 51, 309.
[19] L. G. Cencha, G. Dittrich, P. Huber, C. L. A. Berli, R. Urteaga, *Phys Rev Lett* **2020**, 125.
[20] M. Steinhart, *Advances in Polymer Science* **2008**, 220, 123.
[21] B. Y. Cao, M. Yang, G. J. Hu, *Rsc Adv* **2016**, 6, 7553.
[22] M. Engel, B. Stühn, *J Chem PhysJournal of Chemical Physics* **2010**, 132, 224502.
[23] F. Vazquez Luna, M. Gerstenberger, G. Dittrich, J. Martins de Souza e Silva, P. Huber, R. Wehrspohn, M. Steinhart, *The Journal of Physical Chemistry C* **2021**, 125, 26731.
[24] M. Reyssat, L. Courbin, E. Reyssat, H. A. Stone, *J Fluid Mech* **2008**, 615, 335.
[25] H. Masuda, K. Yada, A. Osaka, *Japanese Journal of Applied Physics Part 2-Letters & Express Letters* **1998**, 37, L1340.
[26] K. Singh, M. Jung, M. Brinkmann, R. Seemann, *Annual Review of Fluid Mechanics* **2019**, 51, 429.
[27] D. Enke, F. Janowski, W. Schwieger, *Micropor Mesopor Mat* **2003**, 60, 19.
[28] M. Alava, M. Dube, M. Rost, *Advances in Physics* **2004**, 53, 83.
[29] T. Gambaryan-Roisman, *Current Opinion in Colloid & Interface Science* **2014**, 19, 320.
[30] A. Mehmani, S. Kelly, C. Torres-Verdin, *Petrophysics* **2019**, 60, 872.

[31] J. Schoelkopf, P. A. C. Gane, C. J. Ridgway, G. P. Matthews, *Colloids and Surfaces a-Physicochemical and Engineering Aspects* **2002**, 206, 445.

[32] M. S. Valavanides, *Transport in Porous Media* **2018**, 123, 45.

[33] J. C. Cai, B. M. Yu, *Transport in Porous Media* **2011**, 89, 251.

[34] S. Berg, H. Ott, S. A. Klapp, A. Schwing, R. Neiteler, N. Brussee, A. Makurat, L. Leu, F. Enzmann, J. O. Schwarz, M. Kersten, S. Irvine, M. Stampanoni, *Proc. Natl. Acad. Sci. USA* **2013**, 110, 3755.

[35] M. J. Blunt, H. Scher, *Physical Review E* **1995**, 52, 6387.

[36] A. Dougherty, N. Carle, *Physical Review E* **1998**, 58, 2889.

[37] S. Roux, E. Guyon, *Journal of Physics a-Mathematical and General* **1989**, 22, 3693.

[38] S. Santucci, R. Planet, K. J. Maloy, J. Ortin, *Europhys. Lett.* **2011**, 94.

[39] G. M. Homsy, *Annual Review of Fluid Mechanics* **1987**, 19, 271.

[40] S. V. Buldyrev, A. L. Barabasi, F. Caserta, S. Havlin, H. E. Stanley, T. Vicsek, *Physical Review A* **1992**, 45, R8313.

[41] S. Gruener, Z. Sadjadi, H. E. Hermes, A. V. Kityk, K. Knorr, S. U. Egelhaaf, H. Rieger, P. Huber, *Proceedings of the National Academy of Sciences of the United States of America* **2012**, 109, 10245.

[42] Z. Sadjadi, H. Rieger, *Phys Rev Lett* **2013**, 110.

[43] J. C. Cai, E. Perfect, C. L. Cheng, X. Y. Hu, *Langmuir* **2014**, 30, 5142.

[44] Y. Yao, Y. Suzuki, J. Seiwert, M. Steinhart, H. Frey, H. J. Butt, G. Floudas, *Macromolecules* **2017**, 50, 8755.

[45] Y. Yao, S. Alexandris, F. Henrich, G. Auernhammer, M. Steinhart, H. J. Butt, G. Floudas, *J Chem PhysJournal of Chemical Physics* **2017**, 146, 203320.

[46] A. Serghei, D. Chen, D. H. Lee, T. P. Russell, *Soft Matter* **2010**, 6, 1111.

[47] C. H. Tu, M. Steinhart, H. J. Butt, G. Floudas, *Macromolecules* **2019**, 52, 8167.

[48] C. H. Tu, J. J. Zhou, M. S. Doi, H. J. Butt, G. Floudas, *Phys. Rev. Lett.* **2020**, 125, 127802.

[49] S. Gruener, H. E. Hermes, B. Schillinger, S. U. Egelhaaf, P. Huber, *Colloids and Surfaces a-Physicochemical and Engineering Aspects* **2016**, 496, 13.

[50] P. Huber, S. Grüner, C. Schäfer, K. Knorr, A. V. Kityk, *European Physical Journal -Special Topics* **2007**, 141, 101.

[51] Y. H. Xue, J. Markmann, H. L. Duan, J. Weissmuller, P. Huber, *Nat Commun* **2014**, 5.

[52] S. Gruener, P. Huber, *Transport in Porous Media* **2019**, 126, 599.

[53] L. N. Acquaroli, R. Urteaga, C. L. A. Berli, R. R. Koropecki, *Langmuir* **2011**, 27, 2067.

[54] L. G. Cencha, R. Urteaga, C. L. A. Berli, *Macromolecules* **2018**, 51, 8721.

[55] M. Mercuri, K. Pierpauli, M. G. Bellino, C. L. A. Berli, *Langmuir* **2017**, 33, 152.

[56] M. Sallese, J. Torga, E. Morel, N. Budini, R. Urteaga, *Journal of Applied Physics* **2020**, 128.

[57] O. Vincent, B. Marguet, A. D. Stroock, *Langmuir* **2017**, 33, 1655.

[58] O. Vincent, A. Szenicer, A. D. Stroock, *Soft Matter* **2016**, 12, 6656.

[59] H. Masuda, K. Fukuda, *Science* **1995**, 268, 1466.

[60] A. Ruiz-Clavijo, O. Caballero-Calero, M. Martin-Gonzalez, *Nanoscale* **2021**, 13, 2227.

[61] S. X. Liu, J. L. Tian, W. Zhang, *Nanotechnology* **2021**, 32, 222001.

[62] S. C. Mayo, T. J. Davis, T. E. Gureyev, P. R. Miller, D. Paganin, A. Pogany, A. W. Stevenson, S. W. Wilkins, *Optics Express* **2003**, 11, 2289.

[63] A. Tkachuk, F. Duewer, H. Cui, M. Feser, S. Wang, W. Yun, *Zeitschrift für Kristallographie* **2007**, 222, 650.

[64] R. Falcone, C. Jacobsen, J. Kirz, S. Marchesini, D. Shapiro, J. Spence, *Contemporary Physics* **2011**, 52, 293.

[65] E. Maire, P. J. Withers, *International Materials Reviews* **2014**, 59, 1.

[66] S. C. Garcea, Y. Wang, P. J. Withers, *Composites Science and Technology* **2018**, 156, 305.

[67] S. Wu, *Journal of Polymer Science Part B-Polymer Physics* **1989**, 27, 723.

[68] L. J. Fetters, D. J. Lohse, S. T. Milner, W. W. Graessley, *Macromolecules* **1999**, 32, 6847.

[69] J. F. Bent, R. W. Richards, T. D. Gough, *Review of Scientific Instruments* **2003**, 74, 4052.

[70] L. G. Cencha, P. Huber, M. Kappl, G. Floudas, M. Steinhart, C. L. A. Berli, R. Urteaga, *Applied Physics Letters* **2019**, 115.

[71] D. Kahneman, O. Sibony, C. R. Sunstein, *Noise: a Flaw in Human Judgment*, William Collins, London **2021**.

[72] J. Rouquerol, D. Avnir, C. W. Fairbridge, D. H. Everett, J. H. Haynes, N. Pernicone, J. D. F. Ramsay, K. S. W. Sing, K. K. Unger, *Pure Appl Chem* **1994**, 66, 1739.

[73] B. Ghanbarian, A. G. Hunt, R. P. Ewing, M. Sahimi, *Soil Sci Soc Am J* **2013**, 77, 1461.

[74] F. Keil, in *Diffusion und Chemische Reaktionen in der Gas/Feststoff-Katalyse*, Springer-Verlag, Berlin, Heidelberg **1999**, Ch. Beschreibung der Porenstruktur von Katalysatorträgern.

[75] J. Comiti, M. Renaud, *Chem Eng Sci* **1989**, 44, 1539.

[76] K. Meyer, P. Lorenz, B. Bohlkuhn, P. Klobes, *Cryst Res Technol* **1994**, 29, 903.

[77] H. Masuda, F. Hasegwa, S. Ono, *J Electrochem Soc* **1997**, 144, L127.

[78] W. Lee, R. Ji, U. Gosele, K. Nielsch, *Nat Mater* **2006**, 5, 741.

[79] K. Nielsch, J. Choi, K. Schwirn, R. B. Wehrspohn, U. Gosele, *Nano Lett* **2002**, 2, 677.

[80] F. Le Coz, L. Arurault, L. Datas, *Mater Charact* **2010**, 61, 283.

[81] W. Lee, S. J. Park, *Chem Rev* **2014**, 114, 7487.

[82] W. Lee, J. C. Kim, *Nanotechnology* **2010**, 21.

[83] F. Janowski, D. Enke, in *Handbook of Porous Solids*, Vol. 3 (Ed: F. Schüth, Sing, K. S. W., Weitkamp, J.), Wiley-VCH, Weinheim **2002**, p. 1432.

[84] F. Schüth, K. S. W. Sing, J. Weitkamp, *Handbook of porous solids*, Wiley-VCH, Weinheim ; Cambridge **2002**.

[85] H. P. Hood, Nordberg, M. E. (Corning Glass Works) *US*, **1934**.

[86] W. Vogel, *J Non-Cryst Solids* **1977**, 25, 170.

[87] W. Haller, *Nature* **1965**, 206, 693.

[88] W. Haller, *J Chem Phys* **1965**, 42, 686.

[89] W. Haller, P. B. Macedo, *Phys Chem Glasses* **1968**, 9, 153.

[90] W. Vogel, *Glass chemistry*, Springer-Verlag, Berlin ; New York **1994**.

[91] T. Yazawa, R. Kuraoka, W. F. Du, *J Phys Chem B* **1999**, 103, 9841.

[92] A. Inayat, B. Reinhardt, J. Herwig, C. Kuster, H. Uhlig, S. Krenkel, E. Raedlein, D. Enke, *New J Chem* **2016**, 40, 4095.

[93] H. K. Christenson, *Journal of Physics-Condensed Matter* **2001**, 13, R95.

[94] D. Enke, F. Friedel, F. Janowski, T. Hahn, W. Gille, R. Muller, H. Kaden, *Stud Surf Sci Catal* **2002**, 144, 347.

[95] S. Gruener, D. Wallacher, S. Greulich, M. Busch, P. Huber, *Physical Review E* **2016**, 93.

[96] J. Rouquerol, G. V. Baron, R. Denoyel, H. Giesche, J. Groen, P. Klobes, P. Levitz, A. V. Neimark, S. Rigby, R. Skudas, K. Sing, M. Thommes, K. Unger, *Micropor Mesopor Mat* **2012**, 154, 2.

[97] C. Schlumberger, M. Thommes, *Adv Mater Interfaces* **2021**, 8.

[98] J. Rouquerol, G. Baron, R. Denoyel, H. Giesche, J. Groen, P. Klobes, P. Levitz, A. V. Neimark, S. Rigby, R. Skudas, K. Sing, M. Thommes, K. Unger, *Pure Appl Chem* **2012**, 84, 107.

[99] T. Young, *Philosophical Transactions of the Royal Society of London* **1805**, 95, 65.

[100] D. Bonn, J. Eggers, J. Indekeu, J. Meunier, E. Rolley, *Reviews of Modern Physics* **2009**, 81, 739.

[101] P. G. de Gennes, *Reviews of Modern Physics* **1985**, 57, 827.

[102] L. Leger, J. F. Joanny, *Rep Prog Phys* **1992**, 55, 431.

[103] R. Lucas, *Kolloid Z.* **1918**, 23, 15.

[104] E. W. Washburn, *Phys. Rev.* **1921**, 17, 273.

[105] F. H. Kriel, R. Sedev, C. Priest, *Isr J Chem* **2014**, 54, 1519.

[106] J. C. Cai, Y. Chen, Y. Liu, S. Li, C. H. Sun, *Adv Colloid Interfac* **2022**, 304.

[107] M. N. Popescu, G. Oshanin, S. Dietrich, A. M. Cazabat, *Journal of Physics-Condensed Matter* **2012**, 24.

[108] D. Quere, *Europhys Lett* **1997**, 39, 533.

[109] K. Binder, J. Horbach, R. Vink, A. De Virgiliis, *Soft Matter* **2008**, 4, 1555.

[110] S. Chibbaro, L. Biferale, F. Diotallevi, S. Succi, K. Binder, D. Dimitrov, A. Milchev, S. Girardo, D. Pisignano, *Epl-Europhys Lett* **2008**, 84.

[111] M. G. Bernadiner, *Transport in Porous Media* **1998**, 30, 251.

[112] G. N. Constantinides, A. C. Payatakes, *Transport in Porous Media* **2000**, 38, 291.

[113] T. Koga, N. Jiang, P. Gin, M. K. Endoh, S. Narayanan, L. B. Lurio, S. K. Sinha, *Phys Rev Lett* **2011**, 107.

[114] D. Benavente, P. Lock, M. A. G. Del Cura, S. Ordonez, *Transport in Porous Media* **2002**, 49, 59.

[115] L. L. Handy, *T Am I Min Met Eng* **1960**, 219, 75.

[116] K. W. Li, R. N. Horne, *Spe J* **2004**, 9, 322.

[117] A. Lundblad, B. Bergman, *J Electrochem Soc* **1997**, 144, 984.

[118] M. Strobl, I. Manke, N. Kardjilov, A. Hilger, M. Dawson, J. Banhart, *J Phys D Appl Phys* **2009**, 42.

[119] A. Snigirev, I. Snigireva, V. Kohn, S. Kuznetsov, I. Schelokov, *Review of Scientific Instruments* **1995**, 66, 5486.

[120] S. C. Mayo, A. W. Stevenson, S. W. Wilkins, *Materials* **2012**, 5, 937.

[121] M. E. Coles, R. D. Hazlett, P. Spanne, W. E. Soll, E. L. Muegge, K. W. Jones, *J Petrol Sci Eng* **1998**, 19, 55.

[122] C. J. Werth, C. Y. Zhang, M. L. Brusseau, M. Oostrom, T. Baumann, *J Contam Hydrol* **2010**, 113, 1.

[123] J. I. Goldstein, D. C. Joy, J. R. Michael, D. E. Newbury, N. W. M. Ritchie, J. H. J. Scott, DOI: 10.1007/978-1-4939-6676-9, Springer New York, New York, NY 2018, 550 pages.

[124] C. A. Schneider, W. S. Rasband, K. W. Eliceiri, *Nature Methods* **2012**, 9, 671.

[125] D. Necas, P. Klapetek, *Central European Journal of Physics* **2012**, 10, 181.

[126] P. E. Danielsson, M. Hammerin, *Cvgip-Graphical Models and Image Processing* **1992**, 54, 340.

[127] C. C. Aggarwal, *Data Classification - Algorithms and Applications*, Chapman and Hall/CRC, New York **2014**.

[128] W. S. Rasband, U. S. National Institutes of Health, Bethesda, Maryland, USA 1997-2018.

[129] A. El Aferni, M. Guettari, T. Tajouri, *Environ. Sci. Pollut. Res.* doi: 10.1007/s11356-020-11188-y.

[130] OriginLab Corporation, accessed July 1, 2021.

[131] H. Kim, A. Ruhm, L. B. Lurio, J. K. Basu, J. Lal, D. Lumma, S. G. J. Mochrie, S. K. Sinha, *Phys. Rev. Lett.* **2003**, 90, 068302.

[132] G. C. Berry, T. G. Fox, *Advances in Polymer Science* **1968**, 5, 261.

[133] M. L. Williams, R. F. Landel, J. D. Ferry, *Journal of the American Chemical Society* **1955**, 77, 3701.

[134] J. Brandrup, E. H. Immergut, E. A. Grulke, *Polymer Handbook*, Wiley, New York **1999**.

[135] J. L. Rodgers, W. A. Nicewander, *American Statistician* **1988**, 42, 59.

[136] S. Napolitano, M. Wübbenhorst, *Nat. Commun.* **2011**, 2.

[137] D. Enke, F. Friedel, T. Hahn, F. Janowski, in *Characterization of porous solids VII*, Vol. 160 (Eds: P. Llewellyn, F. R. Reinoso, J. Rouqerol, N. Seaton), Elsevier, Amsterdam **2007**, p. 455.

[138] H. Preising, D. Enke, *Coll. Surf. A Physicochem. Eng. Aspects* **2007**, 300, 21.

[139] A. B. Shelekhin, A. G. Dixon, Y. H. Ma, *Journal of Membrane Science* **1993**, 83, 181.

Abbreviations

3D	three-dimensional
2D	two-dimensional
AAO	Anodized aluminum oxide
CPG	Controlled porous glass
DSC	Differential scanning calorimetry
EDX	Energy-dispersive X-ray spectroscopy
FEG-TEM	Field-emission gun transmission electron microscopy
FIB	Focused-ion beam
HA	Hard anodization
IUPAC	International Union of Pure and Applied Chemistry
LW	Lucas-Washburn
MA	Mild anodization
NMR	Nuclear magnetic resonance
PDI	Polydispersity index
PDMS	Polydimethylsiloxane
PEO	Polyethylene oxide
PS	Polystyrene
SAXS	Small-angle X-ray scattering
SDD	Silicon drift detector
SEM	Scanning electron microscopy
SESI	Secondary electrons secondary ions
TIFF	Tag image file format
VPG	Vycor® porous glass
WD	Width descriptor
WLF	Williams-Landel-Ferry
X-ray CT	Zernike phase-contrast X-ray computed tomography

List of publications

Parts of this dissertation were reported in:

Vazquez Luna, F.; Maurya, A. K., M.; Martins de Souza e Silva, J.; Dittrich, G.; Paul, T.; Enke, D.; Huber, P.; Wehrspohn, R.; Steinhart, M., Straight versus Spongy – Effect of Tortuosity on Polymer Imbibition into Nanoporous Matrices assessed by Segmentation-Free Analysis of 3D Sample Reconstructions - *Accepted*

Vazquez Luna, F.; Gerstenberger, M.; Dittrich, G.; Martins de Souza e Silva, J.; Huber, P.; Wehrspohn, R.; Steinhart, M., Statistical Analysis of Submicron X-ray Tomography Data on Polymer Imbibition into Arrays of Cylindrical Nanopores. *The Journal of Physical Chemistry C* **2021,** *125* (48), 26731-26743.

Additional publications:

Eichler-Volf, A.; Alsaadawi, Y.; Vazquez Luna, F.; Khan, Q. A.; Stierle, S.; Xu, C.; Heigl, M.; Fekri, Z.; Zhou, S. Q.; Zahn, P.; et al. Sensitivity of PS/CoPd Janus particles to an external magnetic field. *Rsc Adv* **2021**, *11* (28), 17051-17057

Eichler-Volf, A.; Huang, T.; Vazquez Luna, F.; Alsaadawi, Y.; Stierle, S.; Cuniberti, G.; Steinhart, M.; Baraban, L.; Erbe, A. Comparative Studies of Light-Responsive Swimmers: Janus Nanorods versus Spherical Particles. *Langmuir* **2020**, *36* (42), 12504-12512.

Curriculum Vitae

01/2018 – 03/2022	**University of Osnabrück** Research Assistant, PhD student Research topic: Statistical Evaluation of the Imbibition of Polymers into Porous Materials.
09/2014 – 09/2016	**M. Sc. in Materials Science Exploiting Large Scale Facilities** Ludwig Maximilians Universität München and University of Turin Master thesis: Thermoresponsive Nanocomposite Hydrogels for Sensing Applications.
08/2009 – 06/2014	**B. Sc. In Nanotechnology and Molecular Engineering** University of the Americas Puebla Bachelor thesis: Modification of Asphalt with Nanofibers and Carbon Nanotubes and Evaluation of the Mechanical Properties.